DISSERTATION

SINGLE CANCER CELL DETECTION WITH OPTOFLUIDIC INTRACAVITY SPECTROSCOPY

Submitted by

Weina Wang

Department of Electrical and Computer Engineering

In partial fulfillment of the requirements

For the Degree of Doctor of Philosophy

Colorado State University

Fort Collins, Colorado

Summer 2012

Doctoral Committee:

Advisor: Kevin Lear

V. Chandrasekar
Diego Krapf
Kenneth Reardon

ABSTRACT

SINGLE CANCER CELL DETECTION WITH OPTOFLUIDIC INTRACAVITY SPECTROSCOPY

The detection of cancer cells is the basis for cancer diagnostics, cancer screening and cancer treatment monitoring. Non-destructive and non-chemical optical methods may help reduce the complexity and cost of related test, making them more available to the public.

The label-free technique of optofluidic intracavity spectroscopy (OFIS) uses light transmitted through a cellular body in a microfluidic optical resonator to distinguish different types of cells by their spectral signatures. The OFIS chips are fabricated in the CSU semiconductor clean room and the fabrication process was reported by a previous Ph.D student, Hua Shao. She also did some initial exploration on combining dielectrophoresis (DEP) with the OFIS technique. Since then, some revisions to the fabrication technique have been made to improve the alignment, bonding and sealing of this microfluidic chip. In addition, new DEP electrode designs have been designed and fabricated to further improve the trapping performance of the traps and facilitate automated cell trapping and analysis.

Viability tests were carried out to investigate the effect of heating (induced by DEP electrodes) on cells in chips built with borosilicate and sapphire substrates. These experiments used specially designed DEP electrodes that help more accurately control

the DEP exposure time and strength. The survival rate of cells out of DEP enabled OFIS system is greatly affected by the substrate type and DEP exposure dose.

The OFIS technique has differentiated red and white human blood cells, as well as canine lymphoma and lymphocytes based on their distinctive transmission spectra. Using OFIS chips fabricated with the modified process, OFIS spectra of settled cells from canine hemangiosarcoma (HSA) cell lines and monocytes in peripheral blood mononuclear cells (PBMCs) were collected and analyzed. To quantify the strength of transverse modes in their spectra, a single characteristic parameter was determined for each cell by forming a linear combination of the mean and standard deviation of the transmission spectra over one free spectral range excluding the residual longitudinal peaks of the bare Fabry-Pérot (F-P) cavities filled with cell suspending medium only. The difference in the characteristic parameters of HSA and monocyte samples was highly statistically significant with a *p*-value as low as 10^{-6}. A receiver operating characteristic (ROC) curve constructed from *t*-distributions fit to the HSA and monocytes spectra indicates that the cell classification based on their characteristic parameters can achieve 95% sensitivity and 98% specificity simultaneously.

Furthermore, some features observed in the spectra of HSA cells motivated a new optical model of the cell loaded F-P cavity. The OFIS spectra of individual cells from canine HSA and canine lymphoma cancer cell lines exhibit relatively uniformly spaced multiple transverse modes repeated in each free spectral range of a microfluidic F-P cavity while similar spectra of healthy canine monocytes and lymphocytes only have up

to 2 or no transverse mode peaks. Modeling of the cells as thin lenses allows paraxial Gaussian beam resonator analysis that produces spectral features that quantitatively match the frequencies of transverse modes and qualitatively agree with the trends in maximum transmission of the modes when aperture losses are included. The extracted experimental focal lengths are significantly larger for cancerous cells than for noncancerous cells and can be used as a potential cell malignancy indicator.

Furthermore, a thick lens model was developed, allowing manipulation of more parameters related to cell morphology and its location in the cavity. This model was used to interpret experimental results acquired from settled and suspended cells.

TABLE OF CONTENTS

CHAPTER 1 INTRODUCTION

This dissertation describes the improvements to optofluidic intracavity spectroscopy for single cancer cell detection. This chapter introduces the motivation for these improvements including the new cell differentiation algorithm and a new optical model. The organization of this dissertation will be presented in this chapter, too.

1.1 Motivation

Currently the most common and more accurate diagnostic method the pathologists use for the determination and examination of tumor cells is biopsy, which is usually invasive and involves complications such as pain and infection. And the test result takes a few days to get and needs expertise to interpret, and could still be inconclusive or give false readings that leads to false positive clinical diagnostics. Other auxiliary cancer diagnostic methods include physical examination, imaging such as x-ray and MRI (magnetic resonance imaging), endoscopy, and lab tests such as blood and urine tests. These techniques usually reveal signs of abnormal but will require other tools to confirm that the abnormality is tumor. Some of them also need expertise to help interpret the test result, or involve sophisticated equipments that are very costly and not easily available for the general public to use as a cancer screening test. [1]

Label-free optical diagnostics offer a variety of advantages and can provide valuable information about the biological state of cells and in particular may be used for cancer

detection [2]. Some of the advantages include minimal invasion due to the small size of sample needed, easy to operate and interpret, real-time detection, relatively cheap and portable for some of the devices built with lab-on-a-chip technology, making them suitable diagnostic and cancer screening applications even for rural areas.

The optofluidic intracavity spectroscopy (OFIS) technique utilizes optical refraction, diffraction and interference effects in a microfluidic resonator, e.g., a plane-plane Fabry-Pérot (F-P) cavity, to produce characteristic transmission spectra of individual cells. Previously, differentiation of cancerous canine lymphoma and baseline lymphocytes with OFIS was successfully demonstrated, and analyzed in terms of longitudinal mode shift and lateral confinement induced by the cells [3].

While that study found mode shifts of canine lymphoma were extremely repeatable, further experiments revealed they were not sufficiently repeatable to distinguish a more aggressive canine cancer cell line, hemangiosarcoma (HSA), from a background of peripheral blood mononuclear cells (PBMCs). So an alternative analysis of OFIS spectra based on a single parameter quantification of the strength of transverse modes was developed and proven applicable to both HSA and canine lymphoma differentiation from the baseline PBMCs. Then some interesting features in the transverse mode of HSA spectra were noticed, including the frequency spacing between adjacent transverse modes were moderately uniform and the intensity decreased as the optical frequency increases. This observation motivated a new optical model that treats a cell sitting on the channel bottom as a thin lens. Applying apertured Gaussian beam analysis provides

further insight into the relationship between OFIS spectra and cellular shape, size, and refractive index. The thin-lens cell model enabled the further analysis of OFIS spectra and revealed that compared with a cell's refractive index or size, its deformability which is related to the malignancy and is reflected on cell's focal length and aspect ratio, could be a more reliable cell differentiation method [4].

The chip bonding and sealing is an essential part of the microfuidic device fabrication. And combining the OFIS technique with dielectrophoresis (DEP) cell immobilization method with sufficient trapping strength also motivated an improved OFIS chip fabrication technique.

1.2 Overview of the dissertation

In order to give the reader a basic understanding of the OFIS single cancer cell detection technique, background information including a literature review on optical single cell detection techniques, cell manipulation methods and cell biology that is related to OFIS detection, will be presented in Chapter 2.

This is followed by an introduction of the single cell manipulation method of DEP trapping, as well as the DEP electrode designs in this project in Chapter 3. How the electrode patterning and device sealing demanded an improved OFIS chip fabrication process will be discussed Chapter 4. The optical experimental setup, including the fluidic flow, software and hardware control system will be presented in Chapter 5. The results on spectrum-comparison based experiments, as well as the quantitative and

qualitative analysis are discussed in detail in Chapter 6. Chapter 7 discusses the spectral features of cancerous cells and how a cell lens model treats the cell as thin lens and uses apertured Gaussian beam analysis to understand and explain the experimental data. A thick lens cell model which allows more parameter describing the cell morphology and its position in the cavity is presented in this chapter as well. Chapter 8 reports the experimental results on cell deformation, an attempt to differentiate cancerous cells by comparing their focal length change between when they settle at channel bottom and when they are suspended or lifted by DEP force. The later part was done with OFIS chips constructed with sapphire substrates, and the thick lens model was applied to analyze these data. Lastly, the investigation into how changing chip substrates from borosilicate glass to sapphire and increasing DEP exposure dose on the survival rate of cells is presented in Chapter 9.

References:

[1] http://www.medicinenet.com/cancer_detection/article.htm.

[2] V. Backman, M. B. Wallace, L. T. Perelman et al., “Detection of preinvasive cancer cells,” *Nature*, vol. 406, no. 6791, pp. 35-36, Jul, 2000.

[3] H. Shao, W. Wang, S. E. Lana, and K.L. Lear, “Optofluidic intracavity spectroscopy of canine lymphoma and lymphocytes,” *IEEE Photonics Technology Letters*, vol. 20, no. 5-8, pp. 493-495, Mar-Apr, 2008.

[4] W. Wang and K.L. Lear, "A potential individual cell malignancy indicator: focal length", Advanced Biomedical and Clinical Diagnostic Systems IX, a part of the *SPIE BiOS: Biomedical Optics Symposium in Photonics West 2011 (SPIE*), paper 7890-1, San Francisco, Jan. 24, 2011.

CHAPTER 2 BACKGROUND

This chapter will present a literature review on a few aspects that the OFIS technique involves. These include various methods of optical interrogation of single cells, techniques for cell position manipulation and a brief review of cell biology. The techniques usually used for canine hemangiosarcoma (HSA) detection were also reviewed in this chapter.

2.1 Literature review of optical detection of single cells

The most common diagnostic method pathologists use for the determination and examination of tumor cells is staining, which requires expertise and could give false readings that lead to false positive clinical diagnostics. There have been various attempts to realize accurate, label-free, real-time, high-throughput screening for tumor cells with optical technologies and they may play an important role in advanced early detection, diagnosis and treatment of cancer. To improve the accuracy of the diagnostic means the device needs to have high sensitivity and specificity. When the diagnostic process is label-free, it usually doesn't require any reagent or any fluorescent tagging on the biological component that is being analyzed, saving cost and process time. And real-time diagnosis is always preferred to provide instant information to the patient. In order to realize this, the device needs to be able to handle a large amount of sample (large enough to give a statistically reliable result) in a relative short period of time, such as two hours instead of a few days.

Optical processes such as absorption, scattering, diffraction and refraction can probe the inherent refractive index properties of cells, which are related to a cell's size, shape and intracellular components. These optical technologies investigate the optical density (refractive index) and/or the size of cells which provide valuable information about the biological state of cells and in particular may be used for cancer detection [1].

2.1.1 Flow cytometry

Flow cytometry is a powerful technique for analyzing chemicals, particles, and cells in clinical diagnostics, biochemistry, and biology. In flow cytometry, cells or particles flow in suspension, preferably in a single file, pass by an optical detection apparatus one by one, as shown in Fig. 2.1 (a). And parameters such as scattered light and fluorescence are measured to provide information about the cells or particles of interest. It allows simultaneous multiparametric analysis of the physical and/or chemical characteristics of up to thousands of particles or cells per second. Flow cytometry is routinely used in the diagnosis of health disorders, especially blood cancers, but has many other applications in both research and clinical practice.

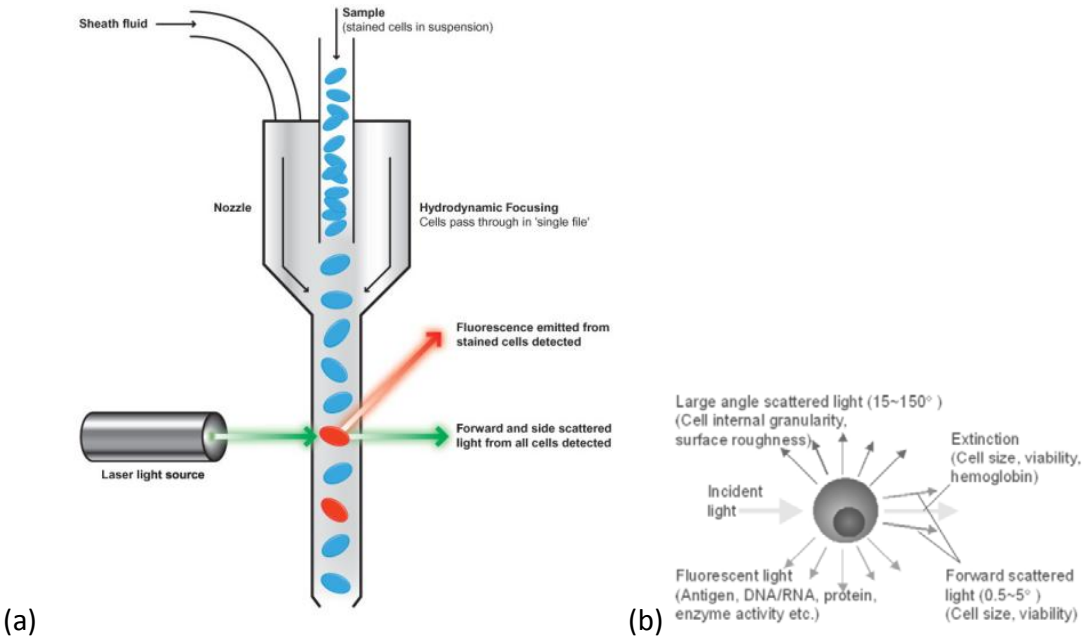

Fig. 2.1 Schematic of the (a) working and (b) measuring principle of flow cytometer (Reproduced from [2,3]).

Cells can be selected for sorting based on all of the measured properties of fluorescence and light scatter. The correlation of light scattering and the spatial organization of mitochondria are as follows: in normal liver cells, for example, mitochondria are highly organized within the cytoplasm and highly scattering, yielding a highly correlated signal, but in cancer cells, mitochondria are more chaotically organized and poorly scattering [4]. As shown in Fig. 2.1 (b), forward scattering, measured in a very narrow scattering angle range (0.5–5.0° to the incident light), provides information on the size and viability of cells or particles. And large angle scattering, detected in a broad scattering angle range (15–150° to the incident light), gives information on surface roughness and

internal structures of cells or particles, such as cell internal granularity. When a cell or particle passes through the light beam, the amount of direct light decreases due to a combination of absorbance and light scattering, and this decrease provides information on size, viability, and protein contents.

Although the scattering provides information on cell size and granularity, more conventionally fluorescent labels are involved in flow cytometry. Typically up to 6 fluorescent labels are used; the fluorescent light is filtered and then collected by different color detectors. Even though the fluorescent tagging is cost efficient per run, a flow cytometer is expensive to buy (a few hundred thousand dollars for analyzers) and to operate (typically a few hundred thousand dollars per year, for a full-time clinical flow cytometry lab). That makes flow cytometry a relatively expensive approach but still not a very accurate measure of refractive index.

2.1.2 Biocavity laser based biosensor

A recent example of optical interferometry of cells involves placing individual cells in laser or resonant cavities and observing how the cells modify the cavity modes. In the majority of previously reported Fabry-Pérot (F-P) cavity based sensing devices, only changes in longitudinal modes were considered. Although the techniques could successfully determine the refractive index and thus infer some information about the biological state of living cells in real time without any cell labeling or chemical treatment, they had some limitations.

Gourley [5] used the biocavity laser spectroscopy to measure the biophysical optic parameter Δλ, the wavelength shift of the laser, as well as the transverse modes which are related to the optical density of a cell or mitochondria [6] that uniquely reflects its size and biomolecular composition. The device has an etched microfluidic channel integrated with half of a GaAs VCSEL structure as shown in Fig. 2.2.

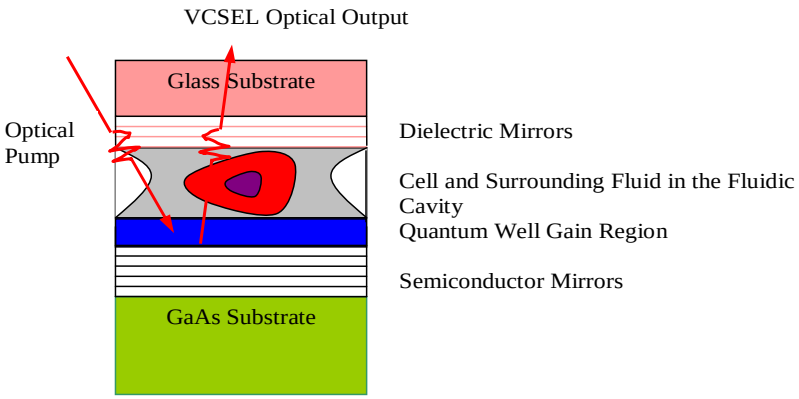

Fig. 2.2 Schematic diagram of the optically pumped VCSEL based biosensor developed by Gourley et al (Reproduced from [7]).

With this device they demonstrated that different cell types resulted in multimode laser spectra with mode offset, spacing, and intensity being characteristic of the cell type. The spacing and intensity distributions of the spectral peaks of the VCSEL output yielded a unique spectral signature for the four types of cells they worked with: platelets, white blood cells, red blood cells and spindle nuclei cancer cells [7].

The need for an external solid-state or other laser to optically pump the VCSEL increases the size and cost of such a device. However, this idea motivated the OFIS project to extract the characteristic spectral signature of different types of cells. Spectroscopy on spheres and cells were reported using the biocavity technique. However, the biocavity laser system required an external laser, which increased the cost of the system and was an impediment to miniaturization. Gourley and co-workers relied on both fundamental mode shifts and observations of the number of transverse modes to characterize cells.

In our group, an alternative approach was carried out [8] to electrically pump the VCSEL but high gain material would be required to overcome the losses associated with the introduction of the cells and the cell suspending media, which greatly complicated the fabrication process.

2.1.3 Microfluidic fiber optic biosensor

Fiber optic biosensor usually refers to optical fiber derived devices that utilize optical field to measure biological species such as the presence of cells, as well as the attachment of proteins and DNA. The transduction mechanisms used in fiber optic biosensors are changes in output power due to refractive index changes (i.e., intensity-based), evanescent field absorption [9-10], fluorescence [11-14] and Surface Plasmon Resonance (SPR) [15-16]. Because they have the ability to do real-time, low cost and accurate detection, fiber optic biosensors have become promising alternatives to traditional immunological methods for biomedical applications.

This section will review one particular kind of fiber optic biosensor that, instead of measuring cell concentration, combines optical fiber with microfluidics and is capable of single-cell detection, which is a research area closer to the OFIS project compared with other types of fiber optic biosensors. This microfluidic fiber optic biosensor [17] was designed by a group in Singapore, and it used two single-mode fibers with high reflectivity coating on the end facets to form a Fabry-Pérot (F-P) cavity, as shown in Fig. 2.3 below.

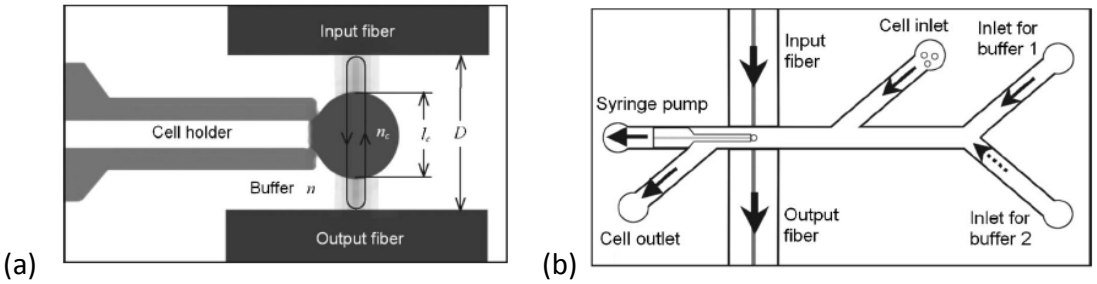

Figure 2.3 (a) Working principle of an on-chip microfluidic F-P cavity for single cell detection, (b) Structure of the chip. (Reproduced from [17])

The cell was immobilized by a cell holder (a micropipette), and the refractive index of each cell could be measured by observing the shift of the resonant wavelength of the optical cavity when two kinds of buffer solution with different index was used.

This device can measure the size (determined by the spectral shift) and refractive index (calculated with known index of the two buffers) of a cell. The size (with a standard

deviation of 4.0%) and index (with a standard deviation of 0.2%) of 4 MDCK cells was reported in [17]. It applied similar sensing mechanism, intracavity spectroscopy, as used in OFIS, which is based on the refractive index perturbation of an optical resonator. However, unlike OFIS, the multiple transverse mode operation induced by the cell was neglected in their analysis.

Similarly, a microfluidic resonator designed by Domachuk [18] integrated a F-P cavity formed between optical fiber Bragg grating reflectors across a planar microfluidic channel. The position of the phase reflection plane of distributed Bragg reflectors, which was several periods out from the fiber faces, making the effective cavity length substantially longer than the channel width, reducing the sensitivity to cellular refractive index. Refractive index changes as low as 0.2% were resolved; however, this approach still required sophisticated equipment such as a high-resolution spectrometer to monitor small shifts in the resonant wavelength of the high finesse cavity.

So in these approaches, a high-resolution spectrometer was still an essential part of the apparatus. Transverse mode spectra were not investigated in either one of these fiber-based F-P interferometers, nor did they consider lateral confinement effects.

2.2 Literature review of cell manipulation

Cell steering and manipulation has always been an important issue in the analysis of single cells. For OFIS spectral acquisition, a cell needs to stay at the exact same location

for 3-6 seconds to allow for spectral acquisition, so that better signal-to-noise ratio (SNR) of the cell spectra could be achieved.

2.2.1 Optical trapping

Optical tweezers [19] is one of the most widely applied optical methods for cell manipulation in single molecule and cellular studies. It uses optical gradient forces to trap particles at the focal point of highly focused laser beams, as indicated in Fig. 2.4 (a). Optical tweezers have been an invaluable tool in cell biology research, for the trapping of atoms, virus, bacteria and cells [20-22]. Optical tweezers offer high resolution for single cell trapping in three dimensions, but have limited manipulation area due to tight focusing requirement.

To overcome this limitation, Ashkin [19], as well as Smith *et. al.* [23] produced a point in space where the scattering force produced by two laser beams cancel with each other, as shown in Fig. 2.4 (b). This design, especially its fiber optic implementation [24], has been integrated with microfluidics for the trapping of biological cells, as long as the refractive index of the particle or cell is larger than that of the surrounding medium, and the beam sizes are larger than the size of the trapped object.

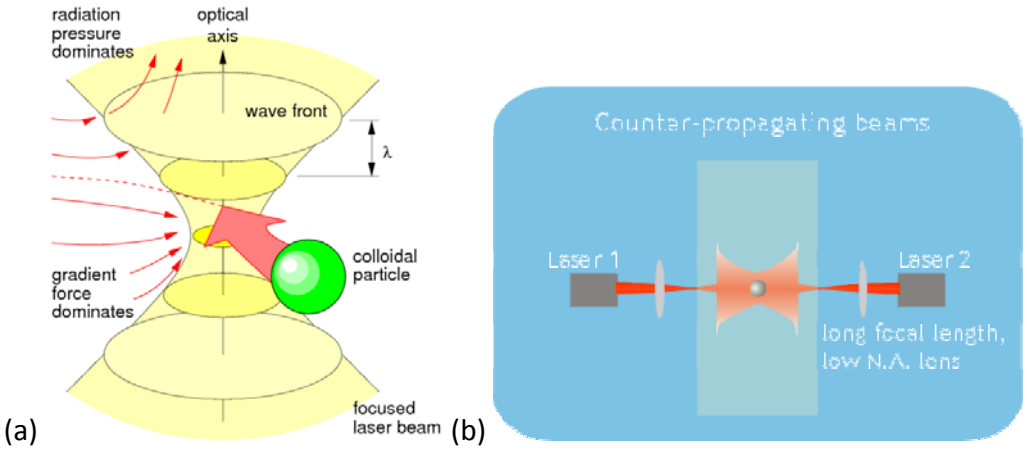

Fig. 2.4 (a) Optical tweezers that trap particle at the focal point of a highly focused laser beam [25]; (b) optical tweezers with counter-propagating beams [26].

Another application that uses the optical force of the optical tweezers (approximately pico- to nano- Newton) is the optical stretcher [27, 28]. The basic concept is that with dual beam trapping, if the object trapped is sufficiently elastic, the surface forces could stretch it along the beam axis, because of the opposite surface forces on the front and backside of the object. More details of this method will be reviewed in the cell deformation section.

2.2.2 Dielectrophoresis (DEP) trapping

Dielectrophoresis (DEP) trapping utilizes the phenomenon that DEP force is applied upon a particle (with a different dielectric constant from the suspending media) when it is subjected to a non-uniform electric field [29, 30]. The DEP force is given by [31]:

$$F_{DEP} = 2\pi r^3 \varepsilon_m Re[K(\omega)]\nabla E^2 \quad (2.1)$$

where r is the radius of the particle, ε_m is the permittivity (dielectric constant) of the medium, $K(\omega)$ is the polarization factor, also know as the Clausius-Mossotti (CM) function that contains all the frequency dependence of the DEP force,

$$K = \frac{\varepsilon_p^* - \varepsilon_m^*}{\varepsilon_p^* + 2\varepsilon_m^*} \quad (2.2)$$

and the complex permittivity ε^* is,

$$\varepsilon^* = \varepsilon - j\frac{\sigma}{\omega} \quad (2.3)$$

where ε is the dielectric constant, σ is the electrical conductivity and ω is the field frequency for either the particle or the media. Apparently the intensity of the DEP force is determined by the medium and particles' electrical properties, the particles' shape and size, as well as the frequency of the electric field. This motivated a lot of work to not only manipulate particles such as cells [32-37], but sort them with great selectivity [32, 38-42].

Also, there are two types of DEP traps. Depending on the dielectric constant of the particle and the suspending media, the DEP force would either push the particle to the location where the E^2 is bigger ($\varepsilon_p^* > \varepsilon_m^*$, positive DEP or pDEP), as shown in Fig. 2.5; or push it to the location where E^2 is smaller ($\varepsilon_p^* < \varepsilon_m^*$, negative DEP or nDEP). Due to the opaque nature of the gold electrodes we put down as the DEP electrodes, nDEP is

required for OFIS application where the transmission spectrum of cell loaded optical cavity is collected. And since the dielectric constants of the media and the particles are both frequency dependent, one can choose to use pDEP or nDEP by simply changing the working electrical frequency of the DEP traps; moreover, the electrical conductivity of the media can be changed by varying the concentration of the salty solution, and the dielectric properties of biological cells are related to their viability.

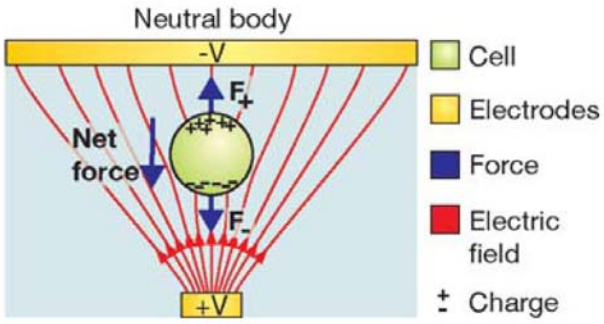

Fig. 2.5 A neutral particle gets polarized in a non-uniform electric field. The particle will experience a net force toward the electric-field maximum because the field magnitude is different at the top and bottom part of the particle ($F_- > F_+$), such as in a pDEP case. (Reproduced from [43].)

A typical example of the application of DEP trapping and sorting was reported in [44], where planar DEP structure as shown in Fig. 2.6 was used. First the yeast cells were trapped with 5Vpp, 10kHz signal; and as the frequency went up to 10MHz, the non-viable cells (stained with methylene blue) formed triangular aggregations between the

electrodes (nDEP) while the viable cells gathered on the edges of electrodes (pDEP). And then the non-viable yeast cells were flushed by passing a gentle stream of fluid medium through the chamber.

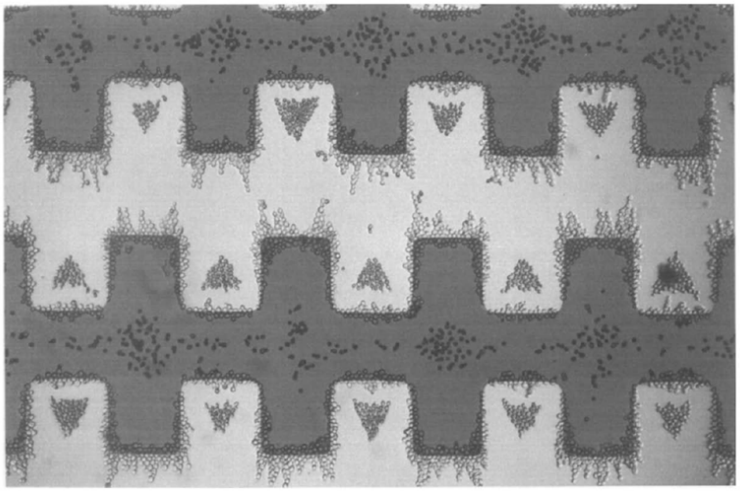

Fig. 2.6 Local separation of viable and non-viable (stained) yeast cells with dielectrophoresis. (Reproduced from [44].)

Similarly, others employed different DEP structure to realize the separation between electroporated and non-electroporated cells [45, 46]. The relationship between electroporation and cell viability will be further reviewed in Section 2.3.2.

2.3 Brief review of cell biology

This section consists of a brief review of cell biology that is related to OFIS detection and DEP trapping. A few aspects of cell biology that we care about for this research are: the

cell permittivity vs. cell types, i.e., at what electrical frequency the cells could be trapped steadily by nDEP; the viability of the cells, whether it is affected by the electric field applied or the local temperature raise due to Joule heating, and whether the OFIS spectra vary with cell viability; last but not least, how the cell cycle influences the OFIS spectra.

2.3.1 Cell permittivity

As discussed in the previous section, the dielectric constants (i.e., permittivity) of both the suspending media and the cells are frequency dependent. The permittivity of the media can be changed by varying the electrical conductivity of the solution, i.e., by changing concentration of the salty content or by adding low-conductivity buffer. Fig. 2.7 shows an example of frequency dependence measurement of *Re[K(ω)]* reported in [43].

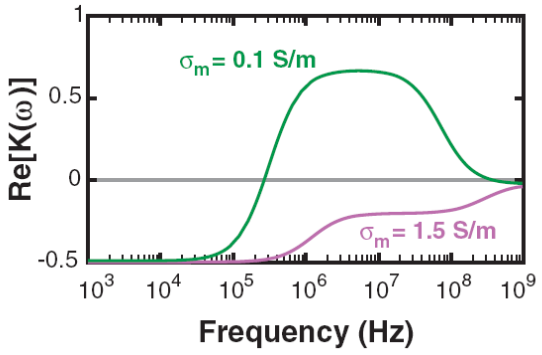

Fig. 2.7 Real part of the CM factor of mammalian cells at low (0.1 S/m) and high (1.5 S/m) solution conductivities. (Reproduced from [43].)

As for the permittivity of biological cells, it is basically a parameter that describes how easy or hard it is to polarize a cell. Thus it is believed that the cell permittivity is related to several factors, such as cell type, cell viability, as well as the cell cycle. Due to the lack of literature on the frequency dependence of cell permittivity of any types of cells until lately, only simulated results can be found in [47]. And it is a intuitive understanding that cell cycle and especially its viability affects the protein content inside a cell, and results in different cell permittivity.

2.3.2 Cell viability

Cell viability is a determination of living or dead cells, based on a total cell sample. However, the determination of cell viability is not as straightforward as it sounds and the result often varies with the technique employed. Testing for cell viability usually involves looking at a sample cell population and staining the cells or applying chemicals to show which are living and which are dead, and there are several popular tests and methods for measuring cell viability. The majority of this section was learned from [48].

The viability of a cell usually refers to the status of a cell to survive and function normally, including growing and multiplying. So naturally the traditional method of culturing the cells and comparing the number of cells with a control group is the most reliable viability test. However, this usually takes at least 24 hours and there are

multiple factors that affect the success rate, such as patient factors or cycle factors, which would influence the test result.

Some other tests are generally faster. A Method of Transcriptional and Translational (MTT) assay could be carried out to determine the metabolic activity of the cell based on their ability to reduce yellow tetrazolium salt. Another option is the Annexin V apoptotic test which identifies cells in the early stages of apoptosis before the membrane has degraded. Probably the most informative test however, would be to simply plate out the cells after they have been run through the chip and determine which were able to attach and form colonies [48].

The fastest and most commonly used method for cell viability test, is the Trypan blue exclusion test. The mechanism is that as a cell loses viability, the cell membrane degrades and becomes more and more porous, and the increased porosity allows the large dye molecules to enter into the cell, whereas it would normally be excluded. So viable cells exclude the dye and thus appear clear, whereas nonviable ones do not exclude the dye and thus are stained blue. Another characteristic is that the nonviable cells will often appear bloated. So within each cell solution sample, the number of viable and nonviable cells could be counted and the viability can be calculated as *viability = # of viable cells / (# of viable cells + # of nonviable cells)*.

Now these methods all work with the original biological definition of viable cells; in the DEP trap enabled OFIS system, there are other phenomenon related with cell death, including denaturation and electroporation.

In biochemistry, denaturation is a process in which proteins or nucleic acids undergo structural change caused by extreme conditions such as a large rise of the ambient temperature. And in this process the proteins lose solubility, an example would be an egg's proteins when it is cooked. And the hydrophobic proteins even make communal aggregation, which means that they come closer and bond, so as to reduce the total area exposed to water [49]. And more specifically, the thermal denaturation causes loss of the multiple weak interactions holding the strands together along the entire length of the DNA molecules [50], and this could explain the cell shrinking observed in our experiments, with borosilicate chips and when DEP traps were turned on. The osteosarcoma (OSA) cell shrinking as the DEP voltage was increased (and the frequency was kept of 50MHz) is shown Fig. 2.7 below.

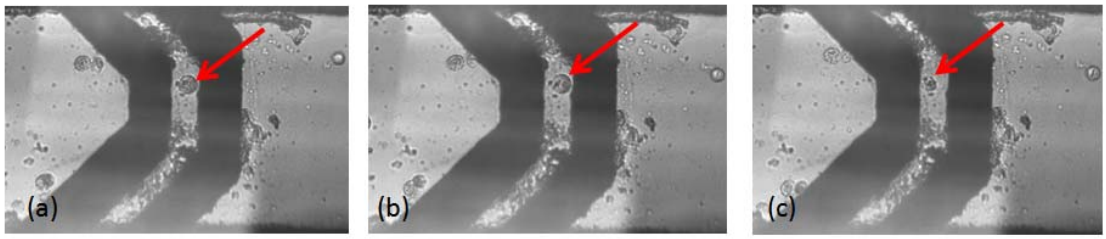

Fig. 2.7 Illustration of cell size change when the DEP voltage was increased from (a) 10V to (b) 12V and then (c) 14V.

Electroporation, also called electropermeabilization, uses an externally applied electrical field to cause a number of very small pores to open on the cell membrane and as a result, increases the permeability of the cell plasma membrane, making it easier in molecular biology to introduce a new substance to the cell [51, 52]. Electroporation is widely used to introduce foreign protein or genes into mammalian cells [46], in the study of new drugs and in clinical studies to treat malignant tumors [53]. With careful control of the strength of the electrical field and the duration of the cell's exposure to it, the pores will re-seal themselves after a short period of time. Dev, et al. [53] reported the relationship between the field strength and the duration of electrical fields that safely cause electroporation without cell lysis (the breaking down of cells), as shown in Fig. 2.8. From this figure, one can conclude that as long as the electric field is small enough or the cells' exposure to the field is short enough, the cell electroporation will not occur.

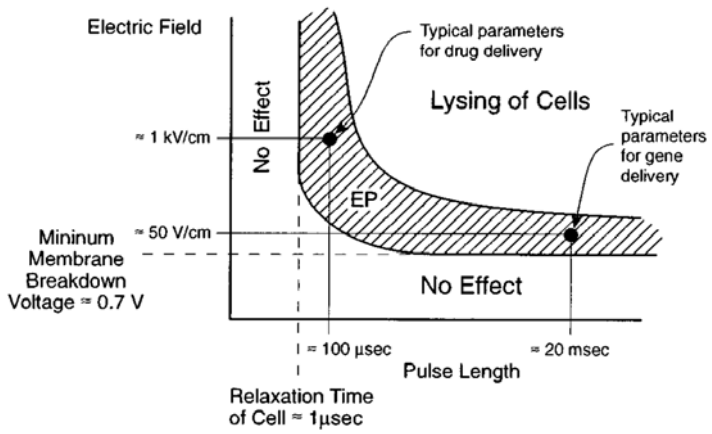

Fig. 2.8 Schematic relationship between field strength and pulse length applicable to the electroporation of cells. (Reproduced from [53].)

However, approaching the upper boundary of the electroporation region in Fig. 2.8, the electroporation may or may not be reversible. The cells that are exposed too long or to over-strong electrical fields can start the process of apoptosis (programmed cell death) or necrosis (premature death of cells), resulting in cell death [53, 54]. He [54] reported viability of cabbage cells dropped significantly as the applied voltage increased.

2.3.3 Cell cycle

The cell cycle consists of four distinct phases: G1 phase, S phase, G2 phase and M phase [55], as illustrated in Fig. 2.9. And the cells at each phase have different protein (n = 1.5) content and it may very likely affect their OFIS spectra. The majority of the information on cell cycle was gained from [56].

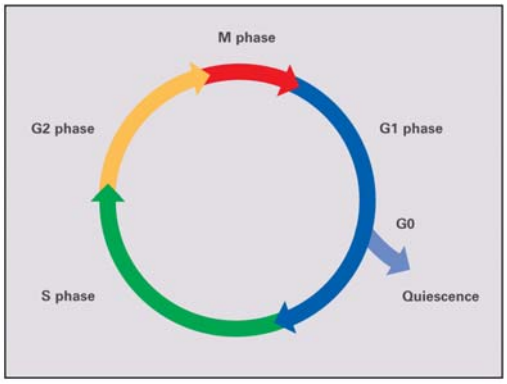

Fig. 2.9 Schematic of the cell cycle. (Reproduced from [57].)

Activation of each phase is dependent on the proper progression and completion of the previous one [58]. Cells that have temporarily or reversibly stopped dividing are said to have entered a state of quiescence called G_0 phase. G_1 phase (1^{st} Gap phase) is the longest and most variable cell-cycle phase: after mitosis (the process of a cell separating the chromosomes in its nucleus into two identical sets in two nuclei) and cytokinesis (the process that the cytoplasm of a single cell is divided to form two daughter cells) in the M phase, cells are half of their previous size and during G_1 grow back to their optimal size. Genes that are involved in cell-cycle progression are switched off so that the cell cannot initiate a new round of proliferation, thereby creating a restrictive point. If the appropriate positive stimuli are received, the cells overcome the restriction point block and trigger a program of gene expression that commits them to a new cycle of replication. Faulty restriction point control may result in a cell proliferation under inappropriate conditions, such as that seen in cancer cells.

The S phase is also known as the synthetic phase, where DNA replication occurs and initiates at many different sites. When the S phase is complete, all of the chromosomes have been replicated, so the amount of DNA in the cell has effectively doubled.

The G_2 phase (2^{nd} gap phase) is the in gap between DNA synthesis and mitosis, during which the cell continues to grow. Significant biosynthesis occurs during this phase, mainly involving the production of microtubules, which are required during the process of mitosis. During the G_2 phase, key enzymatic activities that will trigger entry into

mitosis gradually accumulate and are converted to the active forms, and when they reach a critical threshold level, the cell enters mitosis.

Cell growth stops at the M phase (Mitosis) and cellular energy is focused on the orderly division into two daughter cells. After cell division, each of the daughter cells begins the interphase of a new cycle.

If the cell sample could be synchronized at one phase of cell cycle, OFIS may have the ability to identify the cells at different phases based on their refractive index difference due to the diverse protein content.

2.4 Brief review of canine HSA detection techniques

Canine disease is usually considered as a model for the drug discovery and development research of human one. The dog is an excellent translational model for the investigation of novel antineoplastic therapies. Naturally develop canine cancers share many characteristics with human malignancies, such as tumor growth over long periods of time in the setting of an intact immune system, and metastasis to relevant distant sites [59]. And unlike murine (mouse) models, dogs are relatively outbred, immunocompetent animals with spontaneously occurring tumors, representing a spectrum of tumor histotypes that have biology similar to that found in humans. The relatively large size of canine tumors, when compared with murine tumors, may more closely approximate human solid tumors with respect to important biological factors

such as hypoxia and clonal variation, and allows for multiple samplings of tumor tissue over time [60,61]. Some discussion in this section was learned from [62].

One particular canine cancer of interest, hemangiosarcoma (HSA), is the most common splenic tumor of dogs, accounting for 51 to 66% of all splenic neoplasms [63,64]. It is a malignant neoplasm of vascular endothelial origin that is typified by rapid and aggressive metastasis and a very poor prognosis [62] for hardly any symptoms exhibit until an advanced stage when biopsy is available for clinical detection of canine HSA, but treatment is usually unsuccessful at this stage. The clinical diagnostics and current study on early detection of HSA are reviewed in this section.

2.4.1 Clinical diagnostics

Currently there are no efficacious screening tools to facilitate early detection of HSA. HSA is often suspected based on breed, age, clinical signs, history and physical examination [65] Other tests that may provide further support of this presumptive diagnosis include complete blood count (CBC), serum chemistry profile, coagulation profile, three-view thoracic radiographs, abdominal radiographs, abdominal ultrasound, echocardiogram and electrocardiography. These diagnostic tests can also be used to clinically stage the severity of disease into one of three clinical stages [48, 66]. However, there is no proven difference in median survival times (usually between a few months to less than a year) between different stages of disease.

While all of the above diagnostics will help support a diagnosis of HSA, the definitive diagnosis of HSA often requires biopsy or splenectomy and histopathology [48]. Unfortunately, many cases of HSA already have metastasized by the time they are clinically evident and at this stage even with surgical intervention, which costs thousands of dollars, there would be hardly any improvement in the overall survival time of the patients with HSA.

Due to the poor prognosis of HSA, novel techniques for its early detection would be of considerable clinical utility, so treatment may be instituted prior to development of overt clinical signs or grossly detectable disease. Eventually, these investigations may result in improved diagnosis and treatment of HSA, increased patient mean survival time and improved quality of life for patients with HSA [67].

2.4.2 Flowcytometry study on early detection of HSA

Other research [68] has shown promising results for the early detection of HSA, by recognizing some unique patterns of gene expression that can help distinguish hemangiosarcoma cells from normal blood vessel lining cells.

In their work, Modiano and co-workers have investigated the use of flow cytometry incorporating up to 6 fluorescent labels to interrogate 11 annotated genes and concluded that this technique may be useful in HSA diagnosis [68]. Recently, they've also provided further confirmation that these protein expression signatures not only reflect a cancer-associated angiogenic phenotype, but also distinguished

hemangiosarcoma from non-endothelial, moderately to highly angiogenic bone marrow-derived tumors such as lymphoma, leukemia and osteosarcoma [69].

However, the relatively high cost of flow cytometry equipment and supplies (as discussed in Section 2.1.1) and necessary operational expertise would limit access to this technique as reflected by the fact that only four veterinary hospitals in the U.S. are known to include flow cytometry labs. The Due to the high cost and the very limited availability of the equipment to the veterinary hospitals, it is unlikely that such a test can be generally applied to common dog patients. The need to rapidly and economically diagnose HSA with extremely poor prognosis from operable benign tumors in dogs with internal bleeding motivates research on low cost, widely available diagnostics for this disease.

References:

[1] V. Backman, M. B. Wallace, L. T. Perelman et al., “Detection of preinvasive cancer cells,” *Nature*, vol. 406, no. 6791, pp. 35-36, Jul, 2000.

[2] http://www.sonyinsider.com

[3] H. M. Shapiro, Practical Flow Cytometry, Willy-Liss, New York, 3rd ed., 1995.

[4] P. L. Gourley*, et al.*, "Mitochondrial correlation microscopy and nanolaser spectroscopy - New tools for biophotonic detection of cancer in single cells," *Technology in Cancer Research & Treatment,* vol. 4, pp. 585-592, Dec 2005.

[5] P. L. Gourley*, et al.*, "Vertical cavity surface-emitting laser scanning cytometer for high speed analysis of cells," in *Advances in Laser and Light Spectroscopy to Diagnose Cancer and Other Diseases Iii: Optical Biopsy, Proceedings*. vol. 2679, pp. 131-141, 1996,

[6] P. L. Gourley, et al., "Reactive biomolecular divergence in genetically altered yeast cells and isolated mitochondria as measured by biocavity laser spectroscopy: rapid diagnostic method for studying cellular responses to stress and disease," *Journal of Biomedical Optics*, vol. 12, Sep-Oct 2007.

[7] P. L. Gourley and A. E. McDonald, “Semiconductor microlasers with intracavity microfluidics for biomedical application”, *Proc. SPIE*, vol. 2978, pg. 186-196, 1997.

[8] D. Kumar, H. Shao, and K. L. Lear, “Microfluidic cavity surface emitting laser based biosensor*”, IEEE LEOS 17th Annual Meeting*, vol. 1, pp.118–119, November 7-11, 2004.

[9] S. W. Kang, et al., "SENSITIVITY ANALYSIS OF A THIN-FILM OPTICAL WAVE-GUIDE BIOCHEMICAL SENSOR USING EVANESCENT FIELD ABSORPTION," *Applied Optics*, vol. 32, pp. 3544-3549, Jul 1993.

[10] L. Cheng, et al., "Terahertz-wave absorption in liquids measured using the evanescent field of a silicon waveguide," *Applied Physics Letters*, vol. 92, May 2008.

[11] E. Furusawa and W. Cutting, "DETECTION OF VIRAL DNA IN THE INCLUSION BODIES OF ECTROMELIA-INFECTED TUMOR CELLS WITH FLUORESCENCE MICROSCOPY," *Virology*, vol. 11, pp. 632-634, 1960.

[12] K. W. Dunn, et al., "APPLICATIONS OF RATIO FLUORESCENCE MICROSCOPY IN THE STUDY OF CELL PHYSIOLOGY," *FASEB Journal*, vol. 8, pp. 573-582, Jun 1994.

[13] E. S. Yeung, "Study of single cells by using capillary electrophoresis and native fluorescence detection," *Journal of Chromatography A*, vol. 830, pp. 243-262, Jan 1999.

[14] B. Liu and G. C. Bazan, "Homogeneous fluorescence-based DNA detection with water-soluble conjugated polymers," *Chemistry of Materials*, vol. 16, pp. 4467-4476, Nov 2004.

[15] J. Homola, "Present and future of surface plasmon resonance biosensors," *Analytical and Bioanalytical Chemistry*, vol. 377, pp. 528-539, Oct 2003.

[16] J. M. McDonnell, "Surface plasmon resonance: towards an understanding of the mechanisms of biological molecular recognition," *Current Opinion in Chemical Biology*, vol. 5, pp. 572-577, Oct 2001.

[17] W. Z. Song, et al., "Refractive index measurement of single living cells using on-chip Fabry-Perot cavity," *Applied Physics Letters*, vol. 89, Nov 2006.

[18] P. Domachuk, I. C. M. Littler, M. Cronin-Golomb et al., "Compact resonant integrated microfluidic refractometer," *Applied Physics Letters*, vol. 88, no. 9, Feb, 2006.

[19] A. Ashkin, "Acceleration and trapping of particles by radiation pressure," *Physical Review Letters*, vol. 24, pp. 156-&, 1970.

[20] A. Ashkin, "LASER MANIPULATION OF ATOMS," *Nature*, vol. 330, pp. 608-609, Dec 1987.

[21] A. Ashkin and J. M. Dziedzic, "OPTICAL TRAPPING AND MANIPULATION OF VIRUSES AND BACTERIA," *Science*, vol. 235, pp. 1517-1520, Mar 1987.

[22] A. Ashkin, et al., "OPTICAL TRAPPING AND MANIPULATION OF SINGLE CELLS USING INFRARED-LASER BEAMS," *Nature*, vol. 330, pp. 769-771, Dec 1987.

[23] S. B. Smith, et al., "Overstretching B-DNA: The elastic response of individual double-stranded and single-stranded DNA molecules," *Science*, vol. 271, pp. 795-799, Feb 1996.

[24] A. Constable, et al., "DEMONSTRATION OF A FIBEROPTIC LIGHT-FORCE TRAP," *Optics Letters*, vol. 18, pp. 1867-1869, Nov 1993.

[25] http://www.physics.nyu.edu

[26] http://www2.bioch.ox.ac.uk

[27] J. Guck, et al., "Optical deformability of soft biological dielectrics," *Physical Review Letters*, vol. 84, pp. 5451-5454, Jun 2000.

[28] B. Lincoln, et al., "Reconfigurable microfluidic integration of a dual-beam laser trap with biomedical applications," *Biomedical Microdevices*, vol. 9, pp. 703-710, Oct 2007.

[29] H. A. Pohl, Dielectrophoresis the behavior of neutral matter in nonuniform electric fields, Cambridge University Press, 1978.

[30] B. J. Kirby, *Micro- and Nanoscale Fluid Mechanics: Transport in Microfluidic Devices,* Chapter 17, Cambridge University Press, 2010. http://www.kirbyresearch.com/textbook.

[31] T. B. Jones, Electromechanics of particles, Cambridge University Press, 1995.

[32] H. Morgan and N. G. Green, AC Electrokinetic: Colloids and Nanoparticles (Microtechnologies and Microsystems), Research Studies Press Ltd; 1st edition, 2002.

[33] J. Muys, et al., "Biochip: Cellular analysis by atomic force microscopy using dielectrophoretic manipulation," *Japanese Journal of Applied Physics Part 1-Regular Papers Brief Communications & Review Papers*, vol. 44, pp. 5717-5723, Jul 2005.

[34] M. Borgatti, et al., "Dielectrophoresis based Lab-on-a-chip platforms for the identification and manipulation of rare cells and microspheres: implications for non-invasive prenatal diagnosis," *Minerva Biotecnologica*, vol. 19, pp. 43-49, Jun 2007.

[35] L. S. Jang, et al., "Single-cell trapping utilizing negative dielectrophoretic quadrupole and microwell electrodes," *Biosensors & Bioelectronics*, vol. 24, pp. 3637-3644, Aug 2009.

[36] K. Park, et al., "Dielectrophoresis-based cell manipulation using electrodes on a reusable printed circuit board," *Lab on a Chip*, vol. 9, pp. 2224-2229, 2009.

[37] M. W. Wang, "Using Dielectrophoresis to Trap Nanobead/Stem Cell Compounds in Continuous Flow," *Journal of the Electrochemical Society*, vol. 156, pp. G97-G102, 2009.

[38] R. Pethig, "Dielectrophoresis: Using inhomogeneous AC electrical fields to separate and manipulate cells," *Critical Reviews in Biotechnology*, vol. 16, pp. 331-348, 1996.

[39] B. G. Hawkins, et al., "Continuous-flow particle separation by 3D insulative dielectrophoresis using coherently shaped, dc-biased, ac electric fields," *Analytical Chemistry*, vol. 79, pp. 7291-7300, Oct 2007.

[40] M. D. Jaramillo, et al., "On-line separation of bacterial cells by carbon-electrode dielectrophoresis," *Electrophoresis*, vol. 31, pp. 2921-2928, Sep 2010.

[41] W. Wang, et al., "Selective manipulation of microparticles using polymer-based optically induced dielectrophoretic devices," *Applied Physics Letters*, vol. 96, Mar 2010.

[42] F. Yang, et al., "Dielectrophoretic separation of colorectal cancer cells," *Biomicrofluidics*, vol. 4, Mar 2010.

[43] J. Voldman, "Electrical forces for microscale cell manipulation," *Annual Review of Biomedical Engineering*, vol. 8, pp. 425-454, 2006.

[44] G. H. Markx, et al., "SEPARATION OF VIABLE AND NONVIABLE YEAST USING DIELECTROPHORESIS," Journal of Biotechnology, vol. 32, pp. 29-37, Jan 1994.

[45] J. Oblak, et al., "Separation of electroporated and non-electroporated cells by means of dielectrophoresis," in 11th Mediterranean Conference on Medical and Biological Engineering and Computing 2007, Vols 1 and 2. vol. 16, T. Jarm, et al., Eds., pp. 178-181 2007.

[46] L. A. MacQueen, et al., "Gene delivery by electroporation after dielectrophoretic positioning of cells in a non-uniform electric field," Bioelectrochemistry, vol. 72, pp. 141-148, Apr 2008.

[47] C. F. Opel, et al., "Quantitative Modeling of Viable Cell Density, Cell Size, Intracellular Conductivity, and Membrane Capacitance in Batch and Fed-Batch CHO Processes Using Dielectric Spectroscopy," Biotechnology Progress, vol. 26, pp. 1187-1199, Jul-Aug 2010.

[48] S. J. Withrow and E. G. MacEwen, Eds. Withrowand MacEwen's Small Animal Clinical Oncology, 4th Ed. Saunders/Elsevier, St. Louis, MO: 2007.

[49] http://en.wikipedia.org/wiki/Denaturation_(biochemistry)

[50] H. F. Lodish, et. al., Molecular cell biology, 6th ed. W. H. Freeman, chapter 4, pp. 117, June 2007.

[51] M. J. Farabee, TRANSPORT IN AND OUT OF CELLS,

http://www.emc.maricopa.edu/faculty/farabee/BIOBK/BioBooktransp.html

[52] WK. Purves, et. al., Life: The Science of Biology- 6th ed. Sinauer Associates, pp.316-317, 2001.

[53] S. B. Dev, et al., "Medical applications of electroporation," IEEE Transactions on Plasma Science, vol. 28, pp. 206-223, Feb 2000.

[54] H. Q. He, et al., "Micro pulsed radio-frequency electroporation chips," Bioelectrochemistry, vol. 68, pp. 89-97, Jan 2006.

[55] J. A. SMITH AND L. MARTIN, “Do Cells Cycle?,”, *Proc. Nat. Acad. Sci.* USA, Vol. 70, No. 4, pp. 1263-1267, April 1973.

[56] W. Fuller, T. Kiljan, A. Miller, L. Mundhenke and M. Eldeiry, senior design report spring 2010.

[57] T.D. Hardy and W.C. Earnshaw, *Cell Biology*, 2nd Ed. Philadelphia, PA: Saunders Elsevier, 2008.

[58] http://en.wikipedia.org/wiki/Cell_cycle

[59] C. Khanna, K. Lindblad-Toh, D. Vail, C. London, P. Bergman, L. Barber, M. Breen, B. Kitchell, E. McNeil, J. F. Modiano, S. Niemi, K. E. Comstock, E. Ostrander, S. Westmoreland, and S. Withrow, "The dog as a cancer model," *Nature Biotechnology*, vol. 24, pp. 1065-1066, Sep 2006.

[60] K. Hansen, and C. Khanna, “Spontaneous and genetically engineered animal models: use in preclinical cancer drug development,” *European Journal of Cancer*, vol. 40, no. 6, pp. 858-880, Apr, 2004.

[61] D. M. Vail and D. H. Thamm, “Spontaneously occurring tumors in companion animals as models for drug development”, In: Teicher BA, Andrews PA, eds. *Anticancer Drug Development Guide: Preclinical Screening, Clinical Trials, and Approval*, 2nd ed. Totowa, NJ: Humana Press; pp. 259-284, 2004.

[62] D. H. Thamm, “Miscellaneous Tumors: Hemangiosarcoma”, in Withrow and MacEwan’s *Small Animal Clinical Oncology*, 4th Edition, ed. S. J. Withrow and D. M.Vail, , Philadelphia: W.B. Saunders, pp. 785-795, 2007.

[63] W. L. Spangler and M. R. Culbertson, "PREVALENCE, TYPE, AND IMPORTANCE OF SPLENIC DISEASES IN DOGS - 1,480 CASES (1985-1989)," *Journal of the American Veterinary Medical Association,* vol. 200, pp. 829-834, Mar 1992.

[64] M. J. Day, V. M. Lucke, and H. Pearson, "A REVIEW OF PATHOLOGICAL DIAGNOSES MADE FROM 87 CANINE SPLENIC BIOPSIES," *Journal of Small Animal Practice,* vol. 36, pp. 426-433, Oct 1995.

[65] http://www.vet.uga.edu/VPP/clerk/frankhauser/index.php

[66] N. Smith Annette, Hemangiosarcoma in dogs and cats. In: The Veterinary Clinics of North America, Small Animal Practice, Advances in Medical Oncology. W.B. Saunders Co, Philadelphia, pp. 533-552, 2003.

[67] C. A. Clifford, A. J. Mackin, and C. J. Henry, "Treatment of canine hemangiosarcoma: 2000 and beyond," *Journal of Veterinary Internal Medicine,* vol. 14, pp. 479-485, Sep-Oct 2000.

[68] A. R. Lamerato-Kozicki, K. M. Helm, C. M. Jubala, et al., “Canine hemangiosarcoma originates from hematopoietic precursors with potential for endothelial differentiation,” *Experimental Hematology*, vol. 34, no. 7, pp. 870-878, 2006.

[69] B. A. Tamburini, T. L. Phang, S. P. Fosmire, M. C. Scott, S. C. Trapp, M. M. Duckett, S. R. Robinson, J. E. Slansky, L. C. Sharkey, G. R. Cutter, J. W. Wojcieszyn, D. Bellgrau, R. M. Gemmill, L. E. Hunter, and J. F. Modiano, "Gene expression profiling identifies inflammation and angiogenesis as distinguishing features of canine hemangiosarcoma," *Bmc Cancer*, vol. 10, DOI: 10.1186/1471-2407-10-619, Nov 2010.

CHAPTER 3 SINGLE CELL MANIPULATION

There are two kinds of manipulation of the cell position inside a microfluidic channel, cell immobilization which stabilizes a cell at a certain location for optical analysis and cell steering which guides one or more cells into different lateral positions of the laminar flow. The latter one could also be used for cell flow focusing or cell sorting.

3.1 Cell immobilization

Cell immobilization is an important integrated part of OFIS, for the data collection usually requires 6-8 seconds integration time to get a better signal-to-noise ratio (SNR). The design of the dielectrophoresis (DEP) trap [1] evolved as we developed more understanding on the electric field distribution induced by different trap geometry, as well as on the interaction between the trap and cells; the electrode designs were also related to or limited to the existing fabrication technique.

3.1.1 Planar designs

The first DEP trap design was inherited from the planar trap design proposed by Voldman [2] as shown in Fig. 3.1. The fluid flow delivered cells to the hallow square formed by electrode before the trap was turned on, and when the trap was on, the cell would be pushed back by the high electric field between the right edge of the square and the ground bar.

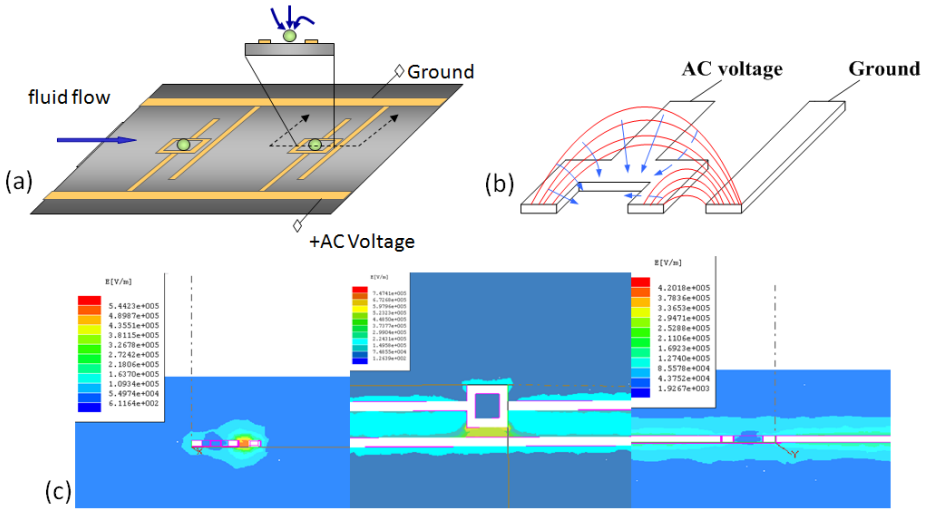

Fig. 3.1 (a) Configuration of typical Voldman trap inside a microfluidic channel; (b) illustration of the field lines (red) and the direction of DEP force (blue); and (c) 2-D field distribution simulations (Maxwell 3D®, Ansoft) at the cross-section and the top of the DEP trap, as well as along the flow direction.

As found out later, the Voldman trap provided very little DEP force to stop the cells, 10's of pN of force against liquid flows [3]. Therefore, only very low flow velocity (approximately 40μm/sec, based on experimental observations) could be used, and this raised great challenges to the flow control that delivered cells to desired locations. Even though typically high concentration of cell solution is requested (10^6-10^7 cells/ml), the cells are not evenly distributed in the suspension solution (PBS) and are more likely to settle at the inlet area or along the channel (before they reach the CCD camera viewing area) at this extremely low flow velocity.

And when cells show up in the viewing area, even though they followed the parabolic profile (which will be discussed in section 4.1.1), a good portion (60-70%) of the cells does not go through the trap area and are not able to be trapped or analyzed. So additional DEP traps were designed, such as revised Voldman to help bring the cells into the trap area, as shown in Fig. 3.2 below. More DEP trap designs and their purposes were described in the 08'-09' senior design final report [4]. This senior design group also helped with the design of traps and the mask layout of 16 OFIS chips with these trap designs.

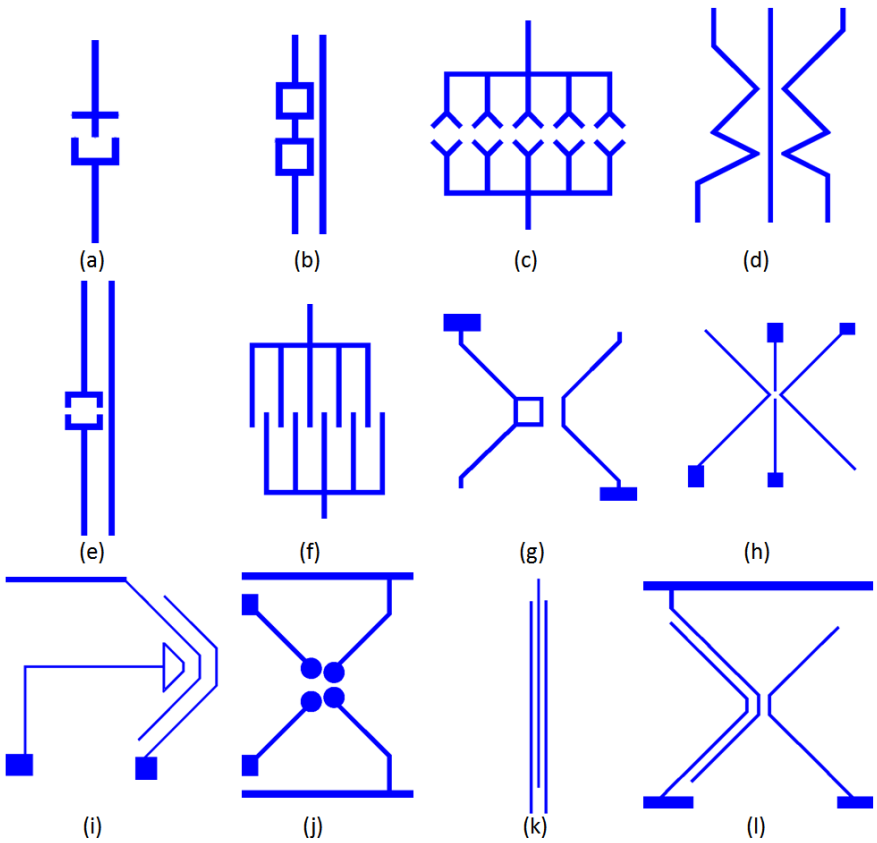

Fig. 3.2 Other planar DEP trap designs.

The majority of these designs are negative (as introduced in section 2.2.2) DEP traps that were designed to have AC signal between adjacent electrodes and to stop cells at the open area in between, except for the designs in Fig. 3.2 (d) and (f), which serve as positive DEP traps if the permittivity of cells and medium only allows pDEP to work in the electrical frequency range provided by the function generator. A few designs, such as the ones in Fig. 3.2 (g) and (i), are meant to reduce the joule heating around the trap area.

The major disadvantage of planar DEP structure is that very little DEP force (10's of pN) is generated against the fluidic flow, even though the maximum available AC voltage (on the function generator HP8116A) of 16V is used. So in order to trap cells with a planar DEP trap, extremely slow flowrate has to be used, approximately 40 μm/sec. The slow flow rate makes it very hard to control the flow without making the cells all settled or temporarily adhere to the channel bottom, or to find cells in the limited viewing area under the microscope (even with high cell concentration solution of 10^6 – 10^7 cells/ml) of about 1mm along channel length.

With the modeling and simulation from COMSOL Multiphysics (formerly FEMLAB), completed by Joel Kindt, a senior design and master student, the electric field distribution of DEP traps inside a microfluidic channel was simulated. The simulation result promoted the 3-D DEP trap designs discussed in the following section.

3.1.2 3-D designs

The major technical difficulty of having 3-D trap design was the chip fabrication. This includes patterning electrodes on both glass pieces while keeping a fluidic channel in between, the alignment between top and bottom electrodes, and the optical properties of the bonded chip, which will be discussed in detail in Chapter 4. After this difficulty has been overcome, a few 3-D DEP traps have been designed and fabricated for cell experiments of different purposes (including optical analysis and cell deformation test). With the 3-D electrode structure, cells now can be trapped at much lower voltage such as 6-8 VAC, while under a yet higher flowrate of typically 100-200 μm/sec, or up to 350 μm/sec in the center of the channel (which is the speed users usually observe, due to the parabolic velocity profile of the flow), depending on the channel depth and the trapping voltage used.

Fig. 3.3 shows the COMSOL simulation of the electric field around the DEP trap area, where the electrodes are 25 μm apart, in a 25 μm deep microfluidic channel, and the voltage applied is 5 VAC; the surrounding media used here is PBS, and the top and bottom layers are defined as borosilicate glass, which matches the actual structure of OFIS chips and the typical experimental conditions. Comparing the simulation result, one can find out that in the planar structure, the ∇E^2 component in the DEP force equation would push the cells towards the top of the channel, with the electric field that pushes against the fluidic flow being weak; on the contrary, the 3-D trap offers a well-confined area in the middle of the 4 electrodes, where the electric field is as weak as the

area far away from the DEP trap and the cells would have to overcome a greater barrier to escape, as shown in Fig. 3.4.

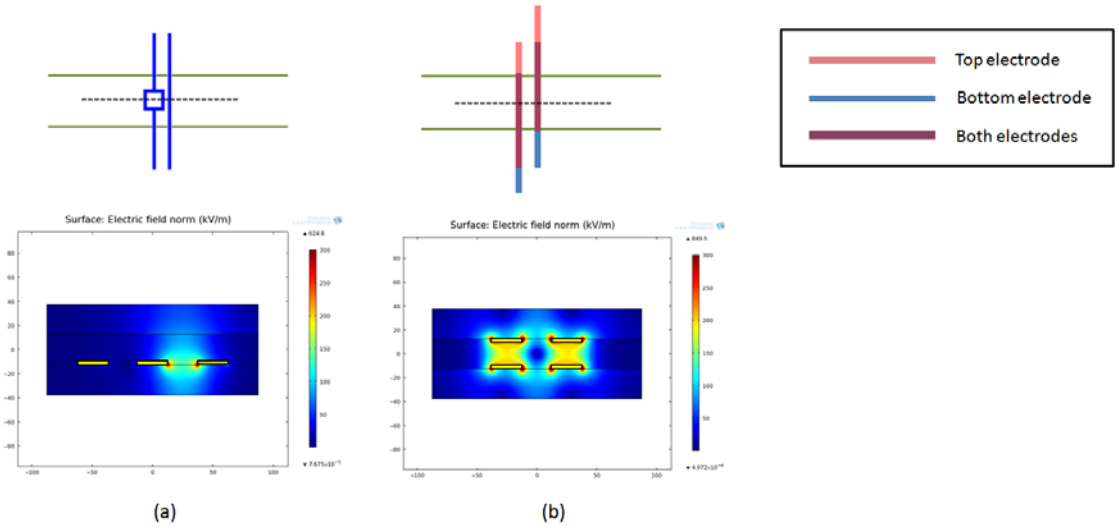

Fig. 3.3 Simulated electric field distribution of (a) a planar Voldman trap; (b) a quadrapole trap, with the dashed line indicating the viewing cross section; the size and gap between the electrodes are not to scale. (Courtesy Joel Kindt)

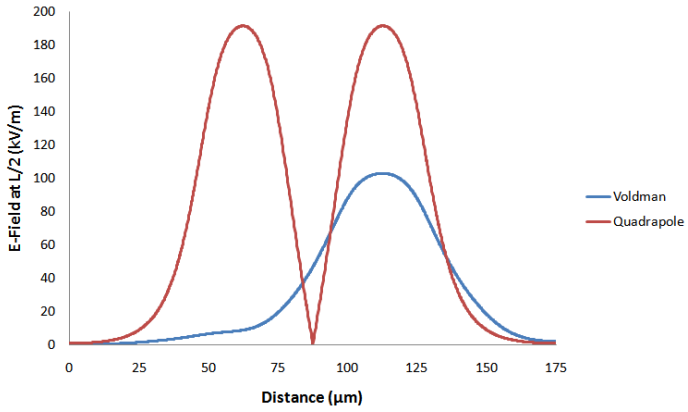

Fig. 3.4 Simulated electric field strength in the center of the channel (i.e., 12.5µm away from substrate and superstrate), along the dashed line in Fig. 3.3. (Courtesy Joel Kindt)

The structure of the first generation of 3-D quadrapole trap is illustrated in Fig. 3.5, and after flip-chip bonding, the 4 electrodes would line up and form the trap across the entire channel to immobolize the cells when the trap is activated. The glass substrate and superstrate are designed to have an offset to that the contact pads on the long edges of the glass chips would be exposed and could be soldered with wires or connected with card edge connectors.

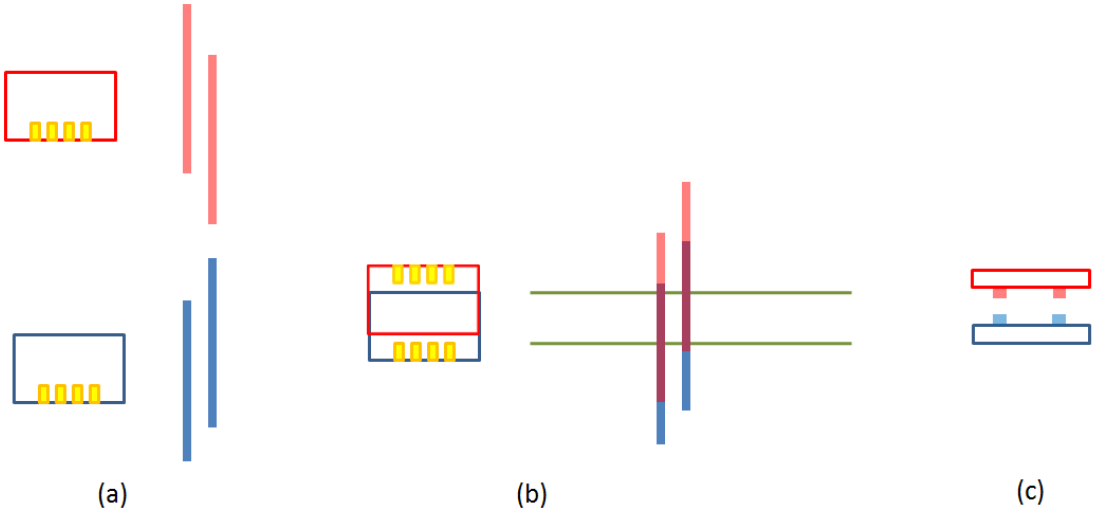

Fig. 3.5 (a) Design of the first generation 3-D quadrapole trap; (b) illustration of the trap on a flip-chip bonded OFIS sample, with the horizontal lines indicating the edges of the microfluidic channel; (c) a cross-sectional view of the bonded channel, with the electrodes on the top and bottom glass lining up and the fluid going in the horizontal direction.

The quadrapole trap works well on stopping cells from fluid with a flowrate of at least 100 μm/sec, except that there is no mechanism to stop the cells from drifting laterally inside the trap. Fig. 3.6 shows a lymphoma-OSW cell trapped in a quadrapole trap, and as the flowrate fluctuates, the cell would drift up and down in the lateral direction within the trap area. And since in a few seconds the cell could move out of the light collecting spot which should be aligned with the center of the cell, the spectrum collection which usually takes 6-8 seconds would be ruined.

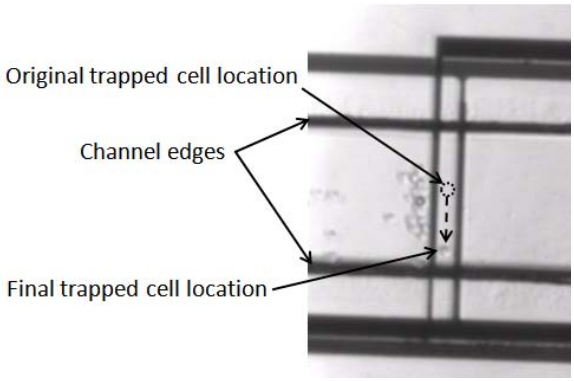

Fig. 3.6 A microscopic photo to explain the drift of a trapped lymphoma cell

To overcome this problem, the quadrapole trap design was then modified as shown in Fig. 3.7. As long as the fluid flow does not reverse, the cell would stay in the center of the trap; and in the experiments, cells did shift less than in the first generation quadrapole trap, but still could shift enough distance (varied with fluidic flowrate) to interfere the spectrum collection.

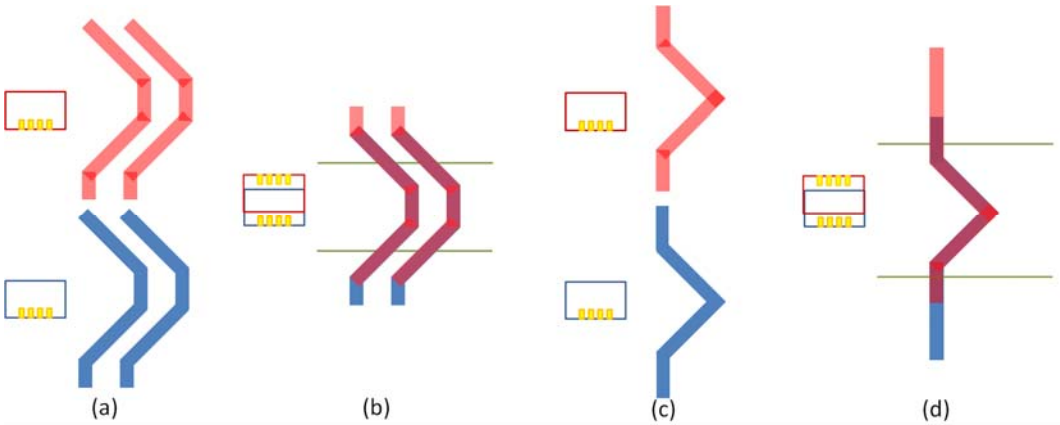

Fig. 3.7 (a) (c) Design of the second generation 3-D quadrapole and dipole trap; and (b)(d) illustration of the traps on a flip-chip bonded OFIS sample, with the horizontal lines indicating the edges of the microfluidic channel.

Another problem is that when the electrodes are kept on for a long time (longer than a few minutes), the joule heating would spread from the fluidic medium (PBS) into the epoxy that bonded the chip and cause an irreversible damage to it. Fig. 3.8 (a) shows the original trap area and (b) and (c) shows the damage after the trap has been left on or used for over 20 minutes.

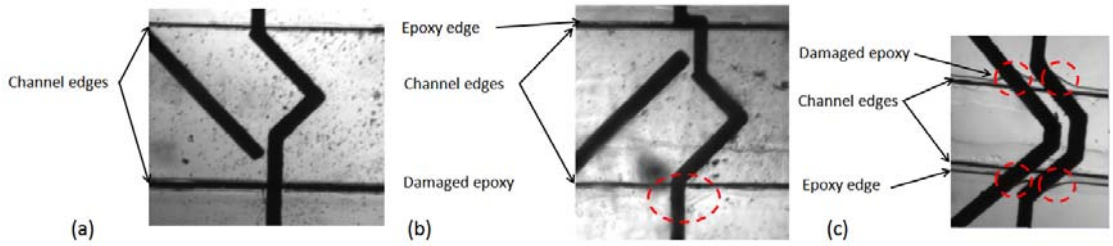

Fig. 3.8 Microscopic pictures of (a) Original trap area on an unused ACSU (automated cell sorting unit) chip; (b) a different set of trap that have been used on the same ACSU chip; (c) a used trap on an FTS (funnel, trap and steer) chip.

A third generation quadrapole traps as shown in Fig. 3.9 were designed to further optimize the performance of the 3-D DEP trap. The gap between the electrodes on the same plane was reduced to create a smaller trapping area where it left less room for the cells to drift. Moreover, the electrodes were shortened so that after flip-chip bonding, they would overlap in the middle of the microfluidic channel (in the lateral direction) only. In this design, the electric field would only exist wherever the electrodes overlap (between the superstrate and substrate) and at the fringing field, thus the joule heat generated by applying AC voltage on the electrodes would be as far away from the epoxy that bonded the chips as possible, to avoid exposing the epoxy to heat over time.

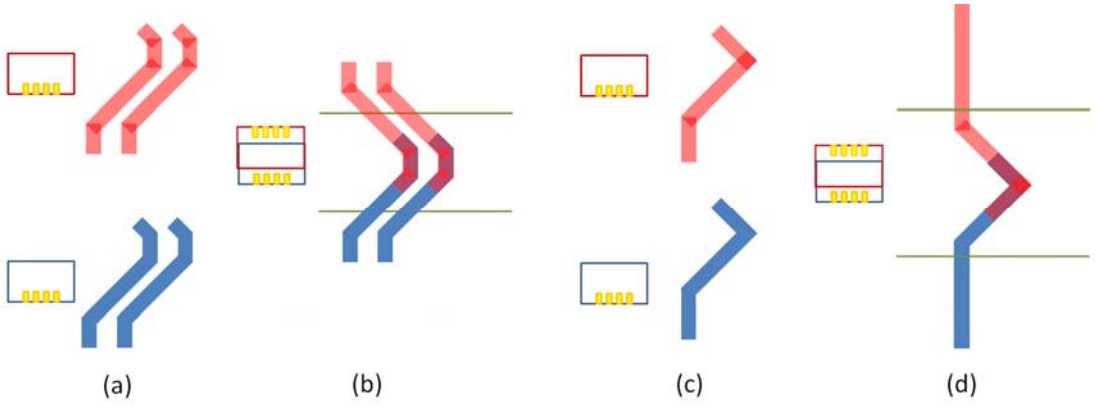

Fig. 3. 9 (a) (c) Design of the third generation 3-D quadrapole and dipole trap; and (b)(d) illustration of the traps on a flip-chip bonded OFIS sample, with the horizontal lines indicating the edges of the microfluidic channel.

3.2 Cell steering

Since with the latest design, the DEP trap could only immobilize the cells travelling in the middle 1/3 of the channel (in the lateral direction), some kind of cell steering electrodes are needed to move the cell flow to the desired location. Depending on the purpose of the chip, the steering structures could focus the cell flow, sort the cells into a side channel, or stop the unwanted cell from entering the data collection area.

3.2.1 Planar designs

Planar cell steering structures utilize the strong electric field created between two adjacent electrodes to push the cells to the lower ∇E^2 locations. Some of the cell steering DEP structures are shown in Fig. 3.10. As the fluid flows from left to right, the

majority of the structures shown focus the cells to the center of the channel, except for (b) that pushes the cells to the upper portion of the channel, for the purpose of sorting or steering cells away from the analysis area. And similar to the planar DEP traps, the planar steering electrodes only work when the flowrate is very low (approximately 40-80 μm/sec), and such flowrate would make locating the cell very hard.

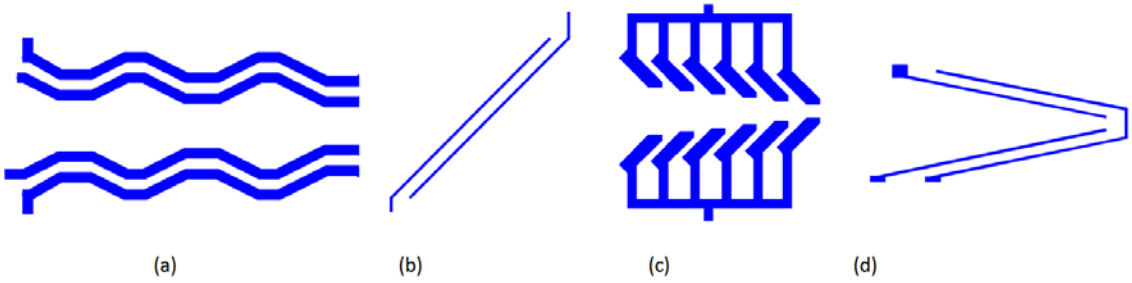

Fig. 3. 10 Other planar steering electrode designs.

3.2.2 3-D designs

Once the difficulty in fabricating 3-D traps was solved, designing 3-D cell steering structures was very easy. The only concern would be making sure even though some electrodes overlapped, they would not act as a trap and stop the cells. Fig 3.11 (a) (b) shows the funnel structure that focuses the cell flow to the center of the channel, although it could also be designed to get the cell flow to some other lateral positions, as long as it is aligned with the DEP traps after the cell-focusing structure, in the fluidic flow

direction. And Fig 3.11 (a) (b) shows the steering structure that once activated, pushes the cells to a side channel for sorting purposes.

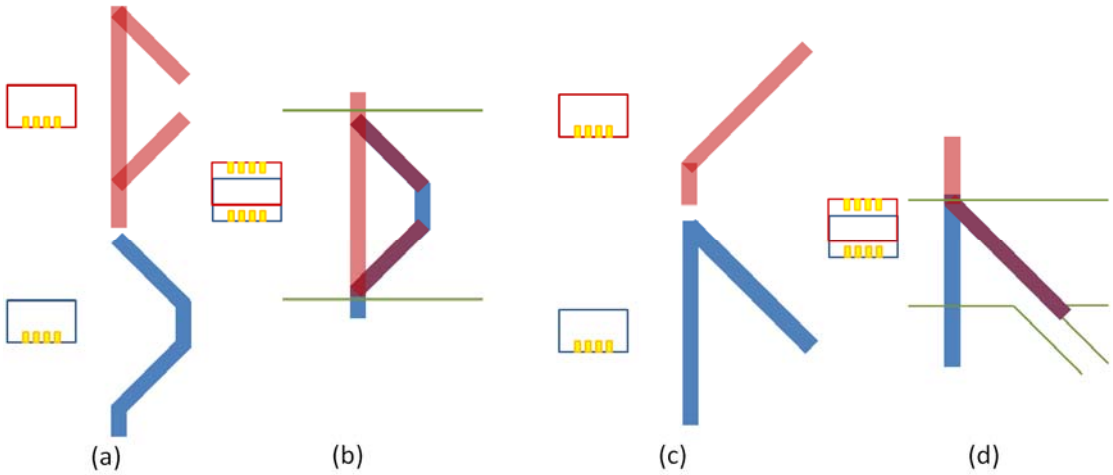

Fig. 3. 11 (a) (c) Design of the third generation 3-D dipole steering structures; and (b)(d) illustration of steering structures on a flip-chip bonded OFIS sample, with the horizontal lines indicating the edges of the microfluidic channel.

The sorting electrodes have a similar problem of letting the joule heating damage the cured bonding epoxy. It could be solved by moving the overlapping electrodes towards the center of the microfludic channel, however, this leaves an area near the channel edges where no electric field could affect the cell movement and making it impossible to focus the cell flow properly to trap and analyze every cell.

3.3 Summary of current mask design

The original motivation of introducing DEP structures into OFIS chip is to immobilize a cells at certain desired location so that the transmission spectrum of the cell, which usually takes 6-8 seconds (for better SNR), could be acquired. After experimenting with lots of planar structures, we realized that the DEP forces provided by planar traps were not sufficient to immobilize the cells moving at decent flowrate; so controlling the flow velocity and locating the cells became a trade off.

So the 3-D quadrapole structure was simulated and it was found that having electrodes on both substrate and superstrate would increase the electric field strength of the trap. After the difficulty in patterning electrodes on both pieces of glass while still keeping the microfluidic channel was solved, 3-D DEP structures were implemented in OFIS chip and were proved by sphere and cell experiments to efficiently immobilize particles while they were moving at a decent velocity of at least 100 μm/sec.

Over time the joule heating would damage the bonding epoxy and moving the electrodes towards the center of the channel would solve the problem. The funnel electrodes were then put in front of any trapping structures to focus the cell flow to a desired lateral position. Similar steering structure was also designed to realize the cell sorting function on some of the OFIS chips and it was also added to the front of the optical analysis area to steer away the unwanted cells.

Despite the effort to immobilize the cells at the center part of the quadrapole, the cells still move around inside the trap. During the experiments, depending on the flow rate, the trapping voltage and sometimes due to the possible damage in the electrodes, the trapped cell could move closer or even go underneath one of the two electrodes trap (as shown in Fig 3.12, position A), or move to the side while still being trapped (as shown in Fig 3.12, position B).

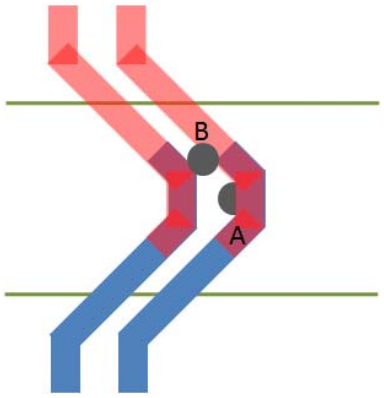

Fig. 3. 12 Illustration of trapped cell movement observed in experiments.

Currently there is no effective way to precisely immobilize cells at a specific location. However, other methods are being explored to facilitate automatic data collection, such as immobilizing the cells with antibodies.

References:

[1] R. Pethig, “Dielectrophoresis: Using inhomogeneous AC electrical fields to separate and manipulate cells”, Critical Reviews in Biotechnology 16, 331-348, 1996.

[2] A. Rosenthal and J. Voldman, “Dielectrophoretic traps for single-particle patterning”, Biophys. J. 88: 2193-2205, 2005.

[3] J. Voldman, “A Microfabricated dielectrophoretic trapping array for cell-based biological assays,” Ph.D. Thesis, MIT, 2001.

[4] J. Kindt, L. Netherton and H, Cutler, senior design report, spring 2009.

CHAPTER 4 DEVICE FABRICATION

The device fabrication is an integrated and very critical process to ensure the satisfactory fluidic, optical and electrical performance of an OFIS chip. The fluidic performance is mainly involved with the channel design and fabrication, which also affect the optical performance; both the optical and electrical performances are determined by the chip bonding technique. Another related aspect is the attachment of nanoport, which provides fluidic inlet and outlet on an OFIS chip.

4.1 Channel designs and fabrication

To properly design and modify the dimension of a microfluidic channel, it is helpful to develop a basic understanding of the fluid dynamics, and this understanding also helps to explain the cells fluidic behavior observed in our experiments, which in turn affects the modification in channel design. The microfluidic channel can be patterned in different ways: on PDMS Polydimethylsiloxane) for testing chips with planar electrode designs, on Pyrex glass for OFIS chips and with SU-8 photoresist for OFIS chips with 3-D electrode designs.

4.1.1 Fluidic analysis

A basic understanding of fluid dynamics is necessary. This is not only because it is the fluid flow that delivers the cells to the spectrum acquisition location during the experiments, but also because the split ratio of the side channels to the main channel

will affect the sensitivity and specificity of the cell sorting process, if any (based on the chip design).

The profile of the fluid velocity inside a rectangular microscale channel should be parabolic, as indicated in Fig. 4.1, plotted with mathCAD by an independent study student [1]. Other bizarre fluid behavior has been observed, such as faster flow on the top or bottom 1/3 of the channel (in the lateral direction, observed with the camera on top of the optical system), instead of faster flow at the center of the channel; however, combining the DEP trap design (e.g., funnels) and the channel design eliminates this potential problem and focus all the cell flow into the center of the channel.

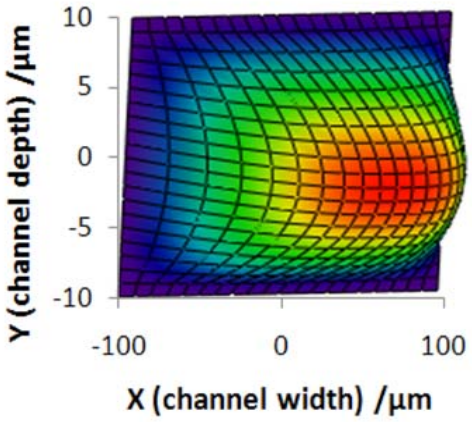

Fig. 4.1 Parabolic flow velocity profile in a 20µm (height) by 200 µm (width) channel (reproduced from [1]).

This flow velocity analysis indicates that there might be other problems occur in the microfluidic channel. An example is that the cells moving along the edges have a flow velocity very close to zero, and this will result in cells settling near the edges of the channel. When cancerous cells are flowing in the channel, due to their adherent nature, they will stick to the ones settling near the edges easily and eventually clog the channel. This problem cannot be avoided even when the average flow velocity is very high, such as over 1000 μm/sec.

4.1.2 Channel designs

The design of a microfluidic channel includes the size and shape of the inlet/outlet, and dimensional design such as the width and height of the channel for different applications. For the sorting purposes, the location where the side channels split from the main one and their widths and lengths affects the split ratio between the side and main channels.

To ensure better cell delivery to the channel, the inlet/outlet and the channel width design has changed over the past few years, as illustrated in Fig. 4.2 below. Comparing (b) with (a), the reduced reservoir diameter decreased the dead zone between the 2mm diameter inlet and the 200μm by 25μm channel so that fewer cells would get stuck in the inlet area; and the intermediate reservoirs were removed to ensure the constant flow rate through the entire channel, also to avoid the sudden stopping of cells due to the expansion of channel width. This modification did not necessarily benefit the optical

analysis on settled cells, but helps to maintain a steady flow across the entire chip. To further reduce the dead zone, the inlet channel was tapered in design (c). And as mentioned before, after the DEP funnel structure was integrated with the channel design and it was easy to focus the cell flow into the center of the channel and be analyzed there, a wider (400 µm) channel was then used to reduce the channel clogging issue.

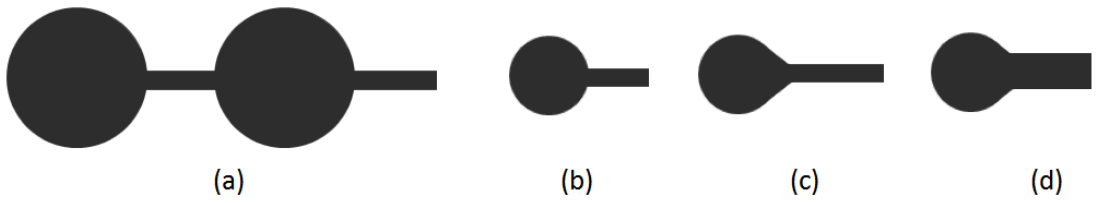

Fig. 4.2 (a) Original channel design with 2mm diameter reservoirs and 200µm wide channel; (b) modified design with 1mm diameter inlet; (c) modified design with tapered entrance; (d) modified design with tapered entrance and increased channel width of 400µm.

These channels can be patterned on or with different kinds of materials, according to the purpose of the chip being fabricated. At first the channels are defined on PDMS for electrode testing chips, then on Pyrex for OFIS chips and with SU-8 for OFIS chips with 3-D electrode designs.

4.1.3 Channel defined on PDMS

PDMS (Polydimethylsiloxane) is the most popular silicon based polymer used to define and seal microfluidic channels. Microfluidic channels are made by soft lithography techniques of first patterning a positive structure (mold) with SU-8 photoresist on a Si slide and then pouring a mixture of PDMS prepolymer–curing agent against the mold. The SU-8 has a very high viscosity (usually a few thousand cSt) and can easily form a mold with structure height ranging from 20 to 50μm, determined by its fabrication process. The fabrication process of the SU-8 mold is described below:

1. Clean a Si slide (approximately 2”×2.5”) with Acetone, Methanol and DI water; blow dry with N_2, bake on the hot plate @120 °C for at least 5 min;

2. Pour an even layer of SU-8 photoresist PR 2035 on the cleaned Si slide (make sure the first attempt covers the center area);

3. Make the PR reach the edge of the chip by tilting it slightly (note that wrinkles are BAD!);

4. Spin on PR with the speed shown in Fig 4.3 (ramp_1 = 100 rpm/sec determines how even the layer would be, ramp_2 = 300 rpm/sec determines the final layer thickness);

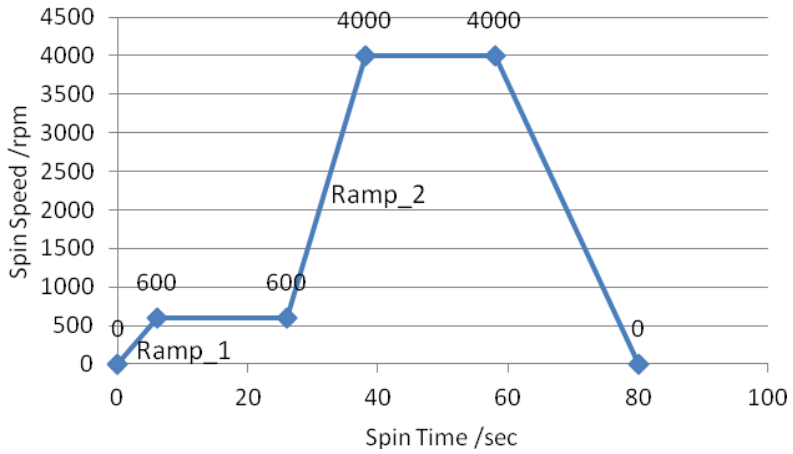

Fig. 4.3 Spin speed to achieve an even SU-8 layer

5. Soft bake @60-65 °C for 2-5 min (this evens out the defects , if any); then @90-95 °C for 15 min (until the PR is hard); let sample cool down to room temperature;

6. Expose with UV-34 filter for 190 mJ/cm^2;

7. Post bake @60-65 °C for 1 min, then @90-95 °C for 10 min, then ramp down to 60-65 °C for 2-3 min; let sample cool down to room temperature; if the exposure is adequate, the outline of the features will show up after 1min of 90-95 °C baking;

8. Use PGMEA(Propylene Glycol Methyl Ether Acetate) as developer, develop until unexposed area is clear (usually take 5-8 min);

9. Dispose PGMEA to solvent waste bottle immediately after use;

10. Before use, clean the mold by rinsing it with methanol, and then blow dry with N_2.

And the PDMS channel fabrication process is:

1. Take a plastic container (with lid) and put it on the scale, then turn it on (this would zero the scale reading);

2. Measure PDMS and its curing agent to a weight ratio of 10:1;

3. Stir slowly with a disposable stirrer to mix well;

4. Degas the mixture with a vacuum degassing pot, carefully check the bubbles coming out of the mixture through the transparent lid on the pot and make sure they do not overflow, the process is done when no more bubbles appear;

5. Pour adequate amount of the mixture into a mold loaded tray or dish, and make the mold as parallel to the fluid (gel) level as possible;

6. Degas the mixture in the tray or dish again;

7. Put the tray in the oven and bake @85 °C for 2 hours, or @65 °C for 4 hours to reduce its rigidity;

8. Use a Methanol cleaned razor blade to cut the cured PDMS and gently peel off the desired area; (for short-time storage, put the PDMS on another piece of cleaned Si slide);

9. Always throw away the first piece peeled off from a mold, it has very rough channel edges;

10. If done, seal the container and put it in the fridge (it could only last a few days, even in the fridge); if not, go to step 5 to make more pieces of PDMS.

Due to the elasticity property of the PDMS, no mirror or metal can be coated or deposited to its surface; thus the chip bonded with PDMS channel can only be used for non-OFIS experiments, such as testing DEP traps.

4.1.4 Channels defined in Pyrex glass

Channels can also be defined by etching into Pyrex glass. Since glass is more rigid than PDMS, dielectric mirror can be coated before the chips are bonded to form an optical cavity, thus glass channels are more commonly used in this project. In order to have the hydrofluoric acid (HF) react with the SiO_2 at the selected channel area but keep the rest of the chip intact, chrome (Cr) and gold (Au) layers are deposited and patterned with photoresist to protect the unexposed area. The fabrication process is described below.

1. Deposit Cr 35 nm, and then Au 150 nm;

2. Spin on photoresist PR 4400 at 3000 rpm for 30 sec;

3. Soft bake @110 °C for 1 min;

4. Edge bead removal (EBR) with acetone; or use a plastic EBR mask, expose and develop;

5. Expose under UV light for 400 mJ/area;

6. Develop for 90 sec;

7. Post bake @120 °C for 15 min;

8. Wet etch Au with Au etchant till golden color is gone, then etch Cr with Cr etchant till clear glass surface is revealed; etching usually takes 40-60 sec;

9. Dip the chip in 48% HF; keep stirring the HF solution without touching the surface of the sample for 3-4 min; HF etching speed is 5-6μm per minute;

10. Remove the protective layers (photoresist, Au and Cr) with acetone and then corresponding etchant.

With the HF etching, the channel depth can be relatively easily controlled by the etching time; although precise control is not possible, for the exact rate is also related to the freshness of the HF solution and the stirring process that affects how much fresh solution is in contact with the exposed glass surface.

Compared with the fabrication of PDMS, the HF etching process is slow (for it requires metal deposition and lithography of photoresist) and hazardous due to the corrosive nature and the toxicological property of HF. In addition, the HF etching is isotropic, so it would leave rough edges while the channel is being etched. And occasionally HF will etch through the protective layers and leave pinholes on the glass surface covered by the masks (Cr, Au and photoresist).

On the other hand, the etched channel bottom has a RMS surface roughness of 8.1nm (based on NSOM measurement of a 15μmx15μm area) and after mirror coating the RMS value decreased to 2.2nm, which theoretically corresponds to an extremely good cavity finesse of $F = \lambda/\left(2\sqrt{3}\sigma\right) = 116.78$ [2-4] with σ designating the RMS surface roughness and λ is the optical wavelength. And although the HF attacks all the exposed area including the back side of the sample, the flatness of the glass surfaces is not affected thus does not jeopardize the parallelism of the mirrors when two pieces of glass are bonded to form an optofluidic cavity.

4.1.5 Channel defined with SU-8

The quadrapole DEP trap design offers stronger electric field strength for cell trapping, however, it raises new challenges to chip fabrication. This design requires electrodes on the top and bottom pieces of glass, thus metal needs to be deposited and patterned on the superstrate and substrate. A few attempts were carried out with different photoresist (AZ1818, and AZ2070 for lift-off process) and different process flow to

pattern the electrodes on the channel-etched substrate. The electrodes patterned with AZ1818 were broken at the channel edges. As shown in Fig. 4.4, it appeared that with AZ2070, the photoresist layer is connected from the bar outside the channel area to the 5μm line at the channel bottom. After the lift-off process, the chip was examined under 20X microscope and the resistance of the electrodes was tested with the probe station. In Fig. 4.5, the metal lines (if any) on the channel edge looked dark because it was a top illumination microscope and since the edge was rough due to the isotropic HF etching, so light reflected on the rough channel edge are not captured by the camera. And in (c), the electrodes were much wider than 5μm, indicating that because of the depth difference between the glass surface and the channel bottom (20-30μm), the photoresist at the channel bottom is not in good contact with the photomask and light diffracted more in the gap and as a result more photoresist was exposed. Not only the electrodes turned out to be different than designed (both width and the gap in between), but the resistance testing later showed that the 5μm lines are not connected with the bus bar.

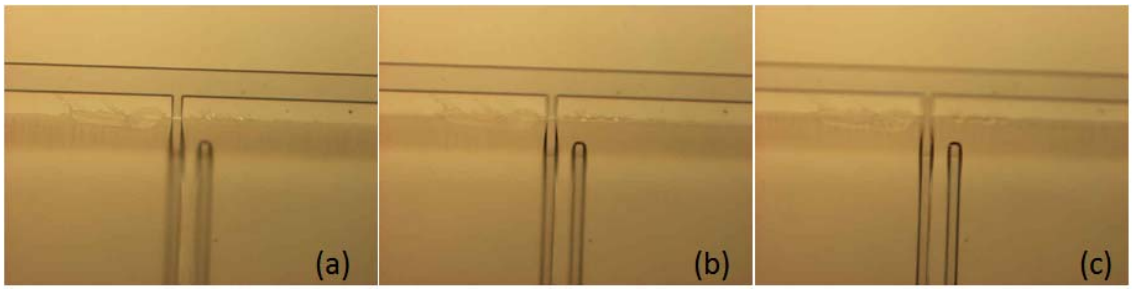

Fig. 4.4 Photoresist patterned with AZ2070, microscope focused on (a) the bus bar outside channel area; (b) channel edge; (c) the 5μm line at the channel bottom.

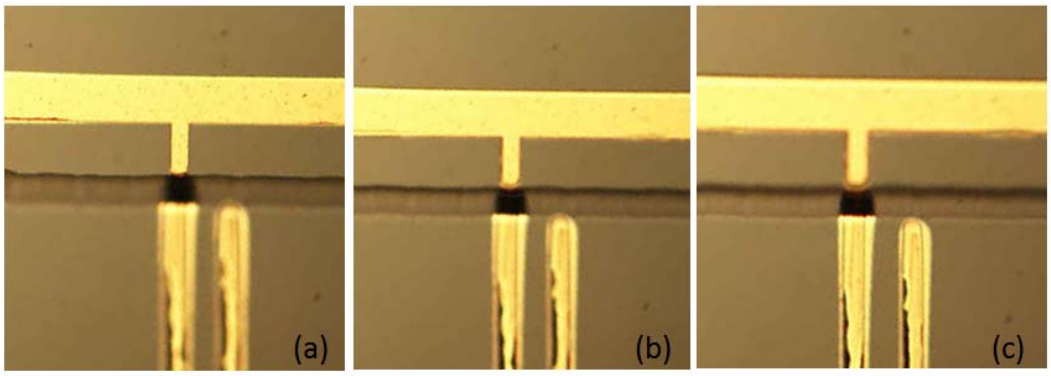

Fig. 4.5 Electrodes after lift-off process, microscope focused on (a) the bus bar outside channel area; (b) channel edge; (c) the 5μm line at the channel bottom.

So an alternative fabrication flow was in desire, where electrodes can be patterned on a flat surface on both the superstrate and the substrate, while still having a microfluidic channel in between, i.e., having some material separating the two pieces of glass. Meanwhile, in order to define a fluidic channel with inlet and outlet reservoirs and possibly with side channels, this material had to be UV patterenable.

The most available option was the SU-8 negative photoresist we used to make the PDMS mold. It is UV patterenable with the process described in section 4.1.3, but with a clear field mask that results in a negative image of the channel on the glass; and the channel depth can be controlled by the final spin speed of this photoreisist.

The viscosity of SU-8 3025 (4000 cSt) is high. This makes it very hard to achieve an even layer across the entire chip, especially at the edges and corners where the edge bead

could be 1 mm high and up to 2-3 mm wide, depending on the spin speed. The channel mask was then designed to have a large dark area (at least 5mm away from every edge of the glass chip) for the edge bead removal, as shown in Fig. 4.6. On the bottom the dark area is further from the chip edge, leaving enough space for the contact pads to be exposed. After photo lithography, this kind of mask would result a relative even layer of SU-8, and the majority of the surface can be used for chip bonding.

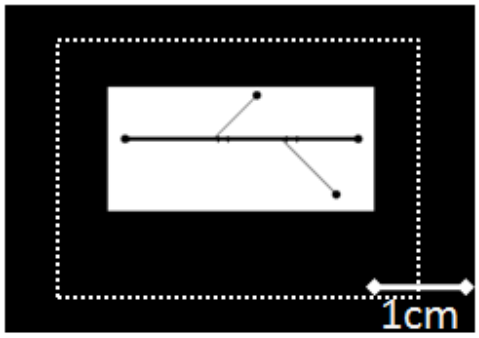

Fig. 4.6 Photomask with EBR for SU-8 channel patterning, with the dotted line showing the edges of a glass sample the mask needs to be aligned to.

In order to get a large area of flat SU-8, the first few steps of the process flow need to be changed as follows:

1. Clean the electrode-patterned glass sample (approximately 1”×1.5”) with acetone, methanol and DI water; blow dry with N_2, bake on the hot plate @120 °C for at least 5 min;

2. Pour an even layer of SU-8 3025 on it, make sure the first attempt covers the entire chip area with the excess SU-8 dripping from the edges;

3. Wait for at least 5min before proceeding, until all trapped air bubbles move up to the top surface or disappear;

4. Spin on PR with the speed shown in Fig 4.3, note that the relationship between spin speed and the final channel depth (thickness of the SU-8 layer) is different than what was given in the datasheet, Fig. 4.7 summarized the actually results measured with profilometer;

5. After spinning, soft bake @60-65 °C for 1min only, this will reduce the width of the edge bead.

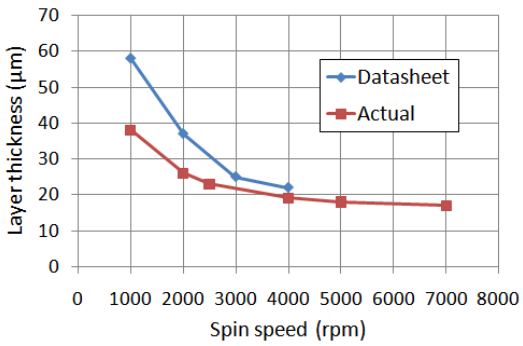

Fig. 4.7 Comparison on the relationship between spin speed and the SU-8 layer thickness.

In addition, a chip lifting device (CLD) was invented by a senior design student [5], Wesley Fuller and the device is as shown in Fig. 4.8. This CLD would be used whenever a chip needs to be picked up or transferred to a different location, until the SU-8 layer was developed and hardened. A CLD is required because when the chip is tilted or when a pair tweezers is used to pick up the chip, otherwise it leave wrinkles on the SU-8 layer.

Fig. 4.8 The chip lifting device

Compared with Pyrex glass etching, this channel patterning process is faster (although it still takes 2 hours) and not dangerous at all. However, the evenness of the SU-8 layer affects the chip bonding and the optical property of the bonded chip greatly, so it requires more practice, carefulness and the chip lifting device; and the patterning of small channels, for example, a 50μm wide channel, requires very careful control of exposure time, for overexposed SU-8 will stay and clog the small channel.

4.1.6 Comparison of different channel fabrication techniques

Every channel fabrication method has its advantages and disadvantages. Currently we are using the SU-8 to pattern the channel because we want to employ the quadrapole DEP trap design to stop the cells that are moving at a few hundred μm/s with a very low temperature raise in the trap area, so the Joule heating effect does not damage the cells. However, the flatness of the SU-8 layer is the bottleneck to achieve a good cavity finesse, which used to be 30 when the glass etching and the thermal compressive bonding method was applied [6]. Table I summarized the comparison between the channel fabrication techniques discussed above.

Table I Comparison of channel patterning methods.

Channel patterning methods	PDMS molding	Glass etching	SU-8
Process time	Reusable mold: 2 hrs; PDMS curing: 4 hrs	Evaporation for 10 piece: 2.5 hrs; Etching and removal of protective masks: 1 hrs	2 hrs
Major advantage	Fast; Repeatable; Clean edges.	Good surface quality after etching.	Easily adjustable channel depth;

Major disadvantage	Fixed channel depth determined by the mold.	Hazardous due to the requirement of HF; Rough edges.	Hard to ensure the flatness; Always leave a mess under the spinner and on the hotplate.
Allow electrodes on both sides?	No	No	Yes
Allow dielectric mirror coating?	No	Yes	Yes

It is possible that with a different photoresist or fabrication process such as filling the bottom of the channel with thick photoresist, the electrodes at the etched channel bottom could be developed as fine as the bus bar on the glass surface and they are connected across the channel edge, then we can go back to the glass channel, which will offer much better optical quality for the bonded cavity.

4.2 Microfluidic device bonding and sealing technique

The bonding of the two fabricated pieces and the sealing of the optofluidic device are crucial steps of the fabrication process. The bonding method determines the complete sealing of the microfluidic channel, which in turn affects the flow profile that is a great part of the performance of the chip. It also has a large influence on the resolution of the

optical cavity. Last but not least, the performance of the DEP electrodes is determined by the electrode alignment in this step.

4.2.1 Au-Au bonding

In Dr. Shao's prior work, the micro-scale optofluidic channel was sealed by bring two patterned glass slides together then performing a gold-to-gold (Au-Au) diffusion thermo compressive bonding [7]. Because of the bonding temperature of 350^{o}C and the pressure applied on the slides to bring them close enough to each other, not only a good parallelism of the mirrors could be achieved, but also the cavity length was readily determined by the channel depth, and the cavity rigidity to fluidic pressure was very good.

Since the sealing of the microfluidic cavity was realized by the diffusion of Au atoms to form a single Au layer between the two slides, uniform clamping forces and a smooth bonding interface were critical. Despite the efforts put in to ensure the cleanness and smoothness of the bonding interface, as well as the uniformity of the applied pressure, the Au-Au bonding sealed channels still had leakage problem. In addition to the bonding between electrode patterned glass slide and channel etched Pyrex slide with the normal bonding process described below, some of the other attempts were (a) attempt to bond with smaller (1" × 1") unpatterned slides, where the entire glass surface were coated with Cr and Au; (b) attempt to bond with two pieces of normal glass, in case the problem was the thermal expansion coefficient difference between Pyrex glass and

normal glass; (c) before bonding, clean the surfaces by dipping the slides in piranha solution for 5 min to remove residual photoresist or other debris that might interfere the contact between the surfaces; (d) in order to make sure that the pressure applied with the bonding plates as shown in Fig 4.9 (b) are uniform, measure the total thicknesses at the corners and edges, and adjust the screws so that these values are as close as possible.

The resulting bonding or sealing of the chip was not satisfactory. Some of the chips were crushed, some were not bonded at all, some were temporarily bonded but would fall apart when forces were applied to the interface or when fluid was put into the channel. There are other chips that had several points bonded across the chip so although they would not be broken apart, fluid would still leak out. And after shear test (introduced below) was carried out on those chips, it was found that at the bonded points, fractures of glass were broken off before the bonding between Au surfaces was separated. This was similar to what was observed in [7].

The following section describes the fabrication processes of Au-Au thermal compressive bonding between unetched, unpatterned, Cr and Au coated glass slides. In order to rule out the thermal expansion coefficient difference between normal experimental glass and Pyrex glass, both slides were of the same kind of glass.

1. After evaporation, clean the metal coated surface with acetone, methanol and DI water, then blow dry with N_2;

2. Bring the surfaces together, put them in between two small (1” square) copper plates and then on top of one large (3” square) aluminum plate, as shown in Fig. 4.9 (a);

3. Align the holes on the second piece of aluminum plate with the ones on the first plate, lay the second piece on top of the stack and tighten four screws to clamp the slides and form the bonding station shown in Fig. 4.9 (b);

4. Adjust the screws so that the two aluminum plates are tightly clamped, then use a caliper to make sure the pressure is uniformly applied, i.e., the total distance between the aluminum plates are similar across the bonding station;

5. Put the entire station into the furnace, pump down to 10^{-3} Torr vacuum level, then start the program that controls the temperature as shown in Fig. 4.9 (c);

6. When the heating program stops and the temperature decreases to room temperature, fill the furnace with N_2 and take out the bonding station.

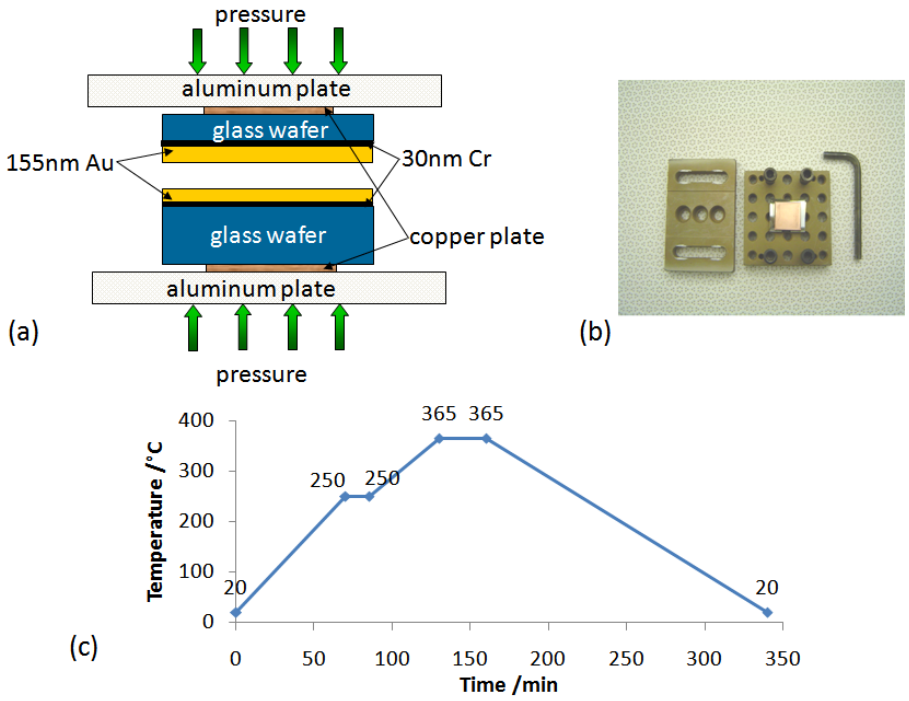

Figure 4.9 (a) Schematic diagram of thermal compressive gold-gold diffusion bonding station (Reproduced from [7]); (b) Optical plates that were used to apply uniform pressure to the glass substrates (Reproduced from [7]); (c) heating program setting on the furnace.

Shear test was carried out with the custom shear force test station (shown in Fig. 4.10) located behind the experimental apparatus in C9. Shear force was then calculated based on the ratio of the total gravity applied to break the bonding between the glass slides and the bonding area; the unit of shear force measured is Newton/cm^2.

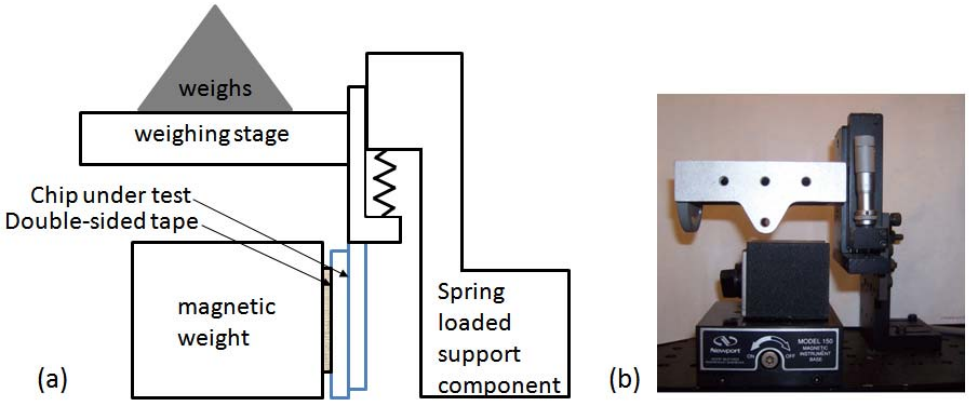

Figure 4.10 (a) Schematic diagram of the shear force test station; (b) picture of the station.

Although copper plates provided more uniform heat distribution due to copper's high thermal conductance, the subsequent failure analysis indicated that bonding primarily occurred on several spots along the outer edges, which was the reason why the chip had leakage problem when the fluidic pressure was increased to deliver liquid across the chip. An alternative bonding method utilizing the welding between indium and gold was then explored.

4.2.2 In-Au bonding

Two kinds of indium(In) plating methods were explored in attempt to provide smooth interface for the In-Au bonding. Generally, In is considered oxide free and has a unique ability to cold weld (or solder) to itself or cold weld a little to other metal, which is an

excellent property to ensure the electrode-channel alignment before and during the bonding process.

At first, the In was directly plated on the Cr/Au coated surface. The following section describes the plating process.

1. After evaporation, clean the metal coated surface with acetone, methanol and DI water, then blow dry with N_2;

2. Dip chip in 28-30% NH_4OH solution for 10 min, then rinse with warm water (heated up on the hotplate);

3. Dip chip in 10% HCl solution for 2 min to remove oxides, rinse with DI water, then blow dry with N_2;

4. Clean In strip with the plating solution, scrub it with a wipe until it shines, then clamp it with a pair of tweezers connected to the anode of the current source, as shown in Fig. 4.11 (a);

5. Use another pair of tweezers to clamp the chip and connected to the cathode, make sure that the metal side and the In strip is face to face and approximately 2 cm away;

6. Adjust the current density to 5.5 mA, then have the current source on for 4 min;

7. Cold weld chips immediately after In plating.

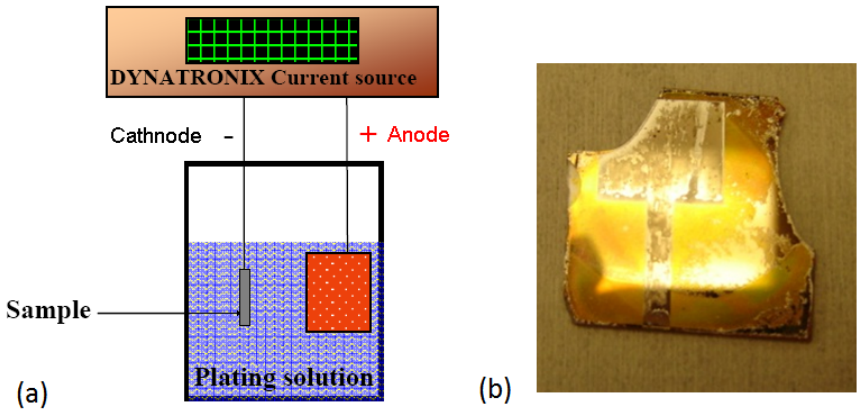

Figure 4.11 (a) Schematic diagram of the plating apparatus; (b) a picture of the partially plated slide with the central T-shape area exposed to plating solution and the rest of the slide covered by photoresist.

Although the mechanism of plating indicates that the In would be plated wherever there is Au atom present, the plated In film was very uneven, and it was especially thick on the edges. This was verified by plating on a Cr/Au coated and partially photoresist covered piece, result as shown in Fig. 4.11 (b), where the area appeared to be golden was covered by photoresist to verify whether the thicker plated In layer show up only on the edges of the plated area.

The flatness (the difference between the thinnest and thickest point across the sample) of the plated In layer, measured with surface profilometer(Alpha-Step ® 100), was 5-

11μm, which depended on the exact plating time and the current density used. Although the plated In could cold weld (solder) to the Au layer when the slides were brought together during the In-Au bonding, only the outer edges were in contact. It was initially anticipated that once the In was melted, it would be able to flow and create a more uniform layer, then fill the gap between two interfaces; however, it turned out that the In did not flow freely at all during the entire heating process.

Thus another In plating method was investigated in order to achieve a uniform In layer before bonding. This was achieved by plating copper (Cu) on top of deposited Cr and Au layer, then plating the In onto the Cu layer. Since the wetting property of Cu on Au is better than that of In on Au, it was more likely to get a uniform Cu layer first, and then it would be a lot easier to plate an even In layer on top of Cu.

The Cu plating apparatus was similar to the one shown in 4.11 (a), except for Cu plating solution was used both for slide cleaning and plating, and the plating was carried out for 5 min under the current density of 5.5 mA (for a 1" x 1.5" slide and a plating rate of 1μm/min). The In layer was plated immediately after the Cu plating, and the plating result is shown in Fig. 4.12 (a), where a very uniform In layer was achieved on top of a perfectly even Cu layer.

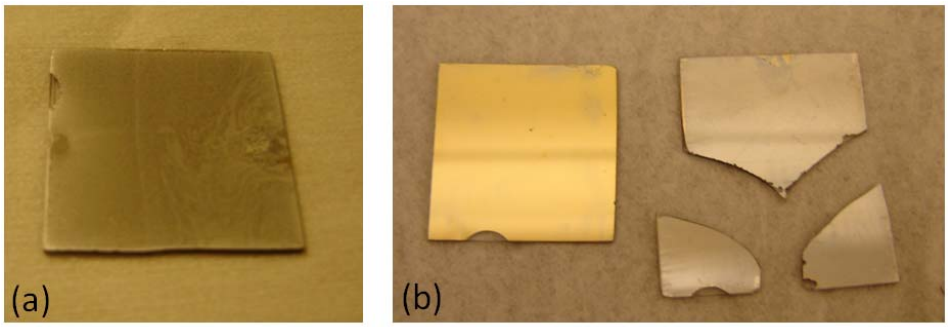

Figure 4.12 (a) A picture of the Cu-In plated slide; (b) a picture for the bonding failure analysis.

The bonding process between In-Au interfaces was basically the same with the one for Au-Au, except for the temperature required for In to melt (160°C) was a lot lower than the temperature needed make the Au atom become active and diffuse (350°C). As a result, the highest temperature in the heating process was set to 180°C, counting in the possible temperature difference between the heating strip in the furnace and the bonding station.

The permanent In-Au bonding was unsuccessful. Even with the uniform In layer, the bonding appeared to only occur at a few points on the interface; and it was noticed, as shown in Fig. 4.12 (b), that the In layer hardly changed after the bonding process, indicating that the In did not flow freely after it reached the melting temperature. This might be due to a thin In oxide layer formed very quick after the In was taken out of the plating solution, and the In_2O_3 had a very high melting temperature of 1910°C.

Several hypotheses and their corresponding solutions have been explored and summarized in Table II below.

Table II Analysis on hypothesis of In-Au bonding issues, solutions and results.

#	Problem	Hypothesis	solution	result
1	plated "cluster" instead of a even layer of In	plating surface is not clean enough	dip slide in piranha solution for 1min to clean the surface right before plating	same plating results
2		plating surface is not clean enough	descum with 30scum, 40W for 1min)	same plating results: only very little In was plated
3		different seed layer provides different sheer resistance	use Ti/Au instead of Cr/Au	formed slightly more uniform layer
4		Concentration of active ingredient is low	dissolve 21.9g 99% sulfamic acid (H3NO3S) powder in 200ml DI water, add this clear solution to the In plating solution	did not improve the plating result significantly (noticeably)
5	unable to bond In-Au	the force applied is not uniform across the slides	use caliper to measure the total distance between the Al plates at a few points, adjust screws to make the distance equal	did not improve the bonding result significantly (noticeably)

6		the copper plates are not in good contact with slides, so heat is not conducted well	clean and polish the copper plates	appeared to be bonded, but very easy to detach; only temporary bonding at a few locations
7		The In surface is not clean enough, or oxide forms	dip slide in 10% HCl solution for 10min before bringing the slides and let them cold weld	bonded, but very low yield
8		In does not bond to Au well	plate In on the other Cr/Au coated slide, effectively use In-In bonding	bonded with shear force of 24.3N/cm^2, however, channel depth would be too large

Although with In-Au bonding could be realized with one or more than one of the solutions 3, 5, 6, 7 and 8 in Table II, the total yield of the bonding was very low, making this bonding technique less preferred.

4.2.3 PDMS bonding

Using polydimethylsiloxane (PDMS) is a very popular technique to provide sealing for microfluidic devices. This polymer based material is clear and can be easily patterned with a mold on Si slide, which is created by photo lithography with SU-8 photoresist.

Treating the cured PDMS in the oxygen plasma activates the PDMS surface and enables the sealing between PDMS and glass.

The procedure for PDMS -glass bonding is described below. A PDMS channel can be produced with the fabrication process explained in section 4.1.3. Note that when pouring PDMS mixture into the mold loaded tray, the mold needs to stay as parallel to the fluid (gel) level as possible. Otherwise the thickness of the resulting PDMS piece will be very uneven, and makes it hard to align the channel on PDMS and the features on glass slide with a mask aligner.

1. Use a Methanol cleaned razor blade to cut the cured PDMS and gently peel the desired area off, then leave it on a cover slide with channel side up, as shown in the center part of Fig. 4.13;

2. Use oxygen plasma to treat the PDMS and the glass with micro-RIE, set O_2 rate to 100 sccm, and the power level to 25 mW, for 1min;

3. Align the channel on PDMS and the features on glass with mask aligner by placing the glass slide with electrode features on the stage, and taping the cover slide on another piece of glass slide held by the mask holder, as shown in Fig. 4.13;

4. After alignment, use the mask aligner to bring them together, release the vacuum on the mask holder and apply adequate force downwards, for 1min;

5. Take off the tapes and additional piece of glass slide and examine the quality of the bonding.

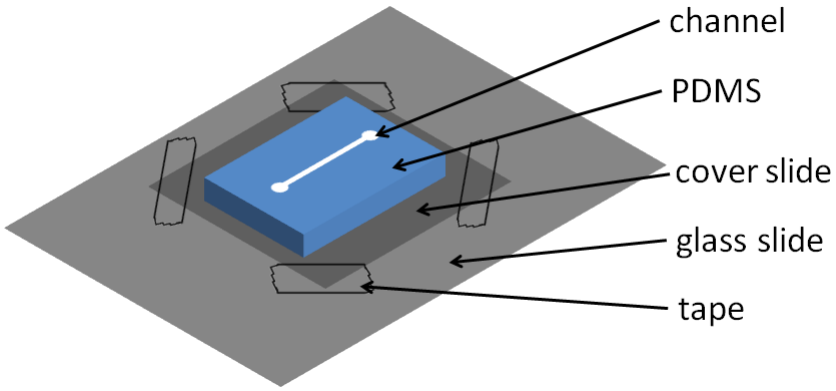

Fig. 4.13 An illustration of how to prepare the PDMS piece before bonding.

The yield of PDMS bonding was higher than that of In-Au bonding and once successful, the PDMS provided excellent sealing for the microfluidic channel and it was impossible to break it apart from the glass without damaging the PDMS. However, if the bonding was not 100% successful, i.e., part of the PDMS-glass interface was not attached permanently, there would be leakage problem and it cannot be fixed by oxygen plasma treat either of the surfaces again, for they were permanently bonded in some other area already. This happened even more often with electrode patterned glass slides, because the PDMS does not bond to metal as well as it would to glass. If the complete sealing could not be provided, then both the PDMS and the glass had to be discarded.

Another disadvantage of using PDMS as the sealing technique for OFIS is that the optofluidic cavity is achieved by coating dielectric mirrors on the top and bottom of the channel; however, PDMS does not provide a rigid surface for mirror coating, thus only DEP electrode testing was carried out with PDMS bonded chips.

4.2.4 Epoxy bonding

The current bonding technique used is epoxy based UV glue bonding of two pieces of glass slides. The clear, low-viscosity optical adhesive (NOA74, Norland) flows into the gap between the slides quickly due to capillary forces, especially after oxygen plasma treatment of the surfaces. And the glue can be easily removed with methanol if the parallelism of the mirrors is not satisfactory, the electrodes are not well aligned, or the glue gets into the channel. This idea and the selection of glue were first explored by David Sehrt in 2008.

NOA 74 was chosen because of its low viscosity (80-95 cps) and good to excellent adhesion to metal and glass. It can be cured by ultraviolet light with maximum absorption between 320-400 nanometers, and both the UV lamp and the mask aligner in the cleanroom offered this UV light within this range. The other UV glue considered was NOA 84, which had an even lower viscosity of 40-75 cps; however, it could be cured by ultraviolet light with maximum absorption within the range of 320-400 nanometers, as well as visible light between 400 and 450 nanometers. During the testing in the

yellow room, NOA 84 was slowly cured in 10-15 minutes. Since it usually takes one hour for the glue to spread in between two pieces of glass, this would be a bad choice.

The bonding with NOA74 becomes permanent with as little as 5min UV exposure of 15mW/area, and becomes robust after aging at 50°C for 12hrs. With the shear force test station introduced in 4.2.1 and all the weights available in the lab, no UV glue bonded chip could be taken apart.

The following section describes the epoxy bonding process.

1. Operate in the yellow room;

2. Clean glass slides with acetone, methanol and DI water, and SU-8 patterned piece with methanol and DI water, then blow dry with N2;

3. Use oxygen plasma to treat the glass slides with Micro-RIE, set O2 rate to 40 sccm, and the power level to 40 mW, for 1min;

4. Align channel with DEP features under the microscope on a mask aligner, make sure all the traps are aligned;

5. Apply UV glue (with a 1ml syringe and small needle) at a few spot along the chip edge, after it spread out, carefully flip the chip over and apply more at the other edges;

6. Check how the glue spreads in between the chip, make sure it stops at the channel edge; note that the UV glue might take 1-2 hrs to cover the entire bonding area;

7. Cure the UV glue by exposing the chip under 15mW/area for 5min;

8. Bake the chip at 50°C overnight or for 12 hrs to further link the glue.

It is recommended that the spreading of the glue to be monitored from time to time, so when it fails, one can start over in time. The glue can be rinsed off by methanol, which does not jeopardize the SU-8 layer (if any).

Another major advantage of this bonding method is that compared with thermal compressive bonding or welding between two layers of metal, the UV glue and SU-8 (if any) naturally provides an electrical insulation layer; this is an exceptionally useful feature when we decided to have a 3-D DEP electrode design. Having a non-conductive layer in between two slides also make complete sealing of the channel possible, contact pads can now run to the edge of either or both of the slides while the fluidic channel is fully sealed by the optical adhesive. An UV glue bonded chip is shown in Fig. 4.14.

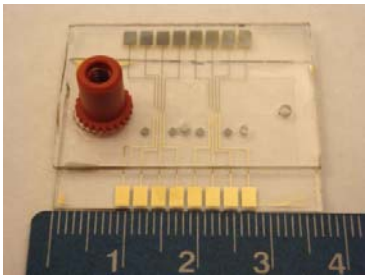

Figure 4.14 A picture of the epoxy bonded OFIS chip, with DEP electrode on both glass slides.

The majority of the epoxy bonded chips can be taken apart by soaking in freshly made piranha solution (H_2SO_4:H_2O_2=3:1), which removes the cured UV glue, the SU-8 layer as well as part of the metals but does not attack the dielectric mirrors; and the mirror coated piece can be reused.

Note that the UV glue needs to be store in the fridge (4°C) and has a shelf life of approximately 12 months.

4.2.5 Comparison of bonding techniques

Chip bonding of the two chips is a critical step in the fabrication of OFIS chips. The sealing of the microfluidic channel, the resolution of the optical cavity, as well as the performance of the DEP electrodes are all determined in this step. And for the bonding methods discussed above, the bonding results including the yield and the sustainability could vary significantly.

Table III summarize the major differences in the fabrication process and the results of the bonding methods.

Table III Summary of the fabrication process and the results of the bonding methods.

Bonding methods	Au-Au	In-Au	Cu/In-In/Cu	Au/In-In/Au	PDMS-glass	Epoxy
Mechanism	Thermo-compressive	In-Au com-pound; solder	In-Cu com-pound; solder	In-Au com-pound; solder	RF plasma surface activation	UV cured glue
Process Time	7 hrs	4 hrs	4 hrs	4 hrs	2 hrs	1-2 hr
Temperature required for the process	Ramp up to 365°C; ramp down	Ramp up to 180°C; ramp down	Ramp up to 200°C; ramp down	Ramp up to 200°C; ramp down	PDMS: bake at 60°C or 110°C	Bake at 50°C for aging
Major factor for channel depth control	Glass etching	Glass etching,and thicker In layer on the edges and corners	Cu and In layer thickness	After descum, In layer thickness	SU-8 mold	SU-8 spinspeed and flatness
Yield	40%	20%	0%	100%	70%	80%, bonding is reversible until 100% is reached

Sheer force	>25.5 N/cm^2	10.5 N/cm^2	N/A	13.9 N/cm^2	Permanent bonding	>24.3 N/cm^2
Channel parallelism	0.095^0	0.871^0	N/A	Did not measure	N/A	0.15^0
Complete sealing once successful bonding is realized?	Yes, but starts to leak after a few usage	No	N/A	Yes, but starts to leak after a few usage	Yes	Yes

In the end, because of the high yield and the electrical insulation provided by the epoxy bonding, this method was chosen to be the primary bonding method for all DEP OFIS chip fabricated after August 2008.

4.3 Nanoport™ attachment

Nanoport assemblies (Upchurch Scientific, cross-sectional view shown in Fig. 4.15) are the major fluidic delivery system applied to OFIS system. Nanoports are one of the few commercial products on the market for making on-chip microfluidic connections, and they are robust, easy to use, able to connect to standard tubing sizes (such as 1/32-in OD used in this project), and are particularly useful when connections are changed regularly. The fittings are constructed from polyetheretherketone (PEEK) and are

intended to adhere to glass or silicon surfaces using epoxy or a heat-curable adhesive ring.

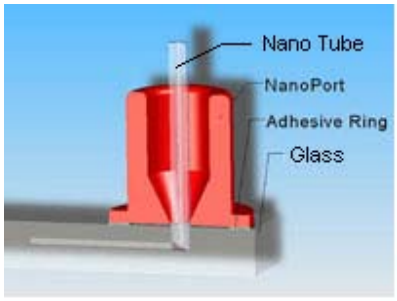

Fig. 4.15 A cross-sectional view of nanoport assemblies (reproduced from [8]).

In order to realize complete liquid sealing of the fluidic system, not only the microfluidic channel on the OFIS chips has to be sealed, but also the nanoport that provides fluid connection to the inlet /outlet of the channel has to be fully attached and sealed to allow no fluid to leak underneath it at the glass-nanoport interface. A few methods used to attach the nanoport, their advantages and disadvantages are summarized below.

4.3.1 Upchurch provided white adhesive ring

The first generation of white adhesive ring provided by Upchurch Scientific (N-100-01) is not adhesive at room temperature, but will cure after 1.5 hours at 121°C. Meanwhile, it is required that appropriate pressure to be applied on the nanoport during the entire procedure, so a binder clip is used to clamp the nanoport down on the OFIS chip before

it is put into the oven. However, the binder chip is opaque and this made the alignment between the fluid connection hole on the nanoport and the inlet hole very hard; what makes it worse is that one could not find out about the misalignment after 1.5 hours.

Another major disadvantage of this first generation of adhesive rings is that the sealing started to fail after a few experiments; although one could patch up the leakage point with silicone based sealant, it usually makes an area around the nanoport and on the chip no longer transparent; and the sealing does not work all the time.

4.3.2 Upchurch provided black adhesive ring

And then Upchurch came up with the second generation black, acrylic-epoxy hybrid adhesive ring, which is a little sticky even under room temperature. So after removing one side of the backing and sticking the adhesive ring to the bottom of the nanoport, one could easily align the fluid connection hole with the inlet of the channel before the nanoport is pressed down on the chip. The recommended recipe is after clamping the nanoport on the chip, either to leave it at room temperature for 24 hours or at 95°C for 1.5 hours.

Although the alignment could be ensured before the curing of the adhesive, it is still a rather long process and the robustness of the sealing is similar to that of the first generation adhesive.

4.3.3 Crystalbond^{TM} washaway adhesive

Typically crystalbond adhesives are ideal materials for temporarily mounting objects onto metals, glass and ceramics. This adhesive is in solid form and will melt and flow at 95°C. The alignment between the fluid connection hole on the nanoport and the inlet hole to the channel on OFIS chips has to be done when the adhesive is still warm and soft. And once the processing is complete, crystalbond adhesives can be easily removed by reheating and cleaning with acetone.

The mounting process is briefly described below:

1. Heat the chip on the hot plate at 100°C;

2. Grab a small piece (preferably with a pointy tip) of the crystalbond (break some from the cylinder if necessary) with a pair of tweezers;

3. Hold the adhesive close to the inlet hole area and draw a circle around the inlet, make sure there is enough adhesive on the glass;

4. Use tweezers to pick up and flip the chip, then align the channel inlet with the hole on the nanoport;

5. While the adhesive is still warm and soft, press down and hold for 20 sec;

6. Test the liquid seal with a syringe filled with DI water, if it is not ideal, restart by reheating the chip for 10 sec, then remove the nanoport and wipe off the adhesive from the chip and bottom of the nanoport with an acetone sprayed wipe.

The process takes no more than 10 minutes and the only difficulty is to press down the nanoport when the chip is still hot and the adhesive is soft, it could slide away from the inlet hole. If the alignment is not satisfactory, it is not very hard to take off the nanoport, clean up and restart.

The robustness of the mounting is not as good as the method that is going to be introduced below, if too much force is applied sideways on the nanoport, it could break the nanoport from the glass surface.

4.3.4 UV cured epoxy

So far the fastest way to attach a nanoport is to use the same epoxy used for chip bonding. Once the alignment between the nanoport and the chip is done, the chip can sit under the UV lamp, with the nanoport side facing down. Whenever necessary, another unattached nanoport can be used to support the chip. The epoxy will be cured in a few minutes; before curing, it can be removed easily with a wide range of solvent, such as acetone and methanol.

However, the low viscosity UV glue can get into the microfluidic channel and if it is not noticed before the curing, the UV cured glue would clog the channel and make the chip unusable because cured epoxy can no longer be readily removed by acetone. One can then imagine how robust the nanoport attachment is, but it then become a problem when he tries to remove the nanoport and switches it to a new chip. Although the bond can be broken by applying a lot of force, the cured epoxy sticks to the nanoport or the glass, such attempt would almost always contaminate the bottom of the nanoport but does not remove the epoxy completely.

4.3.5 Comparison of Nanoport^{TM} attachment methods

The nanoport attachment is the last step to ensure complete liquid seal of the fluid delivery system. Regardless of which adhesive to use, the nanoport needs to be able to provide fluidic seal to ensure the cells and media gets delivered to the microfludic channel. A brief comparison among different nanoport attachment methods is listed in Table IV below.

Table IV Summary of the major differences among the nanoport attachment process.

Nanoport attachment methods	White adhesive ring	Black adhesive ring	Crystalbond	UV Epoxy
Process Time	1.5 hrs	2 hrs	10 min	5 min

Temperature required for the process	121°C	95°	100°C	none
Yield	80%	60%	80%	90%
Duration	Good	Fair	Good	Excellent
Nanoport easy to retrieve?	Yes	Yes	Yes	No
Cost	$1.7 per pair	$2.1 per pair	Negligible	Negligible

References

[1] D. Trujillo, independent study paper, summer 2008.

[2] R. A. Briones, L. O. Heflinger, and R. F. Wuerker, “Holographic microscopy”, *Appl. Opt.,* vol. 17, pp.944, 1978.

[3] G. J. Sloggett, “Fringe broadening in Fabry-Perot interferometers”, *Appl. Opt.*, 23(14), 2427-2431, 1984.

[4] C. S. Vikram and M. L. Billet, “Aberration limited resolution in Frauhofer holography with collimated beams”, *Opt. Laser Technol.*, vol. 21, pp.185, 1989.

[5] W. Fuller, T. Kiljan, A. Miller, L. Mundhenke and M. Eldeiry, senior design report spring 2010.

[6] H. Shao, Ph.D dissertation, section 4.3 device characterization, 2007.

[7] H. Shao, D. Kumar, S. A. Feld, and K.L. Lear, “Fabrication of a Fabry-Perot cavity in a microfluidic channel using thermocompressive gold bonding of glass substrates,” *Journal of Microelectromechanical Systems*, vol. 14, no. 4, pp. 756-762, Aug, 2005.

[8] C. Koch, J. Ingle, and V. Remcho, “Chips & Tips: Bonding Upchurch® NanoPorts to PDMS”, *Lab on a Chip,* 2008.

CHAPTER 5 EXPERIMENTAL APPARATUS

This chapter briefly reviews the experimental set up of the OFIS system, including the hardware configuration summarized in section 5.1, and the software control reviewed in section 5.2.

5.1 Apparatus overview

The hardware configuration of the OFIS system is involved with three major aspects: optics, fluidics and electronics. The optical alignment ensures the quality of the transmission spectrum collected (such as its location, intensity and finesse), as well as timely observation of cells inside the cavity. The fluidic control delivers the cells to desired locations in the channel, and proper cell removal is also very important to not only help reduce the cell debris in the OFIS chip but also facilitate other analysis after the cells going through the channel. The electrical configuration works with the on-chip electrodes to enable the automatic manipulation of cells with DEP forces.

5.1.1 Optical system

Understanding the optics involved with OFIS system is a critical step to understand how the apparatus worked, to adjust the optics accordingly for better system performance, and to improve the signal to noise ratio (SNR) of the acquired OFIS spectra. The major components of the optical system required to obtain OFIS spectra are illustrated in Fig. 5.1. The optical components are, following the optical path: an infrared light emitting

diode (LED) centered at 890nm, the mirror-coated OFIS chip (that formed an optical resonant cavity), a microscope with objective lends and a spectrometer; another focusing lens is usually used in front of the LED to increase the total power shined on the OFIS chip. And in order to line up the cell with the light collecting spot whose size is comparable with a cell, a 50/50 splitter and a CMOS camera is located on the top of the system to provide visual image of a selected area on the chip.

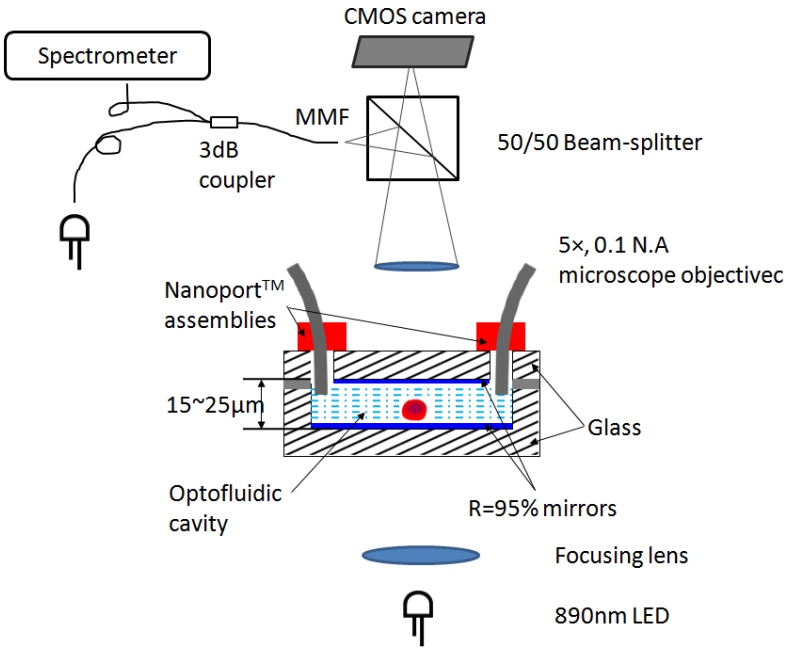

Fig. 5.1 Schematics of the optical system for OFIS.

The system works as follows. First, the light from an infrared LED (L2690-02, Hamamatsu) whose wavelength peak centered at 890nm is focused through the cavity of the micro-fluidic channel on the chip. Even though the light is focused to increase its intensity at

the chip plane, it still covers a large area (approximately 1.5mm^2) on the chip. The light then passes through the OFIS chip and the transmitted light relayed by a 5x objective lens (N.A. = 0.1) is directed to a fiber coupled spectrometer (HR2000, Ocean Optics). The multi-mode fiber (MMF) optical cable into the spectrometer acted as a spatial filter with a 10µm - 15µm diameter (similar size as cells) image in the plane of the channel. The core image is aligned with individual cell positions by translating the entire chip relative to the optical system, so that the majority of the optical signal collected with the spectrometer is from an area comparable with that of an individual cell. An industrial CMOS camera (scA640-74, Basler) is added to the system to provide visual confirmation of the location of cells, as well as the alignment between the light collecting spot and the cell under investigation. A full instruction for optical adjustment is given in Appendix A.

The optical system needs to be adjusted so that effective optical data collection could be carried out. It is aligned in a way that the LED focused on the rectangular opening on the transition plate where the chip is sitting, and the alignment between microscope lens and the LED could be confirmed with top illumination light. Another preferred match, for user's convenience during the experiments, is the optical length between the focusing plane of the optical fiber and that of the CMOS camera. After the 50/50 beam splitter, these optical lengths need to be identical for the image of the MMF core, i.e. the spatial filter, to be focused on the plane where cells pass through and for the camera to provide visual conformation. Since the position of the camera is already determined by distances from the lens to the image, an adaptor translation mount

(Thorlabs) was purchased and attached by Hua Shao to the left side of the microscope, so that the end of the MMF could be adjusted horizontally and vertically by adjusting the two screws that translate the entire mount. This adaptor is also capable of moving to the front and back to make sure the image of the fiber, when it is imaged on a reflective surface on the object plane, is within the viewing area of the camera. As shown in Fig. 5.1, another infrared LED and a 3dB coupler was added to the system to provide instant visual confirmation of the image of the light collecting spot. A detailed guide for optical alignment is summarized in Appendix B.

The HR2000 is a high-resolution fiber optic spectrometer and compatible with USB interface. It provides optical resolution of 0.035 nm (Full-Width-at-Half-Maximum) in the wavelength range between 865nm and 1025nm. The dark signal could be subtracted based on the integration time chosen; and the SNR is dependent on the integration time, which is typically chosen between 6 to 8 seconds.

The infrared LED of model L2690-02 from Hamamatsu is chosen, because it has a few preferred features. This model has a large forward current (I_F = 100mA) and a small directivity of ±10° with radiant flux of 9mW.

An industrial camera (scA640-74, Baslar), instead of a webcam is used, because it offers an acquisition rate of up to 74 frames per second (fps), when the resolution is 659 x 494, compared with webcam's 30 fps with 640 x 480 resolution. And it has much better sensitivity and low noise in the infrared range.

In order to image the light collecting spot, one could add a 3dB coupler in front of the MMF leading to the spectrometer and back illuminate from one arm of the 3dB coupler with another infrared LED (as shown in Fig. 5.1). And if the focusing planes of the camera and the chip with a reflective surface is identical or close enough (within 1mm in the vertical direction), the image of the MMF would show up as a bright spot, as shown in Fig. 5.2. The size of this spatial filter is determined by the core diameter of MMF and the magnification of the microscope lens by

$$Size\ of\ light\ collecting\ spot = \frac{MMF\ core\ diameter}{lens\ magnification} = \frac{62.5\mu m}{5} = 12.5\mu m$$, which is comparable with the size of cells.

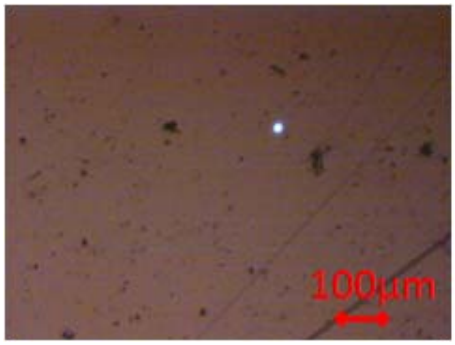

Fig. 5.2 Example image of the MMF on a reflective surface (such as a mirror coated glass slide or an OFIS chip) with top illumination on the chip, when the fiber was back illuminated by a separate infrared LED.

5.1.2 Flow control

An essential and integrated part of the project is the flow control. It includes a few aspects: to be able to get cells into the chip without leaking, maintain a constant fluidic flow, and deliver the cells to desire locations, as well as take the cells out of the chip without clogging the channel. If further analysis of the cells pass through the channel is required, proper cell removal from the microfluidic channel and gathering at the channel outlet may become important.

The primary fluidic delivery method used is nanoport assemblies (N-126H or N-126S, Upchurch Scientific) and nanotubes (PEEK T-1576, Upchurch Scientific) with various inner diameters, as illustrated in Fig. 5.1. The N-126S has a flat top which would make it easier to completely tighten the connection between the assemblies; and the PEEK T-1576, whose inner diameter is 125μm, is chosen so that the tube is not too narrow to be clogged easily, or too wide to raise new challenge to the flow control (such as the resulting increased flow volume within a certain amount of time, when the flowrate is required to be kept relatively low so that the cells would settle, or be trapped easily). The other end of the nanotube is connected to a syringe (1ml or 3ml with luer lock adaptors) run by a custom syringe pump (Oriel Instruments Encoder Mike Controller 18011). The complete sealing of the entire fluidic system critically relies on the bonding of the chip and the nanoport attachment, which was discussed in details in section 4.3 of chapter 4.

There are several considerations for acceptable means to accomplish the desired flow rate of cells in the microfluidic channel. The first and primary requirement is that the flow rate must be less than or equal to 40 μm/sec for 2-D traps, or 100-200 μm/sec for 3-D traps, based on the observations made during the experiments. This requirement comes from the DEP force strengths determined by the configuration of the DEP traps on the chip. If the flow rate exceeds the above values, the force of the DEP trap would not be sufficient to stop a cell and hold it in place. Conventional continuous pressure driven flow would result in excessive flow velocities of well over 1000 μm/sec and might cause clogging at the beginning the microfluidic channel, where the cross-section area is greatly reduced from the 1mm diameter inlet to the 200μm wide channel. To avoid clogging, a low flowrate is achieved at the beginning of each experiment by running the syringe pump with a small duty cycle, typically 10-20%, controlled by the LabView program developed by senior design students, which will be discussed later in section 5.2.1. Steady flow is observed even under pulsed drive conditions due to compressible air space in the syringe combined with the low conductance of the nanotube and microchannel acting as a low pass mechanical frequency filter.

The delivery of the cells to desired locations where their transmission spectra could be collected is achieved by one of the two methods described below. The first one is used when spectra of settled cell are collected. After flowing cell suspension through the nanotube into the channel, the syringe pump is stopped and manual control of the syringe (by very gently pushing or pulling it, according to the flowrate observed with the camera) is used to further slow down the flowrate, until minimal velocity is achieved

and some cells temporarily settle on the channel bottom. The second one is to use cell manipulation methods, in our case, the dielectrophoresis (DEP) traps. As soon as cells approach the trapping area, a funnel structure focuses the cell flow before a DEP trap immobilizes an individual cell at the center of the trap. In the latter case, and especially when 3-D DEP structures are used, the flowrate could typically be much higher, approximately 100-200 μm/sec, thus offers a slightly better throughput for the fluidic system.

There are two major ways to extract the fluid from the outlet of the microfluidic channel. One is to leave the outlet area open and simply let the liquid evaporate from the outlet area. And if the flowrate is too high, use a Q-tip or tissue paper to remove the excess liquid. This method does not effectively remove the majority of the cells coming out of the system. The other way is to attach another set of nanoports assemblies and nanotubes at the channel outlet, as shown in Fig. 5.1, and collect the fluid coming out of the outlet with a vial.

Whether the fluidic flowrate is low or high, or whichever fluid extraction method is used, it seems that a dead zone always exists near the inlet or outlet of the microfluidic channel. Part of the clogged cells could be removed by flushing the channel with methanol or even bleach (1:10 diluted with DI water), but the rest would stay attached to the glass and eventually clog the channel after 2-8 cell experiments, depending on the channel depth. Although a shallow channel is preferred for the stability of optical resonators [1], it is more easily clogged by cells, especially when their size is comparable

to the channel depth, such as HSA cells in a 16 μm deep channel. Other channel outlet configurations, such as an open outlet that let the fluid flow horizontally out of the channel, are under investigation to reduce the dead zone and make it easier to collect more percentage of the cells going through the microfluidic channel. Currently the cell retrieval rate of using an outlet nanoport connecting to a vial is about 20%-40%.

Another critical aspect of flow control is the exclusion of air bubbles in the system, because their appearance would affect the flowrate or even the local velocity profile near the bubbles. According to [2], using the PDMS channel could usually avoid this problem, for the air bubbles trapped would vanish through the PDMS ceiling as the microfluidic channel is pressurize. This matched with what was observed during the experiments: hardly any air bubbles were found in the channel formed by bonding PDMS onto glass. However, no optical coating can be deposited on the elastic PDMS surface, so after switching to glass channel, air bubble elimination becomes a key step before any experiments, so that the fluidic system would start bubble-free. A detailed instruction can be found in Appendix B, which was modified from [3], appendix L.

5.1.3 Electric connection

The initial electrical connection from the function generator to the electrodes on the OFIS chip was to realize manual DEP trapping. This was done by soldering wires on the gold pads on the edges of each chip and then making the connection with coax cable and test clip leads. The AC signal (including voltage and frequency) applied to the DEP

electrodes was set on the function generator and could only be manually enabled or disabled. This was due to the trap design and one had to wait until the particles entered the trapping area before turning on the trap.

The manual trapping motivated the idea of an automated trapping system and related circuit design. This part was realized and implemented by the senior design students from 2008-2010 [4-5]. Fig. 5.3 briefly describes how the system works. The repetition spacing between the pads on the OFIS chip was designed to be 0.1" (2.54mm) so that electrical connection can be easily and steadily made before every experiment by inserting the chip into one or two card edge connectors (depending on the trap configuration), as shown in Fig. 5.4.

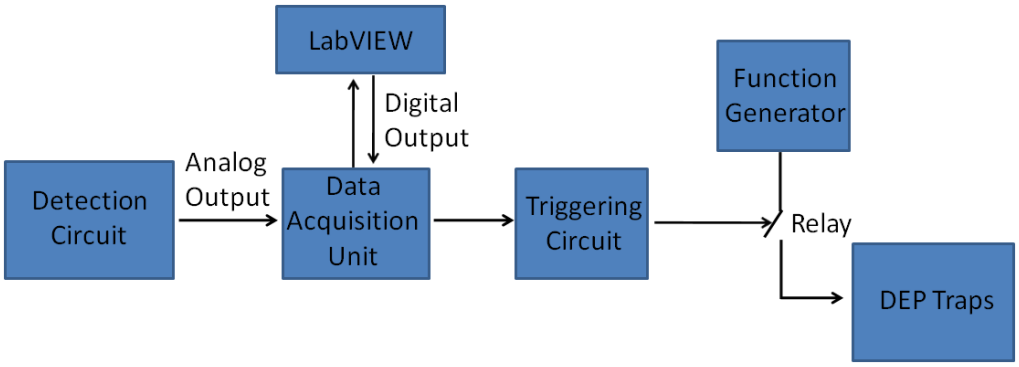

Fig. 5.3 Schematic diagram of automated trapping system (reproduced from [4]).

(a) 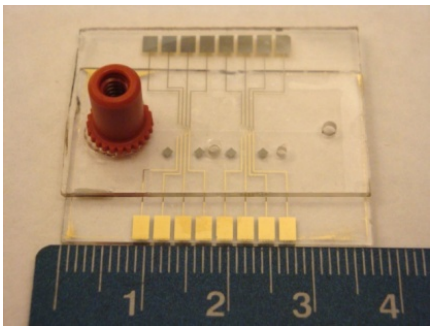 (b) 

Fig. 5.4 Pictures of (a) an OFIS chip with a ruler showing cm marks; (b) an OFIS chip with 3-D traps, mounted on card edge connectors. (Courtesy Joel Kindt.)

There are wires soldered onto the connectors and they are connected to the function generator via a relay, which is controlled by the trap triggering circuit. During the experiments, firstly, the presence of a cell at a certain location (where the light collecting spot is aligned to, usually the center of the trap) could be detected by the detection circuit that monitors the intensity of transmitted light; the circuit consists of a photodiode and a transimpedance amplifier (TIA) configuration that turns the photocurrent from the photodiode into an analog voltage signal. And secondly, the data acquisition unit (DAQ) reads this analog signal and feeds it to the LabVIEW program to compare with a preset threshold voltage. If the voltage is lower than the threshold, it indicates a cell's presence inside the trap area. Then the LabVIEW controls the DAQ to give a "1" digital output to trigger the relay and enable the AC signal applied on the DEP electrode automatically.

The releasing of the trapped cell is also controlled by the LabVIEW program. It was originally set to release the cell (by giving a digital “0” output to open the relay and thus turn off the DEP trap) after a certain amount of time set by the user [4]. In 2010 the senior design group worked on the project integrated the spectrum acquisition software that communicates with the Ocean Optics spectrometer into the LabVIEW program, and now the trapped cell is released after the spectral data acquisition is done [5].

5.2 Software control

At first the fluidic control, DEP trapping of the cell and data collection were carried out manually, to expedite this process, LabVIEW programs were written and integrated with the hardware, including a custom syringe pump, the circuit that realize the automatic detection of cell’s presence and cell trapping, and the spectrometer.

5.2.1 Custom syringe pump

The system required a relative constant flow rate. However, the low-throughput (as low as 1 μL/hr, corresponding to a flow rate of 40μm/sec) fluidic system raised challenges for a traditional syringe pump: the low flowrate in a microfluidic channel with small dimensions created a high pressure environment which in turn applied a large force on the small gear inside the syringe pump (NE-1000, New Era Pump Systems), and eventually damaged it. And the pressure built up in the system requires the use of syringes with luer lock adaptors and the ones available are at least 3ml, corresponding

to a diameter of 8.66 mm, so even the slowest speed setting on the syringe pump (1 µm/sec) would result in a flowrate higher than 200µm/sec.

So a custom syringe pump was built with Encoder Mike Controller (18011, Oriel Instruments), and its ON/OFF duty cycle is controlled by the LabVIEW program, as illustrated in Fig. 5.5. After the Mike controller is set to remote mode, the user can adjust the speed of the pump from as low as 0.5 µm/sec to 200 µm/sec, and the length of the ON/OFF time in ms; typically the duty cycle of the pump is set to 10%-30%.

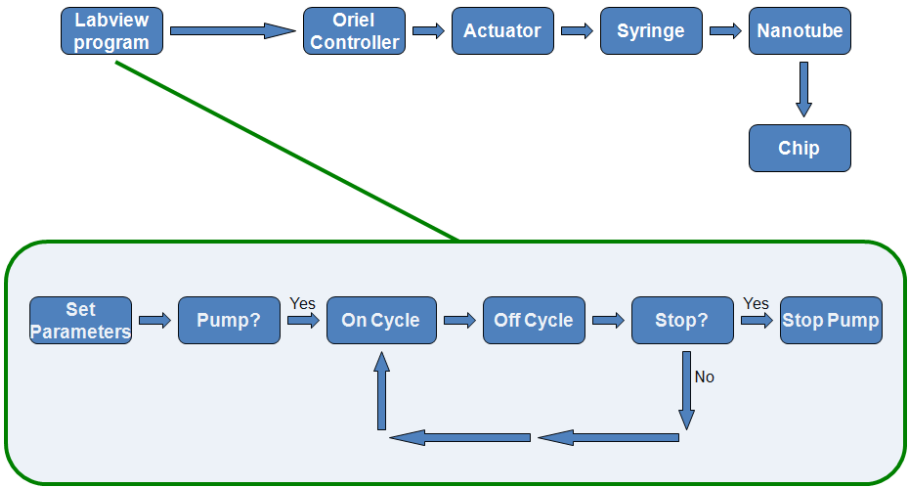

Fig. 5.5 Schematic diagram of flow control system (reproduced from spring 2008 senior design report [4]).

It usually takes approximately 20 minutes for the system to stabilize and achieve a steady flowrate. However, it has been observed that having the automated flow control

system running continuously for a few hours resulted in clogging in the channel, or seeing much fewer cells flowing through the channel, possibly caused by some filtration through the settled cells due to the low flowrate.

5.2.2 Triggering of trap with spectral data acquisition

Two approaches had been explored to realize the automated triggering of the traps, both of which relied on the same mechanism of detecting the decrease in the transmitted light intensity. The first one was the photodiode and TIA approach introduced in section 5.1.3, which was mainly constructed with hardware. The other one utilized the optical signal collected by the spectrometer, which also greatly involved with software control.

According to the spring 2008 senior design report [4], the prototype photodiode circuit had a major problem. When an RF signal with frequency over 9MHz was applied to the trapping electrode, the output from the TIA would suddenly drop below 0V, making it unusable for the computer's hardware interface. It was believed that some of the copper wires used in the prototype of the trapping circuit acted as antennas, producing noise that was then picked up possibly by the wires connecting to the photodiode circuit such as the power supplies or its output signal wire affected the offset voltage of the amplifiers used in the TIA.

This issue motivated an alternate method to detect the presence of a cell such as the continuous spectrum analysis discussed below. Since the real-time spectral data of the

cavity was already available, monitoring it would reflect the intensity of the transmitted light. So a side code was integrated with the main LabVIEW code [5] to monitor the maximum amplitude of the spectrum, and if it fell below a certain threshold, the DAQ would output a “1” and trigger the trapping electrodes. Even though the spectral data were collected with 6-8 seconds integration time, a 100ms integration time was used for the real time monitor of the transmitted light, and this was sufficient to work with a fluidic flow of 100-200 μm/sec.

References:

[1] H. Shao, D. Kumar, and K. L. Lear, “Single-cell detection using optofluidic intracavity spectroscopy,” *IEEE Sensors Journal*, vol. 6, no. 6, pp. 1543-1550, Dec, 2006.

[2] J. H. Kang, Y. C. Kim, and J. K. Park, “Analysis of pressure-driven air bubble elimination in a microfluidic device,” *Lab on a Chip*, vol. 8, no. 1, pp. 176-178, 2008.

[3] J. Kindt, L. Netherton and H, Cutler, senior design report, spring 2009.

[4] M. Bretz, A. Fierro, D. Sehrt, D. Trujillo and E. Vlcek, senior design report, spring 2008.

[5] W. Fuller, T. Kiljan, A. Miller, L. Mundhenke and M. Eldeiry, senior design report spring 2010.

CHAPTER 6 SPECTRAL RESULTS AND ANALYSIS

Experiments have been carried out to examine the dielectrophoresis (DEP) properties of the polystyrene spheres/particles and de-ionized (DI) water used as particle suspending medium, and to inspect the transmission spectra of a fluidic Fabry-Pérot (F-P) cavity loaded with different cancerous and non-cancerous cells from canine and human cell lines using phosphate buffered saline (PBS) as suspending medium. The spectral data was quantified by the strength of their transverse modes and analyzed with statistical methods such as Student's t-test.

6.1 Test on single particle dielectrophoresis (DEP) traps

Cell-patterning and cell-manipulation in micro-environments is fundamental to biological and biomedical applications, such as our technique of intracavity spectroscopy (OFIS) that proposes early detection of individual cancer cells based on their characteristic OFIS spectrum in a microfluidic resonant cavity.

Dielectrophoresis (DEP) trapping structures were designed and the electrical frequency dependence of the trapping strength of traditional Voldman trap [1] was tested. In the initial attempt to combine DEP trapping with OFIS, DEP traps displayed a good ability to place a single particle (polystyrene sphere of various sizes) in a desired location in a microfluidic channel, under a flow rate of 20-40 μm/s. In the former case of 20μm/s,

particles could be trapped using no more than 5VAC voltage, as well as released when wanted.

The capturing strength of DEP traps was measured based on the minimum AC voltage and frequency required to capture a single particle under certain flow rate. It was revealed that the capturing strength of a DEP trap varies according to the size and material of the particle. The structure of the Voldman trap used in this experiment is shown in Fig. 6.1 (a), the particle trapped in (b) was 10µm diameter polystyrene sphere and the suspending medium used was deionized (DI) water. Due to the chip bonding difficulty experienced at the time, a PDMS channel was used for this experiment. The cross-sectional view of the bonded chip is illustrated in Fig. 6.2.

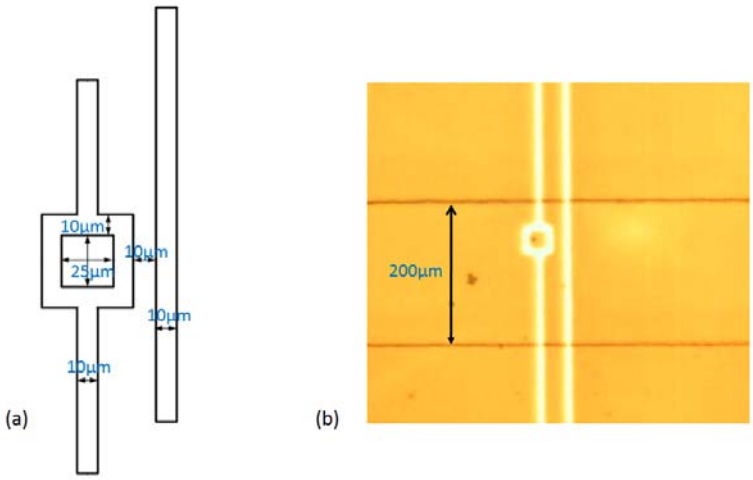

Fig. 6.1 (a) Dimensions of the Voldman trap used in the experiment to test the DEP capturing strength; (b) A microscopic picture of a trapped particle, with the horizontal lines showing the edges of the microfluidic channel.

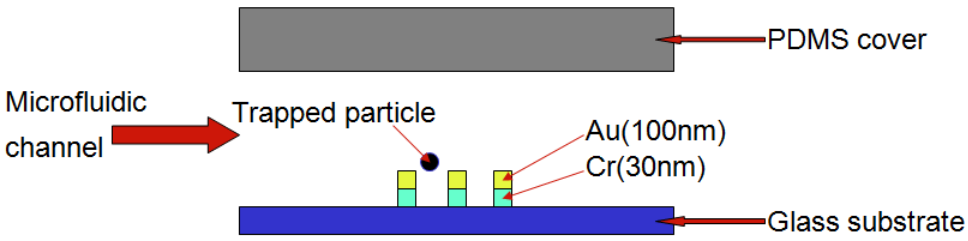

Fig. 6.2 The cross-sectional view of the chip used in the experiment to test the DEP capturing strength.

The particles would be captured by the DEP trap when the time-average DEP force [2], F_{DEP}, was larger than or at least equal to the drag force from fluidic flow,

$$F_{Fluid} \le F_{DEP} = 2\pi r^3 \varepsilon_m \,\mathrm{Re}[K(\omega)]\nabla E^2 \qquad (6.1)$$

where r is the radius of the particle, ε_m is the permittivity (dielectric constant) of the medium, $K(\omega)$ is the polarization factor, also known as the Clausius-Mossotti (CM) function that contains all the frequency dependence of the DEP force,

$$K = \frac{\varepsilon_p^* - \varepsilon_m^*}{\varepsilon_p^* + 2\varepsilon_m^*} \qquad (6.2)$$

and ε^* is the complex permittivity of the particle (ε_p^*) or the suspending medium (ε_m^*),

$$\varepsilon^* = \varepsilon - j\frac{\sigma}{\omega} \qquad (6.3)$$

The experiment was carried out with PDMS-glass chips, and the polystyrene spheres were diluted in DI water. The flowrate was stabilized to approximately 40 μm/s. The flowrate was estimated with the following method: the viewing area of the CCD camera was 1mm in length, and it took certain particle, which was travelling in the center 1/3 of the channel, approximately 25 seconds to go across the area along the channel. Then the minimal voltage-frequency pairs used to successfully immobilize the particles were recorded. Even though the exact frequency dependence of Re[$K(\omega)$] (the real part of $K(\omega)$]) was not available in the literature nor do we have any way to measure it directly, measuring the capturing strength could reveal its trend by

$$Re[K(\omega)] \propto \frac{F_{Fluid}}{\nabla E^2} \propto \frac{Capturing\ strength}{const \cdot V_{AC}^2 r^3} \tag{6.4}$$

Thus this trend could be illustrated by plotting the $1/V_{AC}^2$ (where V_{AC}^2 is the minimum AC voltage) and electrical frequency required to capture a single particle under a constant flow rate of 40 μm/s, as shown in Fig. 6.3.

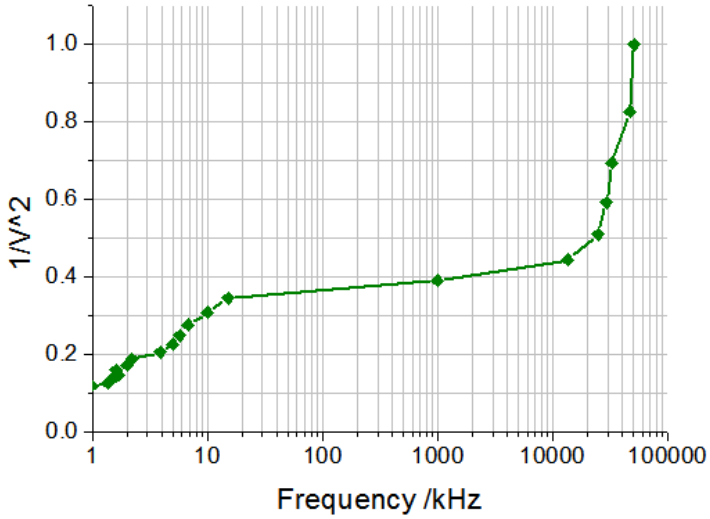

Fig. 6.3 The experimental trend of frequency dependence of Re[*K(ω)*].

Plots of the frequency dependence of Re[*K(ω)*] for different types of cells and suspending medium with various concentration of PBS (thus different electrical conductivities) could be found in the literature [2,3]. Even though we used polystyrene spheres instead of cells and water had a lower electrical conductivity of 0.05S/m, the combination of the complex permittivity of the particles and water followed a similar trend as the frequency dependence of cells and PBS, as shown in Fig. 6.4.

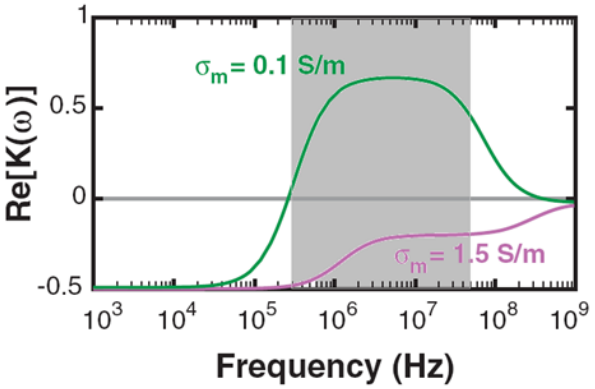

Fig. 6.4 Plot of real part of the CM factor of mammalian cells at low (0.1 S/m) and high (1.5 S/m) solution conductivities (reproduced from [2]), with the grey area indicating the range of electrical frequency used in our experiments.

And from equation (6.4) one can find out that the frequency dependence of Re[$K(\omega)$]should depend on the particle size as well. The experiment results were summarized in Fig. 6.5. All four curves for 5, 7, 10 and 15μm particles followed similar prediction, and all trends except for the one for 15μm particles qualitatively matched equation (6.4).

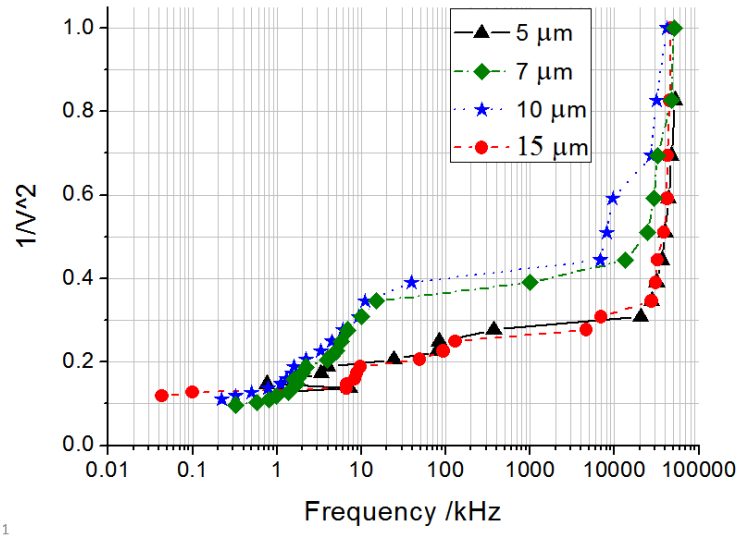

Fig. 6.5 The experimental trend of frequency dependence of Re[$K(\omega)$] with various diameter of particles trapped.

This experimentally confirmed that DEP traps can be combined with OFIS, and it was the only time in this study that the capture strength of DEP traps was systematically measured and the only time its frequency dependence was compared with theoretical prediction.

6.2 Differentiation of canine HSA and PBMC

Canine cancer cells were chosen to acquire preliminary data with OFIS system for they had several benefiting characteristics. The dog is an excellent translational model for the investigation of novel antineoplastic therapies. Unlike murine (mouse) models, dogs are relatively outbred, immunocompetent animals with spontaneously occurring tumors,

representing a spectrum of tumor histotypes that have biology similar to that found in humans. The relatively large size of canine tumors, when compared with murine tumors, may more closely approximate human solid tumors with respect to important biological factors such as hypoxia and clonal variation, and allows for multiple samplings of tumor tissue over time [4,5].

The two main types of cancer cells used in this research, hemangiosarcoma (HSA) and lymphoma, are two of the most common canine cancers. Although very uncommon in humans, HSA is the most common splenic tumor of dogs. It is typified by rapid and widespread metastasis and a very poor [6], for hardly any symptoms exhibit until an advanced stage when biopsy is available for clinical detection of canine HSA, but treatment is usually unsuccessful at this stage. Currently there are no efficacious screening tools to facilitate early detection of HSA, thus novel techniques for its early detection would be of considerable clinical utility. Other research [7] has shown promising results for the early detection of HSA, with the help of flow cytometry and several fluorescent labels. Due to the high cost and the very limited availability of the equipment to the veterinary hospitals, it is unlikely that such a test can be generally applied to common dog patients.

Optical properties of one HSA cell line, DEN-HSA, were investigated with OFIS technique. The DEN-HSA canine hemangiosarcoma cells were established in the laboratory of Dr. Thamm [8]. Dr. Thamm provided the following recipe for HSA cell culture and preparation: and the DEN-HSA cell line was cultured in Minimal Essential Medium (MEM,

BioWhittaker, Walkersville, MD) supplemented with 10% heat inactivated fetal bovine serum (HyClone, Logan, UT), 100 units/ml penicillin–streptomycin (Mediatech, Herndon, VA), 2 mM L-Glutamine (Mediatech), 1 mM sodium pyruvate (Mediatech) and 1X nonessential amino acid solution (Sigma, St. Louis, MO)(C/10%), at 37°C, 5% CO_2 in a humidified atmosphere, and suspended in C/10% on ice prior to utilization in the described experiments. The PBS used for cell suspension, channel preparation or flush, as well as further dilution, if necessary, was 1X PBS (i.e., 10mM PBS). The HSA cells had an enlarged and condensed nucleus, which was very apparent when the cells were cytospun and stained, as shown in Fig. 6.6(a).

The baseline non-cancerous cells used for comparison were peripheral blood mononuclear cells (PBMCs). These cells are often extracted from whole blood using ficoll, a hydrophilic polysaccharide that separates layers of blood, with monocytes and lymphocytes forming a buffy coat under a layer of plasma [9]. A sample of this resulting solution was then put on a slide, cytospin and stained to allow one to observe the morphology of the cells: the cells' nucleus would appear dark pink-red color while the cells' cytoplasm appeared to be light pink. The PBMC solution used were acquired from dog patients in the animal cancer center of CSU and it contained mainly the PBMCs, very small percentage of neutrophils and other polymorphonuclear (PMN) cells (totaling <1% of the population), as well as red blood cells, white blood cells, and platelets, based on the observation of the cytospin slides of stained PBMC samples. Fig. 6.6 showed the microscopic images of cytospin HSA cell and PBMCs. It was believed that the larger cells (on which OFIS spectra were acquired, unless otherwise specified) in the PBMC solution

were monocytes, the one with horseshoe-shaped nucleus shown in Fig. 6.6 (b); and the smaller ones were lymphocytes, the one with small, round nucleus as shown in Fig. 6.6 (c). The red blood cells, white blood cells, and platelets, since they didn't have any nucleus, were in pale pink to colorless in the microscopic pictures of cytospin slides.

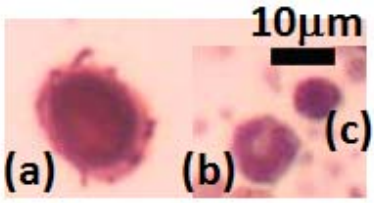

Fig. 6.6. Microscopic images of stained (a) HSA cell, (b) monocyte and (c) lymphocyte on cytospin slides, under 40x magnification.

Transmission spectra of cancerous HSA cells and non-cancerous PBMCs were collected with OFIS chips with different cavity depths. Cavity depths are determined from the free spectral range (FSR) of the transmission spectrum collected from fluid-filled cavities. Three separate chips with cavity depths of 16, 22, and 25 µm were used to measure transmission spectrum of HSA cells; and the 16 and 25 µm channel were then used to take transmission spectrum of baseline PBMCs.

In order to have the cell spectra collected from different locations of the same chip (where the cavity lengths varied and cause the exact wavelength of the bare cavity peak to shift) or even from different days (when the Led intensity fluctuated) to be directly

comparable, normalization was applied to the cell spectra to remove the spectral dependence of the infrared LED, using the following steps. Detailed instructions and the fitting calculation algorithm is provided in Appendix C. **(1)** Load the bare cavity spectrum that was taken at a location right next to the cell, or the exact cell location after it was removed, record the wavelength and intensity of the 4 adjacent peaks located in the center of the spectrum near 900nm: (λ_1, I_1), (λ_2, I_2), (λ_3, I_3) and (λ_4, I_4). **(2)** Use a Lorentzian shape with skew factor (since the LED envelop was not symmetric)

$$I(\lambda) = I_{max} \frac{a^2}{a^2+(\lambda-\bar{\lambda})^2+a^2(\lambda-\bar{\lambda})\cdot s} \quad (6.5)$$

to fit the 4 points, where *Imax, a,* $\bar{\lambda}$ is the height, width and center of the Lorentzian shape and and *s* is the skew factor; this could be done with Excel solver add-in by finding the minimum of the sum of the difference between the Lorentzian shape and the 4 points

$$Sum = I(\lambda_1) + I(\lambda_2) + I(\lambda_3) + I(\lambda_4) - (I_1 + I_2 + I_3 + I_4). \quad (6.6)$$

(3) The normalized spectral transmission would be the quotient of the raw spectrum and the resulting Lorentzian shape that had the minimal sum of difference.

Transmission spectra of 24 single cells from canine HSA-DEN cell line and 24 baseline non-cancerous PBMCs were collected and analyzed. Since the cells were settled on the bottom of the channel rather than rotating, each cell's spectra was relatively constant.

Example normalized transmission spectra of HSA cells and PBMCs in a 25 μm deep cavity are plotted in Fig. 6.7, where vertical lines on each spectrum marked the peaks of bare cavity mode taken at the same location for each cell, or right next to it. The exact wavelength of the bare cavity modes acquired in conjunction with cells at different positions along the channel shifted due to changes as small as 0.2% in the cavity length.

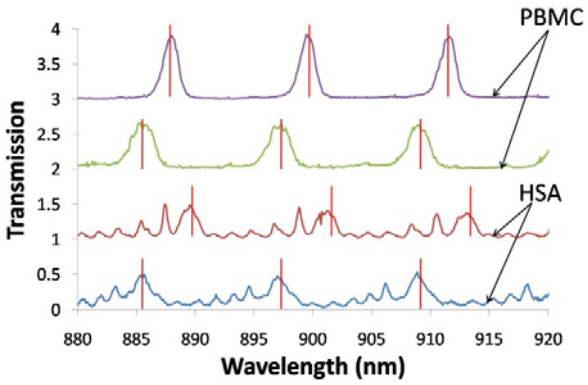

Fig.6.7. Normalized transmission spectra of PBMCs and HSA cells; the vertical lines indicate the bare cavity modes at the same location, or adjacent to each cell.

PBMCs and HSA cells showed distinctive spectral characteristics: the spectra of the normal PBMCs, more precisely monocytes, due to the manual selection of bigger cells in the solution, were dominated by peaks near the bare cavity mode positions with only very weak intervening modes while the majority of HSA cells exhibited several well-defined, significant transverse modes with moderately uniform spacing and weakened peaks as the frequency increased within each FSR.

Some other spectral pattern of HSA spectra were summarized in Fig 6.8. Even though they didn't demonstrate distinctive multiple transverse modes with good aspect ratio, it was still obvious that their transverse modes were stronger than that of the PBMCs', and one could tell them apart solely based on their transmission spectra.

Even though later after the adjustments in the optical system, more (up to two) transverse modes were excited for monocytes that were manually selected based on the cell size, comparing the normalized spectra can still differentiate these two types of cells: the HSA spectra had more average intensity in the transverse modes; and their maximum peak intensity was around 0.5 (compare with monocytes' 0.9), due to their enlarged and more condensed nucleus, as shown in Fig. 6.9.

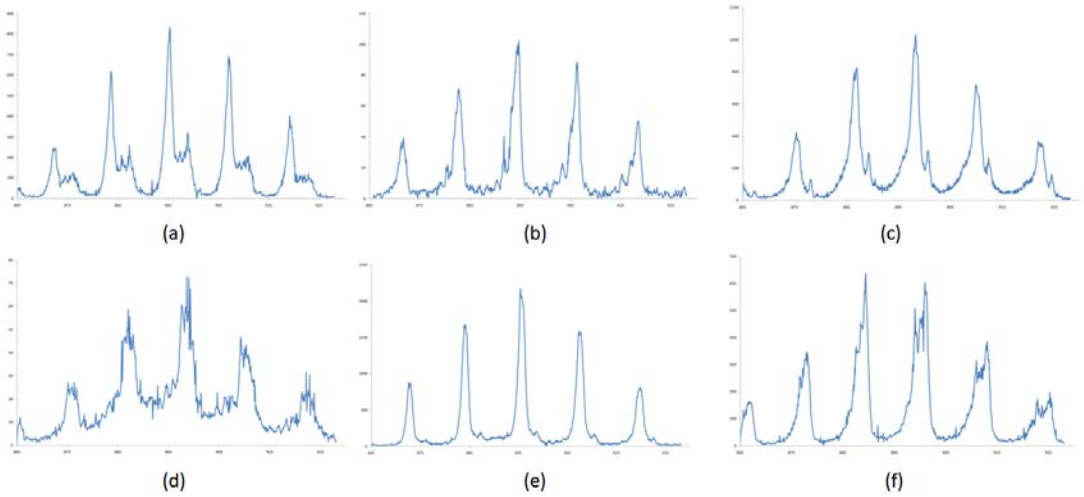

Fig. 6.8 Examples of untypical HSA spectra (raw).

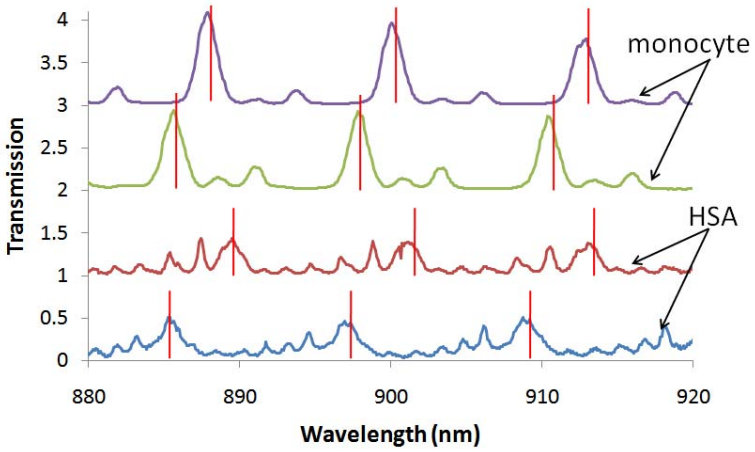

Fig.6.9. Normalized transmission spectra of monocytes (after optical adjustments and manual selection of cells) and HSA cells; the vertical lines indicate the bare cavity modes at the same location, or adjacent to each cell.

Although the HSA spectra were acquired from two different cavities, it was believed that the absolute cavity length is not a critical parameter of intracavity spectroscopy. In both 25 µm and 22 µm cavities, monocytes and HSA cells showed distinctively different spectral characteristics. The spectra of the non-neoplastic monocytes were dominated by 1-2 peaks near the bare cavity mode positions with only very weak intervening modes and the maximum peak intensity in the normalized spectra was over 0.9. In contrast, the majority of HSA cells exhibited several well-defined, significant transverse modes of moderately uniform spacing and weakened peaks near the bare cavity mode wavelengths, and the maximum peak intensity in the normalized spectra was approximately 0.5. Transverse mode groups were repeated for each longitudinal mode

and were spaced by the cavity's FSR of approximately 12 nm or 14 nm, corresponding to a cavity length of 25 μm and 22 μm, respectively.

6.3 Differentiation of lymphoma and lymphocytes

Canine lymphoma histologically resembles human intermediate- to high-grade non-Hodgkin's lymphoma [10], and is typified by very similar biologic behavior and response to therapy. Optical properties of two lymphoma cell lines, 1771 and OSW were investigated with the OFIS technique. The OSW canine T-cell lymphoma cells were provided by Dr. W. Kisseberth, Ohio State University [11]. The 1771 canine B-cell lymphoma cell line was provided by Dr. K.A. Jeglum, Wistar Institute [12, 13, 14]. Both cell lines are maintained at CSU Department of Animal Science.

The distinctive spectral properties of canine lymphoma and lymphocytes were previously reported in [15]. Lymphocytes were used as a control for the two lymphoma cell lines that were investigated, OSW and 1771. Fig.6.10 shows typical lymphoma and lymphocyte spectra from a 15.8 μm deep cavity used in that study, and the vertical lines on each spectrum marked the peaks of bare cavity modes as noted above.

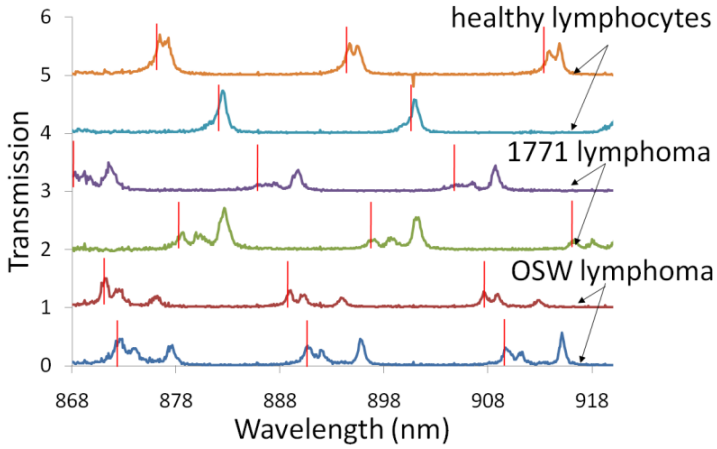

Fig.6.10 Normalized transmission spectra of healthy canine lymphocytes and neoplastic lymphoma cells from two different cell lines, 1771 and OSW. Vertical lines indicate the bare cavity mode wavelengths adjacent to each cell. (Reproduced from data acquired by Hua Shao.)

Lymphoma cells from both cell lines exhibited multi-mode behavior with at least two clear transmission peaks in each free spectral range. The primary peak, attributed to the fundamental mode, was well separated from the bare cavity resonance obtained at the test locations adjacent to each cell. The measured fundamental mode wavelength shifts were extremely repeatable for different lymphoma cells from the same cell line with a standard deviation of ±0.13 nm. The lymphocyte control spectra had a fundamental mode as well, but no higher order transverse modes were observed for these non-neoplastic cells.

And the control cell chosen was still PBMC, even though at that time the samples were acquired from a different dog patient. In these PBMC samples, monocytes, lymphocytes, and a small fraction of neutrophil granulocytes were found in the PBMC samples with different percentages. Monocytes were manually selected during collection of OFIS transmission spectra of unstained PMBC based on obvious size differences between the monocytes (approximately 14-17 μm), lymphocytes (7-8 μm) [16]. Even though neutrophil granulocytes have similar sizes (10-12 μm) as monocytes, since they only took a very small percentage of the cell population (less than 1%), it was assumed that they can be neglected.

The spectra of monocytes in Fig. 6.9 showed more transverse modes than the ones of lymphocytes in Fig. 6.10, this was due to the manual selection of larger cells, for even after the optical adjustments, the spectra the smaller PBMCs were observed to be less likely to contain any observable peaks away from the bare cavity modes, and it was not possible to identify whether they were lymphocytes or neutrophil, although the latter ones were only <1% of the population. One could still tell the monocytes and lymphoma apart even though they all have two transverse mode peaks, by their frequency spacing. An important parameter of the cell spectra was going to be introduced in Chapter 7, which is the ratio of transverse- to longitudinal- mode spacing, $\Delta\nu_{trans}/\Delta\nu_{long}$, where $\Delta\nu_{trans}$ was the frequency spacing between the two transverse mode peaks and $\Delta\nu_{long}$ was the FSR. For lymphoma cells, this ratio was 0.17±0.01, and for monocytes it was 0.22±0.02.

Although qualitative observations of the OFIS spectra can readily distinguish individual HSA cells and PBMCs, as well as lymphoma and lymphocytes or monocytes, a new transmission parameters method was applied to quantitatively analyze the spectra and facilitate future automated sorting algorithms. The method would be discussed in detail in Section 6.5.

6.4 Preliminary spectral results on human pancreatic cancer cells and ovarian cancer cells

In addition to canine HSA and lymphoma cells, the OFIS spectra of some human cancer cells were also investigated. These preliminary results were not published, and more control experiments need to be done to develop a more complete understanding of their OFIS spectra.

Pancreatic cancer is a malignant neoplasm of the pancreas, it has been called a "silent killer" because early pancreatic cancer often does not cause symptoms; By the end of 2010 in the United States, it is estimated about 43,140 individuals will be diagnosed with this condition, and 36,800 will die from the disease [17]. The prognosis is poor, with fewer than 5% of those diagnosed still alive five years after diagnosis [18]. The two human pancreatic tumor cell lines, SW1990 and PANC1, were provided by Dr. Colin Weekes at University of Colorado Denver, and some example cell spectra from each cell line were shown in Fig. 6. 11, with the bare cavity spectra associated with each cell showing in the same plot.

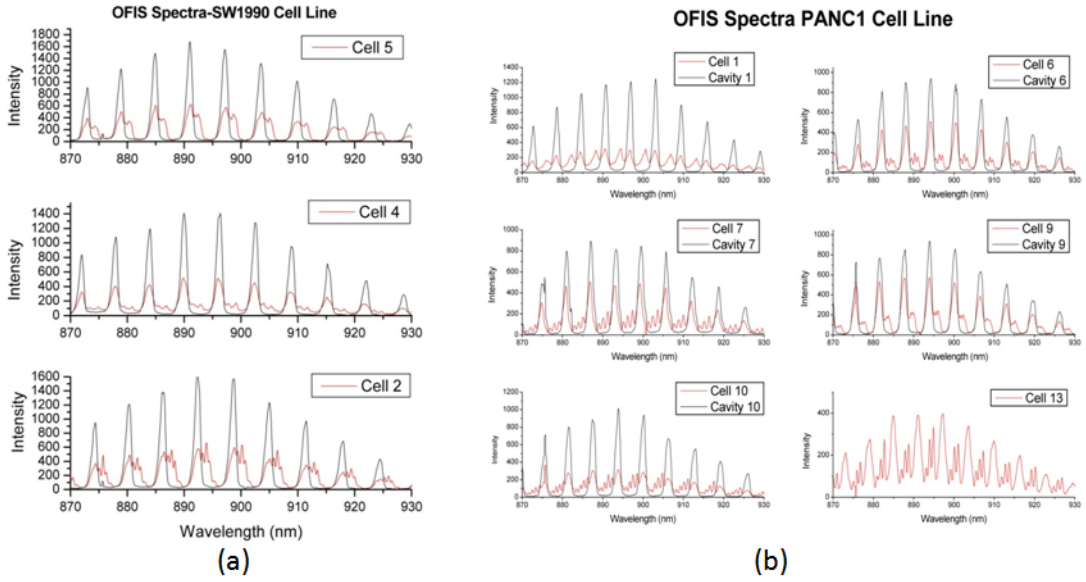

Fig.6.11 Raw transmission spectra of pancreatic cancer cells from two cell lines, (a) SW1990 and (b) PANC1, with the bare cavity spectra taken at the same location (or adjacent to each cell), if available, showing on the same plot. (These figures were created by Dr. Dave Kisker.)

While the pancreatic cancer cells from both cell lines showed strong, multiple transverse modes, there was no obvious repeatable mode pattern observed in these OFIS spectra. No control experiments were done to find out OFIS's ability to differentiate human pancreatic cancer cells from baseline non-cancerous cells. Unlike cancer cells, non-cancerous cells are very hard to culture due to apoptosis (programmed cell death); and getting human PBMCs (which would be extracted from human blood) is involved with strict statute and regulations.

Ovarian cancer is the fifth leading cause of death from cancer in women and the leading cause of death from gynecological cancer [19]. Ovarian cancer starts in the ovaries and symptoms are often vague. Most (>90%) ovarian cancers are classified as "epithelial" and were believed to arise from the surface (epithelium) of the ovary [20]. The human ovarian cancer cells and the normal ovarian cells used in the experiments were provided by Dr. Kian Behbakht at University of Colorado Denver. Three ovarian tumor cell lines were examined, A2780 (fast growing, rapidly tumorigenic), SKOv3 (intermediate invasiveness) and CAOv3 (slow growing, weakly tumorigenic); and two ovarian cell lines were investigated as baseline control, NOSE006 and NOSE007, which are normal ovarian surface epithelial (NOSE) cells. Example cell spectra from each cell line were shown in Fig. 6. 12 and Fig. 6.13, with the bare cavity spectra associated with each cell showing in the same plot.

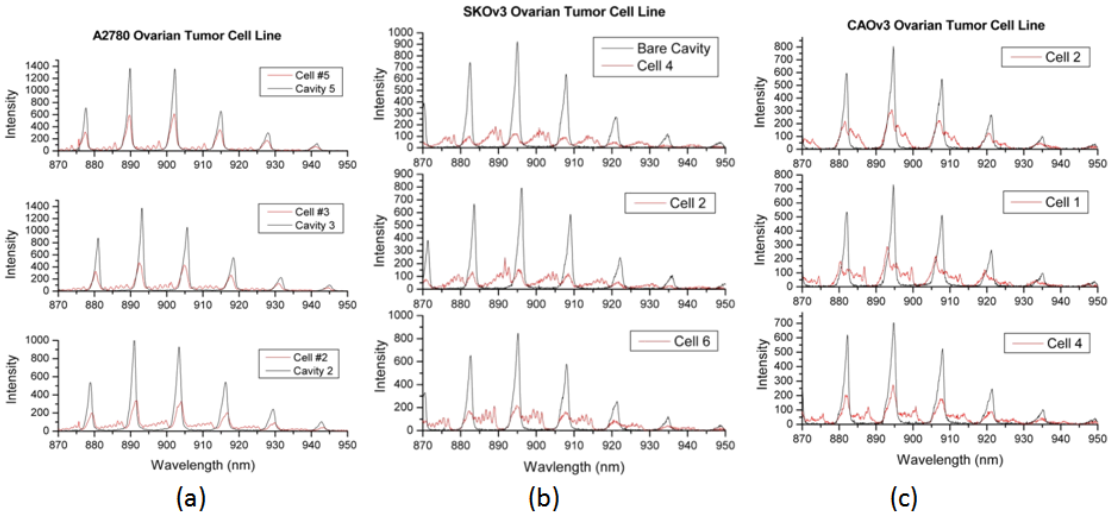

Fig.6.12 Raw transmission spectra of ovarian tumor cells from three cell lines, (a) A2780, (b) SKOv31 and (c) CAOv3, with the bare cavity spectra taken at the same location (or adjacent to each cell), if available, showing on the same plot. (These figures were created by Dr. Dave Kisker.)

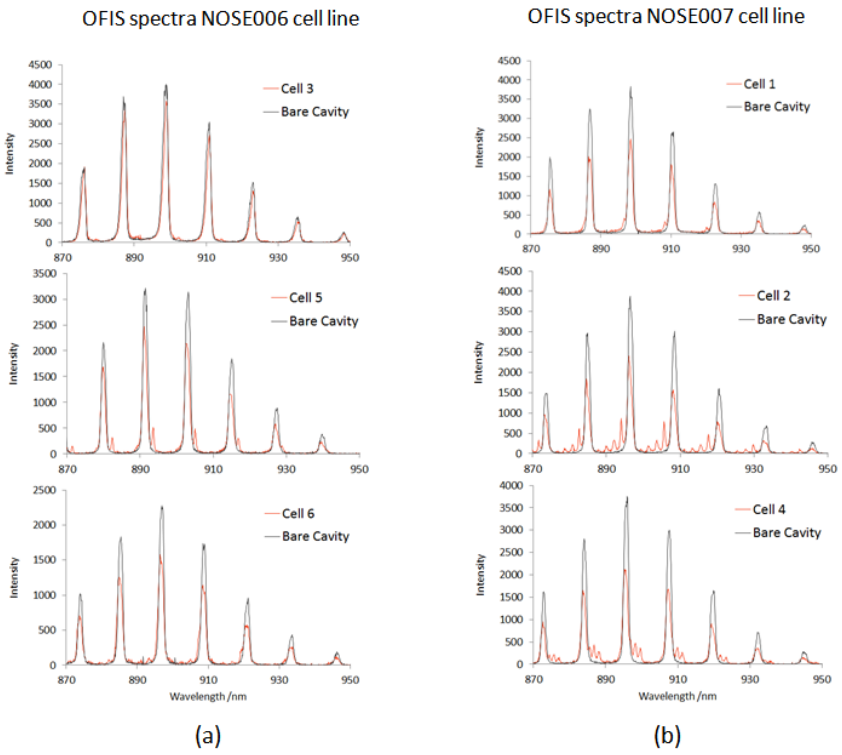

Fig.6.13 Raw transmission spectra of baseline ovarian cells from two cell lines, (a) NOSE006 and (b) NOSE007, with the bare cavity spectra taken at the same location (or adjacent to each cell), if available, showing on the same plot. (These figures were created by Dr. Dave Kisker.)

After comparing the OFIS spectra of the three ovarian tumor cell lines, it was found that the cancerous cell lines demonstrated strong, multiple transverse modes even though the correlation between the cells' invasiveness and their OFIS spectra was not very clear. And some of the baseline NOSE cells had very weak or none transverse modes while others showed strong transverse modes, very similar to the ones of ovarian cancer cells.

Based on these preliminary results, it was not conclusive that OFIS could differentiate human ovarian tumor cells from normal ovarian surface epithelial, which was more likely to be chosen as the baseline control cells than human PBMC would, for the NOSE cell would exist in the same environment as the ovarian cancer cells. Similar problem was found when the OFIS spectra were collected on endothelial cells, which would be the baseline control for canine HSA. One future work would be collecting more OFIS spectra from each cell line (the tumor ones and baseline control of endothelial or epithelial cells) to confirm the percentage of the cells that demonstrate multiple and repeatable transverse modes, and propose a sorting algorithm based on their spectra features.

6.5 Transmission parameter method

While the quantitative differentiation of canine lymphoma and lymphocytes with OFIS was successfully demonstrated and analyzed in terms of longitudinal mode shift and lateral confinement induced by the cells in [15], further experiments revealed that the mode shift method were not sufficiently repeatable to distinguish a more aggressive canine cancer cell line, HSA, from a background of PBMCs. Accordingly, an alternative analysis of OFIS spectra based on a single parameter quantification of the strength of transverse modes were explored and proven to be an efficient sorting algorithm for the classification for HSA cells and PBMCs.

Qualitative observation of the HSA spectra in Fig. 6.9 and the lymphoma spectra in Fig. 6.10 indicated that these cancer cell lines produced much stronger transverse mode peaks between the bare cavity modes than the corresponding monocyte and/or lymphocyte controls. Even in the absence of a precise physical model, the differences motivate an effort to quantify the strength of transverse modes away from the bare cavity peaks and seek a correlation of the transverse mode strength parameters with a binary categorization of cells as neoplastic or non-neoplastic.

Two quantitative measures of the strength of transverse modes were analyzed. One is the mean value of transmission, T, and the other is the standard deviation of the transmission, σT. Casual observation suggested that the presence of multiple transverse modes was correlated with neoplastic cells. To quantify the extent of multimode spectra, it was noted that well-defined transverse mode peaks that have significant peak transmission height would produce a larger mean value of transmission and generally a larger fringe modulation depth. However, if the individual transverse modes for HSA were not well resolved due to the increase of background noise, the mean transmission would increase, but the standard deviation value would be diminished. Also, neoplastic cells that produced low intensity transmission peaks with large fringe depth were sometimes observed where, although the resulting mean transmission was low, the standard deviation value was comparable with that of other neoplastic cells. Hence, both the mean transmission and standard deviation of the transmission were considered.

The two parameters, T and σT, of the normalized transmission spectra (using the raw spectrum normalization method described in Section 6.2) of all 16 HSA cells and 16 monocytes in the 25μm deep channel, and all 8 HSA and 8 monocytes in the 22μm deep channel were computed and plotted in Fig. 6.14. During the spectrum normalization, the peaks in the 880 to 920 nm range of a bare cavity spectrum collected from a location next to each cell was fit to a Lorentzian line shape by adjusting the fit's peak wavelength, peak height, peak width and a small skew factor if necessary, i.e. by adjusting $\overline{\lambda}$, *Imax, a and s* in equation (6.5), respectively. The intensity of the Lorentzian curve was then taken to represent unity transmission for the corresponding cell spectrum to allow normalization of spectral regions between the bare cavity peaks. The transmission parameters and the statistical significance of the results were nearly independent of the exact parameters of the unity transmission fit and even the functional form of the fit. To prevent the bare cavity modes from influencing the parameters, the calculations were performed only on data at least one full-width-at-half-maximum (FWHM) away from the adjacent bare cavity mode peaks. Detail calculation of the transmission parameters is also included in Appendix C.

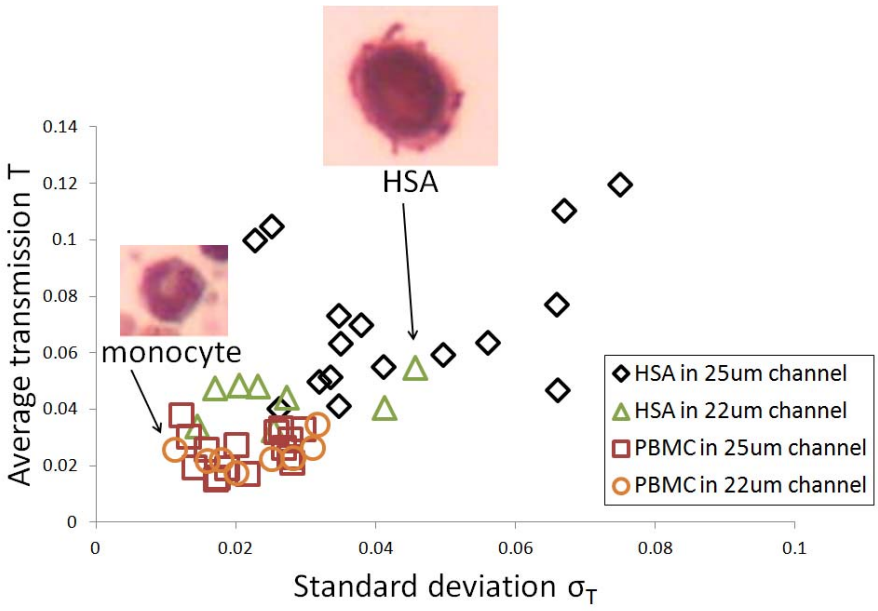

Fig.6.14 Scatter plot of transmission results of HSA and PBMC in 25μm and 22μm deep channels.

In the scatter plot, the neoplastic and non-neoplastic cells in both channels were divided into two groups. In comparison to the monocyte spectra, HSA cell spectra had a higher mean transmission value, and were more likely to have a greater transmission standard deviation, indicating HSA had stronger transverse modes that may be attributed to the enlarged nucleus of neoplastic cells, or more likely (as later found out), to the flattened cell surface. This will be further discussed in Chapter 7. Large standard deviation of transmission values indicated large differences between transmission peaks and valleys, i.e. greater contrast, but did not indicate a lack of repeatability in individual cell spectra.

To support the generality of this method, it was also applied to previously reported lymphoma and lymphocyte results acquired in a 15.8μm deep channel with the OFIS technique. Although the number of cells being interrogated was more limited, the neoplastic lymphoma and non-neoplastic lymphocyte were divided into two groups as well, as shown in Fig. 6.15.

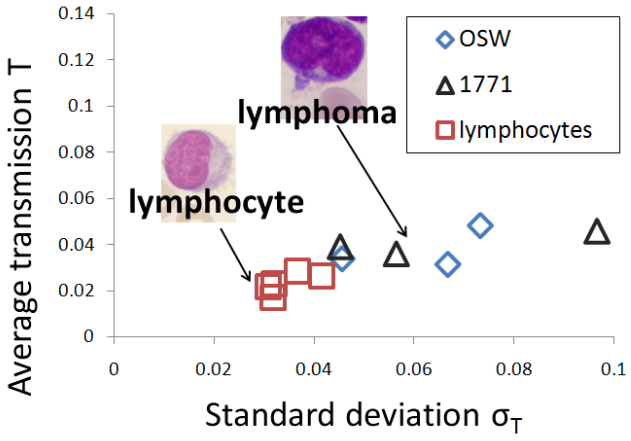

Fig.6.15. Scatter plot of transmission results of lymphoma and lymphocyte; inset reproduced with permission from Lymphomas Extensive Image Collection © 2009 Rector and Visitors of the University of Virginia, Charles E. Hess, M.D. and Lindsey Krstic, B.A.

Not only the data analysis indicated that we could rely on this new method of parameterizing transverse mode strength to distinguish cancerous cells, statistical analysis in the next section showed that the new method to parameterize HSA and

monocyte transverse mode spectra can properly categorize the cells with good sensitivity and specificity.

6.6 Statistical analysis

Two kinds of statistical analysis were applied to the HSA and PBMC differentiation using transmission parameter method. A statistical hypothesis test, Student's t-test [21] was applied to evaluate the difference in transmission parameters of neoplastic and non-neoplastic cells. To assess potential clinical significance, the sensitivity and specificity for detecting neoplastic cells was further evaluated by constructing a receiver operating characteristic (ROC) curve [22].

Typical ROC curves are generated by varying the classification threshold with respect to a single parameter. In order to form a single parameter for classification, a weighted sum of the mean and standard deviation of the transmission $W_T=T+k\sigma T$ was used, where k is a constant chosen to roughly optimize statistical significance of the data sets. The distinctiveness of the cell populations varied weakly but smoothly with k. This single combined transmission parameter enabled quantitative analysis of the transmission spectrum of any individual cell, and a two sample Student's t-test was carried out to verify the statistical importance of neoplastic and non-neoplastic cell classification.

The assumptions of two sample Student's t-test include:

- $X_1, X_2, \ldots X_m$ is a random sample from a population with mean μ_1 and variance

σ_1^2;

- Y1, Y2, …Yn is a random sample from a population with mean μ_2 and variance σ_2^2;

- The X and Y samples are independent of one another; both populations are normal distribution.

But in practice:

- The population mean: μ_1 and μ_2 is unknown;

- the population standard deviation: σ_1 and σ_2 is unknown;

- Sample size (numbers of sample) is small;

- One has to use the sample mean ($\overline{X}$and $\overline{Y}$) and sample standard deviation (s_1 and s_2), to estimate the population distribution.

The null hypothesis here is to assume that the mean of the two populations being sampled is the same (μ_1 - μ_2 = 0), and calculate the resulting standardized variable (also known as t-score). Then one can use the t-score to estimate the probability of the null hypothesis being true. The standardized variable between the two samples (the HSA and monocyte transmission collected from the 25μm deep channel with *k*=0.5) was

$$t = \frac{\overline{X} - \overline{Y} - (\mu_1 - \mu_2)}{\sqrt{\frac{s_1^2}{m} + \frac{s_2^2}{n}}} = 7.45 \qquad (6.7)$$

Where X_1, X_2, …X_{16} are HSA samples, and Y_1, Y_2, …Y_4 are PBMC samples; $m = n = 16$ and the original T and σT data listed in Table. I below:

Table I. Summary of mean (T) and standard deviation (σT) of the HSA and monocyte transmission collected from the 25μm deep channel

HSA cells	**HSA1**	**HSA2**	**HSA3**	**HSA4**	**HSA5**	**HSA6**	**HSA7**	**HSA8**
Mean (T)	0.105	0.073	0.040	0.055	0.100	0.064	0.063	0.070
stdev (σT)	0.025	0.035	0.026	0.041	0.023	0.056	0.035	0.038
	HSA9	**HSA10**	**HSA11**	**HSA12**	**HSA13**	**HSA14**	**HSA15**	**HSA16**
Mean (T)	0.110	0.119	0.041	0.050	0.051	0.047	0.077	0.059
stdev (σT)	0.067	0.075	0.035	0.032	0.034	0.066	0.066	0.050
PBMCs	**PBMC1**	**PBMC2**	**PBMC3**	**PBMC4**	**PBMC5**	**PBMC6**	**PBMC7**	**PBMC8**
Mean (T)	0.030	0.019	0.027	0.038	0.015	0.016	0.021	0.017
stdev (σT)	0.013	0.014	0.020	0.012	0.017	0.017	0.028	0.022
	PBMC9	**PBMC10**	**PBMC11**	**PBMC12**	**PBMC13**	**PBMC14**	**PBMC15**	**PBMC16**

Mean (T)	0.029	0.026	0.033	0.026	0.033	0.032	0.023	0.019
stdev (σT)	0.028	0.027	0.027	0.016	0.030	0.026	0.028	0.019

A normal distribution is governed by two parameters, the mean and the standard deviation. With the limited numbers of samples, the sample distribution no longer has a standard normal distribution, and it is governed by only one parameter called number of degrees of freedom,

$$\nu = \frac{(\frac{s_1^2}{m} + \frac{s_2^2}{n})^2}{\frac{(s_1^2/m)^2}{m-1} + \frac{(s_2^2/n)^2}{n-1}} = 17 \qquad (6.8)$$

With the t-score and *v* calculated above, a *p*-value can be computed, which represents the probability that the null hypothesis cannot be rejected. A Microsoft Excel built-in function TDIST (*t, v*, number of tailed test) can be used to calculate the accumulated probability. The "number of tailed test" is 1, if the problem we care is whether one sample is greater than the other; while the "number of tailed test" is 2, if the problem we care is whether one sample is different (smaller or greater) from the other. For the two samples mentioned about, the resulting p-value was 1.0×10^{-6}. Similar calculation for the cell transmission collected from the 22 μm deep channel revealed that the t-score was 4.63, and the number of degrees of freedom from the total of 16 samples was 12, resulting in a p-value of 5.8×10^{-4}. The very small p-values show that the classification of

HSA and monocyte had extremely high statistical significance; generally speaking, if p-value is smaller than 0.05, the two sample test result is considered to be statistically significant.

To further validate the general applicability of using the weighted sum of transmission parameters, W_T, to differentiate neoplastic and healthy cells, it was applied to the previously reported lymphoma and lymphocyte transmission spectra [15]. The resulting t-score between the two cell types was 4.59 and the number of degrees of freedom from the total of 11 samples was 6. The small sample size produced a somewhat higher, but still quite small null hypothesis probability of p = 3.8×10-3. In comparison, the peak shifts for lymphoma and lymphocytes were extraordinarily well separated. The peak shift mean values and standard deviations reported in Reference 7 of 20.38 ± 0.30 nm for 10 lymphocytes and 24.59 ± 0.13 nm for 10 OSW lymphoma cells yielded a t-score of 40.7. While these data indicate that a weighted transmission parameter was not the optimum approach for distinguishing lymphoma and lymphocytes based on the prior data, the p-values of < 0.005 for HSA in two different cavity lengths as well as lymphoma suggested the new approach may be broadly applicable for detecting multiple types of cancer cells. The calculation sheet for p-value is provided in Appendix D.

For a preliminary assessment of clinical utility, a ROC curve was generated for HSA cells and monocytes in the 25μm deep channel. Due to the limited number of samples, t-distributions were fit to W_T values for the two cell types. Note that t-distributions have larger tails than normal distributions, making the use of t-statistics more conservative

and leading to slightly lower sensitivity and specificity predictions than normal statistics would. The basic concept of ROC curve includes:

- ROC curve is a graphical plot of sensitivity vs. (1-specificity) for a classifier system as its discrimination threshold varies.

- True positive (TP, also known as “hit”): patient has certain disease, and the diagnostic result is positive;

- True negative(TN, also known as “correct rejection”): patient doesn’t have certain disease, and the diagnostic result is negative;

- False positive (FP, also known as “false alarm”): patient doesn’t have certain disease, but the diagnostic result is positive;

- False negative (FN, also known as “miss”): patient has certain disease, but the diagnostic result is negative.

- Sensitivity =TP/(TP+FN); and specificity=TN/(TN+FP).

- The area under the ROC curve (AUC) is an important parameter, representing how good the classification the system gives.

The sample mean ± sample standard deviation for HSA was W_T = 0.092±0.029, while the monocyte distribution produced W_T = 0.036±0.008. Numerical integration of the t-

distributions as the classification threshold was varied produced the most probable ROC curve as shown by the solid line in Fig. 6.16 [23]. Upper and lower 95% confidence limits on the ROC curve, shown with dashed lines, were computed by shifting the t-distribution mean values for HSA and PBMCs in opposite directions by 2.14 times the standard deviations of the sample means. Moving the mean values toward each other gave a lower 95% confidence limit on the ROC curve while shifting them farther apart generated the upper 95% confidence limit on the curve. The small sample size necessitated the use of t-distributions to construct a reasonable ROC curve as the 25μm deep channel provided perfect separation of the HSA and PBMC samples with a classification threshold W_T =0.1. While t-distributions are more conservative than normal distributions, deviations of the transmission parameters of biological cells from either distribution are possible, particularly in the tails. Such deviations would alter the exact locus of the ROC curve [24].

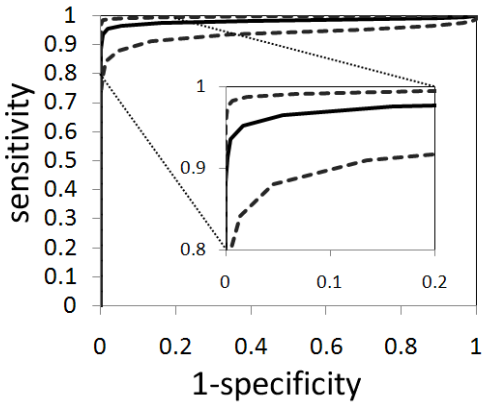

Fig.6.16 ROC curve of HSA detection against PBMCs, with inset enlarging the top left corner of the ROC curve.

The most probable ROC curve indicated that a diagnostic or screening test for individual HSA cells based on OFIS transmission parameters could simultaneously offer 95% sensitivity and 98% specificity. To quantitatively estimate the accuracy of an OFIS based HSA diagnostic test [22, 25], the area under the ROC curve (AUC) was computed to be 0.981+0.014/-0.046 with 95% confidence limits. A diagnostic test is considered "very good" if the AUC is between 0.92 and 0.97 [26], and the full 95% confidence band falls well within or above this range. Similar ROC curve generated for the HSA and monocytes in the 22 μm deep channel indicated 91% sensitivity and 94% specificity, with AUC of 0.961. The absolute channel depth is not a critical parameter of the OFIS diagnostic tool. Instructions to create a ROC curve and calculation sheet to calculate the AUC can be found in Appendix E.

Although the mode shift method [15] is no longer suitable for the analysis of HSA spectra, the transmission parameters method applied here was proven to have sufficient sensitivity and specificity to differentiate neoplastic and non-neoplastic cells, such as canine HSA and monocyte. The generality of this method was further supported by discriminating canine lymphoma and lymphocyte.

The statistical methods introduced here were later applied to other cell differentiation techniques such as the focal length and the flatness of cells. Both were derived from optical modeling, which will be discussed in the next chapter.

References:

[1] J. Voldman, “Electrical forces for microscale cell manipulation,” Annual review of biomedical engineering, vol. 8, no. 1, pp. 425 – 454, 2006.

[2] T. B. Jones, *Electromechanics of particles* (Cambridge University Press, Cambridge, 1995)

[3] Y. Huang, X. B. Wang, F. F. Becker, and P. R. Gascoyne, “Introducing dielectrophoresis as a new force field for field-flow fractionation,” Biophysical journal, vol. 73, no. 2, pp. 1118 – 1129, 1997.

[4] K. Hansen, and C. Khanna, “Spontaneous and genetically engineered animal models: use in preclinical cancer drug development,” European Journal of Cancer, vol. 40, no. 6, pp. 858-880, Apr, 2004.

[5] D. M. Vail and D. H. Thamm, “Spontaneously occurring tumors in companion animals as models for drug development”, In: Teicher BA, Andrews PA, eds. Anticancer Drug Development Guide: Preclinical Screening, Clinical Trials, and Approval, 2nd ed. Totowa, NJ: Humana Press; pp. 259-284, 2004.

[6] D. H. Thamm, “Miscellaneous Tumors: Hemangiosarcoma”, in Withrow and MacEwan’s Small Animal Clinical Oncology, 4th Edition, ed. S. J. Withrow and D. M.Vail, , Philadelphia: W.B. Saunders, pp. 785-795, 2007.

[7] A. R. Lamerato-Kozicki, K. M. Helm, C. M. Jubala, et al., “Canine hemangiosarcoma originates from hematopoietic precursors with potential for endothelial differentiation,” Experimental Hematology, vol. 34, no. 7, pp. 870-878, 2006.

[8] D. H. Thamm, E. B. Dickerson, N. Akhtar et al., “Biological and molecular characterization of a canine hemangiosarcoma-derived cell line,” Research in Veterinary Science, vol. 81, no. 1, pp. 76-86, Aug, 2006.

[9] http://en.wikipedia.org/wiki/Peripheral_blood_mononuclear_cell.

[10] R. M. Jacobs, J. B. Messick, and V. E. O. Tumors of the hemolymphatic system. In: Meuten DJ (ed). Tumors in Domestic Animals. 4th Ed. Ames (IA): Iowa State Press, pp. 119-198, 2002.

[11] W. C. Kisseberth, M. V. P. Nadella, M. Breen et al., “A novel canine lymphoma cell line: A translational and comparative model for lymphoma research,” Leukemia Research, vol. 31, no. 12, pp. 1709-1720, Dec, 2007.

[12] C. Rosales, K. A. Jeglum, M. Obrocka et al., “Cytolytic activity of murine anti-dog lymphoma monoclonal-antibodies with canine effector-cells and complement,” Cellular Immunology, vol. 115, no. 2, pp. 420-428, Sep, 1988.

[13] Z. Steplewski, C. Rosales, K. A. Jeglum et al., “In vivo destruction of canine lymphoma mediated by murine monoclonal antibodies,” In Vivo, 4(4): p. 231-4, 1990.

[14] S. E. Suter, M. B. Chein, V. von Messling et al., “In vitro canine distemper virus infection of canine lymphoid cells: A prelude to oncolytic therapy for lymphoma,” Clinical Cancer Research, vol. 11, no. 4, pp. 1579-1587, Feb, 2005.

[15] H. Shao, W. Wang, S. E. Lana, and K.L. Lear, “Optofluidic intracavity spectroscopy of canine lymphoma and lymphocytes,” IEEE Photonics Technology Letters, vol. 20, no. 5-8, pp. 493-495, Mar-Apr, 2008.

[16] V. G. Daniels, P. R. Wheater, H. G. Burkitt, “Functional histology: a text and colour atlas”. Edinburgh: Churchill Livingstone, 1979.

[17] What You Need To Know About Cancer of the Pancreas — National Cancer Institute, p. 4/5, http://www.cancer.gov/cancertopics/wyntk/pancreas, 2002.

[18] http://en.wikipedia.org/wiki/Pancreatic_cancer.

[19] Gynecologic Neoplasms at Merck Manual of Diagnosis and Therapy Professional Edition

[20] N. Auersperg, A. S. Wong, K. C. Choi, S. K. Kang, and P. C. Leung, "Ovarian surface epithelium: biology, endocrinology, and pathology". Endocr. Rev. 22 (2): 255–88, 2001.

[21] Jay. L. Devore, Probability and Statistics for Engineering and the Sciences, Thomson Brookes/Cole, 6th edition, 360-373

[22] K. H. Zou, A. J. O'Malley, and L. Mauri, “Receiver-operating characteristic analysis for evaluating diagnostic tests and predictive models,” Circulation, vol. 115, no. 5, pp. 654-657, Feb, 2007.

[23] T. Fawcett, “An introduction to ROC analysis,” Pattern Recognition Letters, vol. 27, no. 8, pp. 861-874, Jun, 2006.

[24] Margaret Sullivan Pepe, “The Statistical Evaluation of Medical Tests for Classification and Prediction,” Oxford University Press, USA; 1st edition ,2003.

[25] J. A. Hanley, and B. J. McNeil, “The meaning and use of the area under a receiver operating characteristic (ROC) curve,” Radiology, vol. 143, no. 1, pp. 29-36, 1982.

[26] P. H. Brubaker, “Do Not Be Statistically Cenophobic TIME TO ROC AND ROLL!” Journal of Cardiopulmonary Rehabilitation and Prevention, vol. 28, no. 6, pp. 420-421, Nov-Dec, 2008.

CHAPTER 7 OPTICAL MODEL

The appearance of transverse modes in the transmission spectra of the F-P cavity when loaded with cells was due to the lateral confinement of the field in the transverse direction. To further understand the origin of the transverse modes, as well as the correlation between cell shape, its refractive index (RI) profile, and the experimental transverse mode pattern, optical models of the cell-loaded cavity were constructed.

Two approaches were taken to obtaining approximate solutions for the lateral field profiles and frequencies of transverse modes in a plane-plane microresonator with a localized higher index structure: (A) to treat the configuration as an effective waveguide distributed along the entire length of the resonator; and (B) to model it within the paraxial beam approximation while regarding the high index object as an ideal thin lens. The former approach was adopted for an initial analysis of the effects of transverse confinement on longitudinal mode shifts in an OFIS study of canine lymphoma [1] and will be briefly reviewed in Section 7.1. Application of the latter approach to OFIS spectra of another canine cancer, hemangiosarcoma (HSA), will be described in Section 7.2 and analyzed in detail in later sections. In both approaches, the higher index structure of the cell provides lateral optical confinement of the beam. The majority of the discussion was presented in [1]. Additionally, a model of cell-loaded cavity with a thick cell lens settled at the channel bottom, or suspended in the middle of the channel was constructed and discussed in Section 7.5. This model helped to further understand the relationship among cell position in the channel, its shape and the transverse mode spacing in the

cell's transmission spectrum.

7.1 Overview of prior effective refractive index method

The microcavity effective index method used in [2] provided a mechanism for modeling a short resonator containing an actual index profile, $n(x,y,z)$, that varies along the z-direction (parallel to the resonator axis) by replacing it with an effective lateral index profile $n_{eff}(x,y)$ that is independent of longitudinal position in the resonator. This effective index method used was based on the effective refractive index model developed by Hadley for explaining the waveguiding effects in vertical cavity surface emitting lasers (VCSELs) fabricated by selective oxidation [3]. The basic concept of Hadley's model was that the effective index responsible for waveguiding depended primarily on lateral changes in the F-P resonance frequency.

In the OFIS system, a cell or sphere within a micro-scale F-P cavity served as an optical waveguide to laterally confine light injected from an external LED. The effective index profile, $n(x,y,z)$, that varies along the z-direction can be replaced with an effective lateral index profile $n_{eff}(x,y)$ that is independent of longitudinal position in the resonator. The effective index profile was obtained at each lateral position by determining the resonant longitudinal wavevectors, $k_z(x,y)$, of contrived one-dimensional cavities with the same longitudinal index structure at that lateral position but with no lateral index dependence. The normalized variation in the effective index was then taken to equal the normalized variation in the resonant wavevector, i.e. $\Delta n_{eff}(x,y)/n_{eff}(0,0) \approx$

$k_z(0,0)\Delta(1/k_z(x,y))$, where n_{eff} is the effective index. Similar concepts can be applied to the sphere/cell loaded F-P cavities for calculating the effective index profile from the local resonant wavelength shift.

A concentric, homogeneous RI, double sphere model of cells, similar to those adopted for optical scattering analysis [4-6] was employed in conjunction with the effective index approximation to quantitatively analyze measured canine lymphoma OFIS spectra and extract nuclear size and RI information of the cells [2]. Canine lymphocytes were used as a control for the two lymphoma cell lines investigated, and Fig. 7.1 shows the typical lymphoma and lymphocyte spectra from the 15.8 μm deep cavity used in that study.

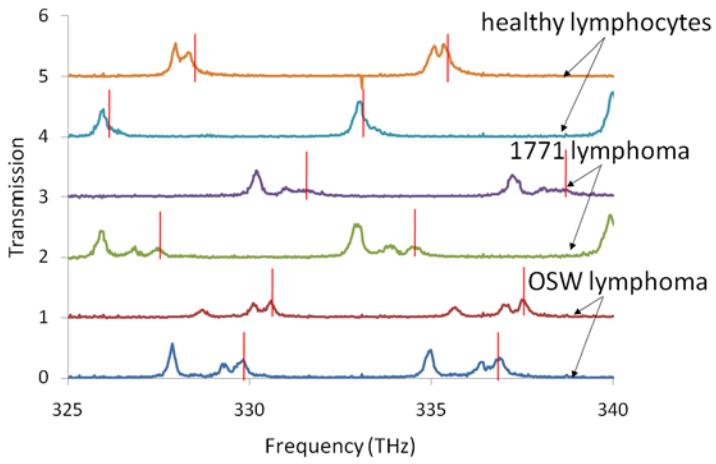

Fig. 7.1. Normalized transmission spectra of healthy canine lymphocytes and cancerous lymphoma cells from two different cell lines, OSW and 1771, in a 15.8μm deep cavity, where vertical lines indicate the bare cavity modes adjacent to each cell.

Cells from both lymphoma cell lines exhibited multi-mode behavior with two to three clear transmission peaks in each FSR. The primary peak, attributed to the fundamental mode, typically had larger intensity and peak width than the transverse modes; and it was well separated from the bare cavity resonances obtained at the test locations when the cell was removed. The wavelength shift between the bare cavity position and cell's fundamental mode was remarkably repeatable for different cells from the same cell line, with relative standard deviations of 0.1% and 2.0% for the mode shifts of the two types of lymphoma. As reported in [2], the 1771 lymphoma cell line displayed a whole cell mode shift of 21.14 ± 0.23 nm, while the Oswald lymphoma cell line displayed a whole cell mode shift of 20.36 ± 0.40 nm and a nuclear mode shift of 24.59 ± 0.13 nm. The lymphocyte control spectra had a fundamental mode as well, but no higher order transverse modes were observed for these non-cancerous cells. The lymphocytes also caused very repeatable wavelength shifts of 20.18 ± 0.30 nm [2], with a relative standard deviation of 1.5%. Statistical analysis showed that the lymphocyte and lymphoma cells could be properly categorized based on wavelength shift with a probability of error less than 10^{-14} [1].

Since the wavelength shift of cell modes from the bare cavity mode is related to the RI and size of cellular features, the concentric double homogeneous RI sphere effective index model as shown in Fig. 7.2 (a), was created to extract size and RI information of the cells [2]. Figure 7.2 (b) shows the effective RI profile of a double sphere loaded cavity in the cylindrical coordinates obtained using an effective index model, where the radial dependence of the refractive index was calculated from the cavity's resonant

wavelength using the RI distribution at each radius location by

$$d_{ball1}(r) := \left(|r| < R_1\right) \cdot \left[2 \cdot R_1 \cdot \sqrt{1 - \left(\frac{r}{R_1}\right)^2}\right] \tag{7.1}$$

$$d_{ball2}(r) := \left(|r| < R_2\right) \cdot \left[2 \cdot R_2 \cdot \sqrt{1 - \left(\frac{r}{R_2}\right)^2}\right] \tag{7.2}$$

$$n_{cav}(r) := \begin{cases} \dfrac{n_{ball2} \cdot d_{ball2}(r) + \left(n_{ball1} - n_{ball2}\right) \cdot d_{ball1}(r) + n_0 \cdot \left(L_{cav} - d_{ball2}(r)\right)}{L_{cav}} & \text{if} \quad |r| \le R_1 \\ \dfrac{n_{ball2} \cdot d_{ball2}(r) + n_0 \cdot \left(L_{cav} - d_{ball2}(r)\right)}{L_{cav}} & \text{if} \quad R_1 \le |r| \le R_2 \\ n_0 \quad \text{otherwise} \end{cases} \tag{7.3}$$

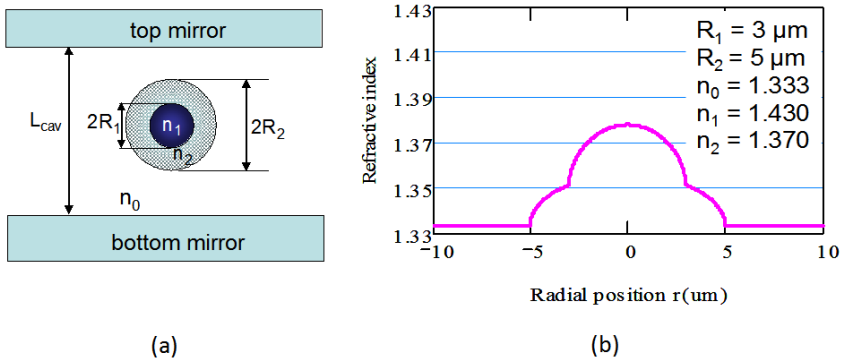

(a) (b)

Fig. 7.2 (a) Illustration of the concentric double sphere cell model in a microfluidic F-P cavity; (b) calculated effective RI profile of the double sphere loaded cavity. (Reproduced from Hua Shao PhD dissertation, Chapter 6.)

And then the cylindrical finite-difference mode solver developed by Dr. Lear was used to solve the fundamental mode, and since the longitudinal mode shift between the bare cavity mode and the cell mode was related to the cell size and RI, the cell nuclear RI or size could be calculated based on the nuclei and cytoplasm RI, as well as the nucleus-to-cytoplasm volume ratio found in the literature [5], and reported in [2].

Despite the successes of the double sphere effective index model in allowing extraction of refractive indices based on fundamental mode shifts while accounting for transverse confinement, it did not provide appropriate predictions of transverse mode number or position. The model predicted far more bound, high order transverse modes than were observed both for lymphoma and lymphocytes. Further, the computed wavelengths of the lower order transverse modes did not readily match the few peak wavelengths observed in multimode spectra. And since the effective index model provided no information on diffraction loss, it also could not predict the relative magnitude of each mode's transmission peak. The absence of many expected modes in the experimental spectra could be attributed to excessive diffraction loss of the highest order modes, but the equivalent waveguide predicted by the microcavity effective index model allowed no diffraction loss for any bound mode, nor was the longitudinal position of the cell within the cavity properly taken into consideration. The lack of agreement in transverse mode peak position and transmission magnitude, as well as consideration of cell deformability calls into question the validity of the microcavity effective index and spherical cell models in this application. In order to evaluate other simple computational methods that could more readily incorporate diffraction loss and additional information

from higher order transverse modes, an apertured paraxial Gaussian beam model, including the paraxial Gaussian beam propagation method and the analysis of the mode dependent diffraction loss, will be described in the following sub-sections.

7.2 A thin lens model

Some notable transverse mode features were found in the OFIS spectra of hemangiosarcoma (HSA) cells and motived the cell lens model. Firstly, as seen in the examples of typical normalized transmission spectra of individual HSA cells and peripheral blood mononuclear cells (PBMC) in a 25μm deep cavity shown in Fig. 7.3, the majority of HSA cells induced several new well-defined peaks with significant transmission ($T > 0.1$) that were attributed to transverse modes and are repeated within each FSR; while for non-cancerous PBMCs, such transverse mode peaks were absent or significantly weaker as observed in the previously reported [2] lymphocyte spectra, and the number of transverse mode peaks was significantly fewer in PBMC spectra. Secondly, the frequency spacing between different orders of the transverse modes was moderately uniform. And thirdly, the transmission of the transverse modes decreased at higher frequencies within each FSR. The moderately uniform spacing of the peaks and decreasing maximum transmission at higher frequencies is reminiscent of the classical spectra of nearly planar conventional stable resonators [7] and motivates the resonator analysis presented here.

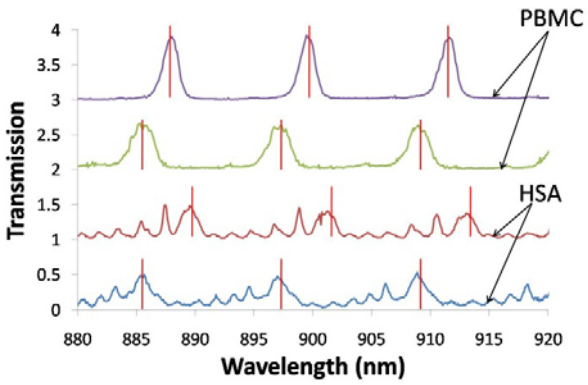

Fig. 7.3 Normalized example transmission spectra of two HSA cells and two PBMCs in a 25µm deep cavity. Vertical lines indicate the longitudinal mode resonant frequencies of the fluid filled F-P cavity without cells.

The cell spectra were taken at different locations in the channel where the cells settled. The slowly varying channel thickness, due to a mirror tilt of approximately 0.1°, slightly shifted the 4.4THz FSR of each spectrum. For reference, the longitudinal mode frequencies of the cavity, marked by vertical lines in the figure, were obtained at each cell's location by flowing the cells out of the optical path. These location specific longitudinal frequencies without cells are referred to as "bare cavity" frequencies. Mirror tilt and surface roughness dropped the finesse of the F-P cavity to 13 from the ideal value of 61 expected for R= 95% reflectivity mirrors, but the lower finesse was still sufficient to resolve multiple transverse peaks in cell spectra. Even with the cells present, attenuated and broadened peaks still occurred at the bare cavity frequencies,

presumably due to some residual light that was not coupled to the cell or light that was scattered from regions outside the cell.

Spectral similarities motivated treatment of the cell loaded plane-plane cavity for OFIS as a classic planar-concave mirror resonator using paraxial Gaussian beam analysis as described in optics textbooks [7]. Specifically, a cell settled on the bottom mirror was assumed to act as a thin lens of focal length f_{cell} and lateral radius a inside a plane-plane cavity, as pictured in Fig. 7.4. The resulting transverse mode spectrum depends on a, L_{cav}, and f_{cell}. Additionally, the cell was anticipated to cause large diffraction loss for the portion of Laguerre-Gaussian mode profiles that extend beyond the cell radius, and thus the cell was treated as opaque for radial positions where $r > a$. The goal of the following analysis was to analytically relate the transverse mode frequencies and loss to experimentally observed spectra. The resulting relationships were then used to extract f_{cell} of each individual cell and to estimate the shape of the cells' top surface from experimental transmission spectra. While the cell surface was likely to have significant aspherical aberrations and the inclusion of apertures in cavities is known to perturb the eigenmodes from ideal Laguerre-Gaussian solutions [8], these issues were neglected in the following analysis for purposes of simplification.

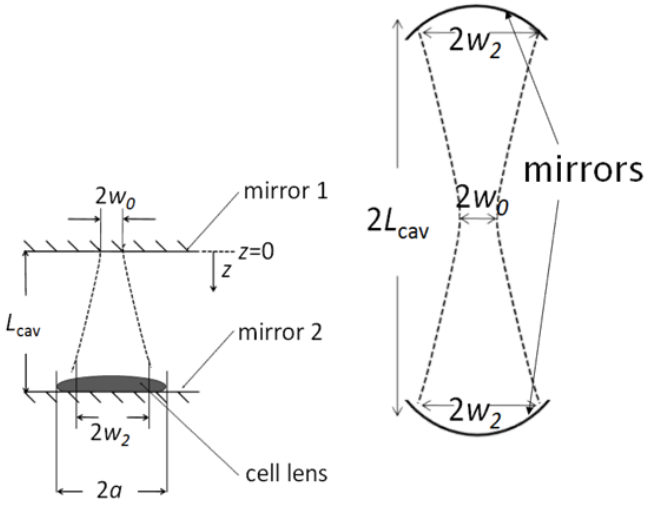

Fig. 7.4 The cell lens model of a cell-loaded F-P cavity.

7.3 Paraxial Gaussian beam propagation method and the focal length of a cell

The paraxial Gaussian beam propagation method was used to analyze the optical property of the cells such as their focal length and the shape of the top surface, as well as the mode dependent diffraction loss. The cell-loaded cavity can be considered as a half-symmetric resonator pictured in Fig. 7.4 with a Gaussian beam waist of radius w_0 at the plane mirror far from the lens. By analogy to a plane-concave mirror resonator of length L_{cav}, the beam waist at the upper mirror is [7]

$$w_0 = \sqrt{\frac{L_{cav}\lambda}{\pi}\left(f_{cell}/L_{cav} - 1\right)^{1/2}} \tag{7.4}$$

where λ is the wavelength inside the cavity. The beam radius at the cell, or equivalently the adjacent bottom mirror, is

$$w_2 = \sqrt{\frac{f_{cell}\lambda}{\pi}\left(f_{cell}/L_{cav} - 1\right)^{-1/2}} \tag{7.5}$$

The resonance frequencies of the Laguerre-Gaussian modes in the cylindrically symmetric cavity are

$$\nu_{qpm} = q\Delta\nu_{long} + (2p + m + 1)\Delta\nu_{trans} \tag{7.6}$$

where *q, p*, and *m* are the integer longitudinal, radial, and azimuthal mode indices, $\Delta\nu_{trans}$ is the transverse mode spacing, and the *g* parameter is

$$g = 1 - 2L_{cav}/f_{cell} \tag{7.7}$$

Note that in an ideal resonator, all of the transverse modes are evenly spaced in frequency. An important relationship for the subsequent analysis of cells is the ratio of transverse to longitudinal mode spacing, $\Delta\nu_{trans}/\Delta\nu_{long}$, which is related to the strength of focusing in the cavity and the Gouy phase shift of transverse modes. For the most strongly focused stable configuration, a concentric resonator where $f_{cell} = L_{cav}$, the ratio is $\Delta\nu_{trans}/\Delta\nu_{long} = 1$, and the ratio is $\Delta\nu_{trans}/\Delta\nu_{long} = ½$ for a confocal resonator with $f_{cell} = 2 L_{cav}$. Solving the relationship between the g parameter with the transverse mode spacing and equation (4) gives the cell's focal length as

$$f_{cell} = \frac{L_{cav}}{\sin^2(\frac{\pi}{2} \cdot \Delta\nu_{trans} / \Delta\nu_{long})} \tag{7.8}$$

This expression can be rigorously derived from standard resonator theory for Gaussian transverse mode frequencies [7]. The f_{cell} value of each cell can be readily calculated from the measured transverse to longitudinal mode spacing ratio and known cavity length obtained from the bare cavity FSR using equation (7.8). Once the f_{cell} value is found for each cell, it can then be used to extract the radius of curvature for the cell's top surface. The bottom of the cell is assumed to be flat against the bottom mirror of the channel while the top side is convex. The lens maker's equation for a thin plano-convex lens of constant RI n_{cell} then gives the radius of curvature as

$$R_c = f_{cell} \cdot (n_{cell} - n_{fluid}) \tag{7.9}$$

Note that this is only the curvature for the top surface of the cell, with a smaller radius of curvature at the sides of the cell as pictured in Fig. 7.4, so that R_c cannot be used to calculate cell thickness.

The focal length of HSA cells were extracted from the experimental ratio of transverse to longitudinal mode spacing of 16 cells in the 25μm deep channel, as well as another 8 cells in the 22μm one, as summarized in Table I.

Table I. Summary of spectral features of HSA cells.

	HSA cell number	Number of resolvable peaks	$\Delta \nu_{trans}$ ($\times 10^{11}$ Hz)	$\Delta \nu_{trans}/\Delta \nu_{long}$
HSA data collected from 25μm deep channel	HSA1	0	-	
	HSA2	6	6.4±1.0	0.15
	HSA3	6	6.7±0.7	0.15
	HSA4	6	6.4±1.7	0.15
	HSA5	0	-	-
	HSA6	6	7.1±0.5	0.16
	HSA7	6	5.2±1.1	0.12
	HSA8	0	-	-
	HSA9	6	5.8±1.0	0.13
	HSA10	6	6.0±1.0	0.14
	HSA11	6	5.5±1.7	0.12
	HSA12	6	5.5±1.2	0.13
	HSA13	4	4.8±3.6	0.11
	HSA14	3	5.3±0.3	0.12
	HSA15	3	5.8±1.8	0.13
	HSA16	3	5.8±1.2	0.13
HSA data collected from 22μm deep channel	HSA1	6	5.9±0.4	0.11
	HSA2	6	7.4±0.6	0.14
	HSA3	6	6.8±1.8	0.13
	HSA4	5	7.0±1.5	0.14
	HSA5	7	6.1±1.1	0.12
	HSA6	6	6.2±1.5	0.12
	HSA7	7	5.2±1.2	0.10
	HSA8	7	6.3±0.9	0.12

Similarly, the transmission spectra of 6 single cells from another canine cancer cell line, lymphoma-1771, were collected in a 21 μm deep cavity and analyzed. Although not as strong as those of the HSA spectra, multiple transverse modes with moderately uniform spacing were identified, and they were repeated in each 5.3 THz FSR. And even though

hardly any transverse mode can be found in the OFIS spectra of lymphocytes, the transmission spectra of 22 baseline monocytes were collected in a 24 μm deep cavity and up to two transverse modes could be identified in their OFIS spectra.

The focal length, radius of curvature, as well as the ratio of a cell's surface radius of curvature to its microscopic observed lateral diameter ($d = 2a$) is summarized in Table II for the three types of cells investigated. The radius of curvature of the HSA cell surface is approximately two times larger than its nominal lateral diameter as observed in a microscope, implying the top plane of the cell is very flat when it is settled at the channel bottom. Meanwhile, the canine monocytes were found to have a more curved top surface, indicating that they stay more rigid than the cancerous cells. The parameters of f_{cell} and R_c/d are potential indicators of whether a cell is cancerous or not.

Table II. Comparison of extracted parameters for neoplastic HSA and lymphoma cells, as well as non-neoplastic monocytes, in various cavities. Mean values ± standard deviation are given for cell focal length and the equivalent radius of curvature for all cancerous cells (n = 1.39 [9]) and all baseline monocytes (n = 1.37 [10]) in phosphate buffered saline solution.

Canine cell type	L_{cav} (μm)	d (μm)	f_{cell} (μm)	R_c (μm)	R_c/d
HSA	25.8±0.3	15.4±1.5	632±147	36±8.4	2.3±0.6
	22.0±0.3	15.4±1.9	601±137	34±7.8	2.2±0.6
lymphoma	21.3±0.1	12.9±0.6	324±44	18.5±2.5	1.4±0.2
monocyte	24.4±0.1	10.0±0.9	224±56	8.3±2.1	0.8±0.2

The same statistical analysis methods introduced in Chapter 6, Student's t-test and constructing ROC curves, were applied to the cell differentiation based on their focal lengths calculated with this thin lens model. Table III summarizes the calculated *p*-values of the cell classification result based on the focal lengths of cells, including the test of cancerous HSA cells and lymphoma cell against baseline monocyte, and the test among different types of cancer cells and HSA cell data collected from different cavities. Usually the threshold chosen for statistical significance is 0.05. The *p*-value of 0.631 between the focal lengths of HSA cells collected from different channel indicated that they are from the same population. This again showed that the cavity length was not a critical parameter for OFIS application. And the extremely small *p*-values between the cancerous cell lines, lymphoma or HSA, and the non-cancerous monocytes showed that the classification of these cells had very high statistical significance.

Table III. The *p*-values between the focal lengths of different types of cells.

Calculated *p*-value	HSA in 25 μm cavity	HSA in 22 μm cavity	lymphoma in 21 μm cavity	monocyte in 24 μm cavity
HSA in 25 μm cavity	1	6.31E-01	4.95E-06	2.54E-07
HSA in 22 μm cavity	6.31E-01	1	6.76E-04	1.25E-04
lymphoma in 21 μm cavity	4.95E-06	6.76E-04	1	1.29E-03
monocyte in 24 μm cavity	2.54E-07	1.25E-04	1.29E-03	1

Although the selection of cancerous cell line was limited by its availability in CSU Animal Cancer Center, the result showed that the cancer cell classification based on the focal

length of cells extracted from their OFIS spectra might have the ability to differentiate not only cancerous cells but also different types of cancer cells from each other. The biggest *p*-value of 1.29×10^{-3} occurred between lymphoma and monocytes, which was still much larger than the threshold of 0.05 and was sufficient to reject the null hypothesis.

For a preliminary assessment of clinical utility, ROC curves were also generated by varying the classification threshold with respect to the focal lengths of different types of cells, fit with t-distribution. The resulting ROC curves of the discrimination between different types of cell are shown in Fig. 7.5. As an example, one available point on the ROC curve in Fig. 7.5 (b) indicated that a diagnostic test for individual HSA cells from normal blood cells based on their focal lengths could simultaneously achieve 97% sensitivity and 99% specificity.

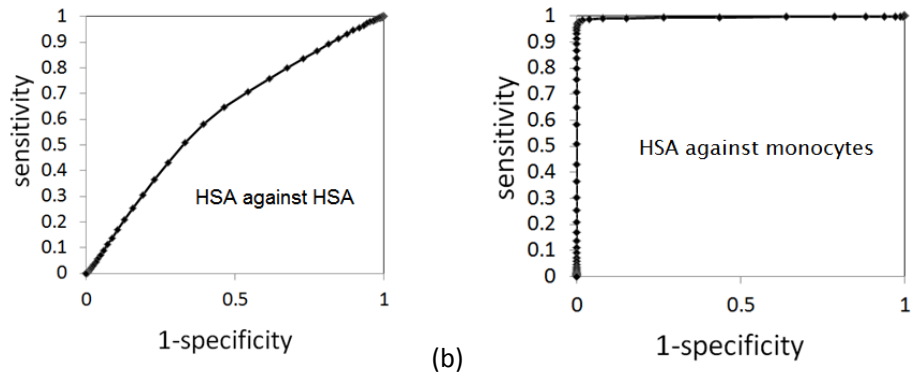

(a) (b)

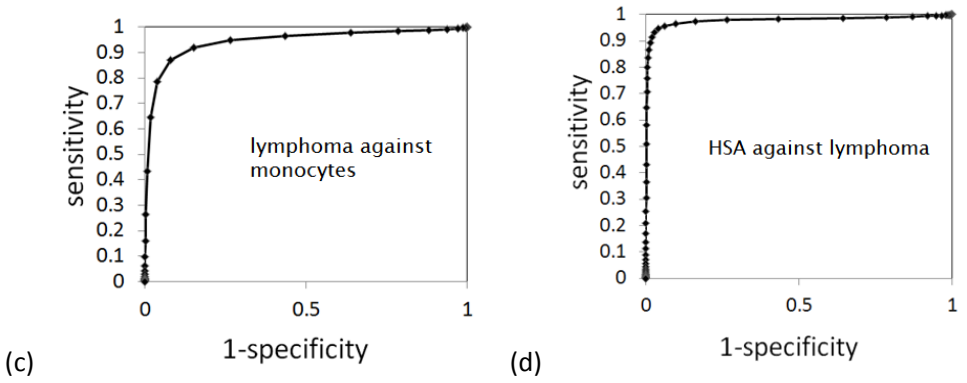

Fig. 7.5 ROC curves of (a) HSA detection in the 25µm cavity against the ones in the 22µm cavity; (b) HSA detection against monocytes; (c) lymphoma detection against monocytes; and (d) HSA detection against lymphoma, based on t-statistics of their focal lengths.

The parameter of area under the ROC curve (AUC) was used to quantify global performance. While flipping a coin would produce a almost straight line from (0,0) to (1,1) on the ROC curve and an AUC very close to 0.5, the focal lengths of HSA cells in different cavity depths produced a slightly curve line as shown in Fig. 7.5 (a) and an AUC of 0.61, which indicated that the differentiation between these cells would not be very successful. Considering they are actually from the same cell line, this is what they are supposed to demonstrate.

The ROC curves in Fig. 7.5 (b), (c) and (d) have AUC of 0.995, 0.944 and 0.978 respectively. As introduced before, a diagnostic test is considered “very good” if the AUC is between 0.92 and 0.97. These preliminary results demonstrated that the

classification based on cells' focal lengths can classify cancerous and non-cancerous cells with great sensitivity and specificity; it can also differentiate different types of cancer cells. And this makes the focal length of cells a very promising cell malignancy indicator.

7.4 Simulated transverse modes

The prediction of the transverse mode intensity is related to the mode dependent diffraction loss due to the portion of the light that misses the cell lens in the optical cavity. Beyond the relationship between focal length and transverse mode frequencies, the intensity distribution of various transverse modes is considered to estimate optical losses that impact the maximum transmission of each transverse mode. The incident LED light excites many Laguerre-Gaussian transverse modes but only the lower order ones have sufficiently narrow beam profiles to avoid large diffraction losses when interacting with the fixed radius cell. The field profile of the Laguerre-Gaussian modes [7] is

$$E_{pm}(r, w(z)) = \sqrt{\frac{2p!}{(1+\delta_{0m})\pi(m+p)!}} \cdot \frac{(\frac{\sqrt{2}r}{w(z)})^m}{w(z)} \cdot L_p^m \cdot e^{-\frac{r^2}{w(z)^2}} \tag{7.10}$$

where r is the radial position, z is the longitudinal position, $w(z)$ is the beam radius, δ_{0m} = 1 if m = 0 and is zero for m > 0, and the generalized Laguerre polynomials L_p^m are [11]:

$$
\begin{aligned}
L_0^{(m)}(x) &= 1 \\
L_1^{(m)}(x) &= -x + m + 1 \\
L_2^{(m)}(x) &= \frac{x^2}{2} - (m+2)x + \frac{(m+2)(m+1)}{2} \\
L_3^{(m)}(x) &= \frac{-x^3}{6} + \frac{(m+3)x^2}{2} - \frac{(m+2)(m+3)x}{2} + \frac{(m+1)(m+2)(m+3)}{6} \\
&\vdots
\end{aligned}
\tag{7.11}
$$

While the beam radius parameter, *w(z)*, does not depend on the mode indices *p* and *m*, higher order modes have broader intensity profiles as shown in Fig. 7.6. The example mode profiles in the figure are computed at a distance of 20 μm from a beam waist of w_0 = 4 μm – dimensions consistent with a 20 μm cavity length and 600 μm focal length, similar to the case of a 25 μm cavity loaded with HSA cells. If the cell causing the focusing had a radius of a = 10 μm, then almost all of the fundamental mode would fall within the cell radius, but the third lobe of the (p = 1, m = 0) mode would almost completely miss the cell. The portion that misses the cell lens becomes diffraction or clipping loss, causing the maximum transmission of that mode to decrease. A full calculation is provided in Appendix F.

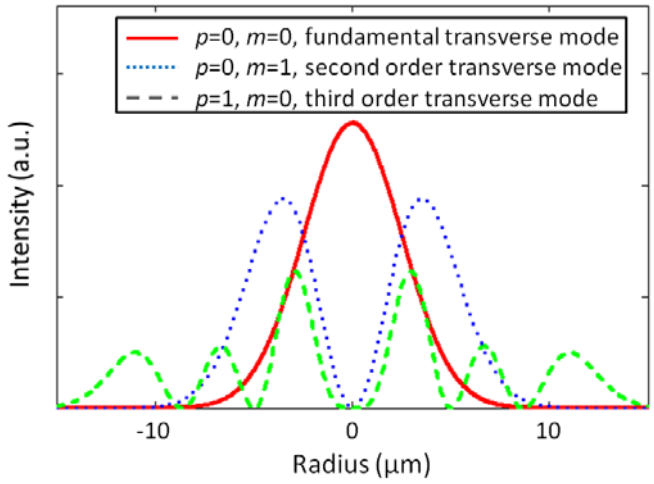

Fig. 7.6 Intensity profile of the fundamental and two higher order Laguerre-Gaussian modes after they propagate 20 μm away from a beam waist of w_0 = 4 μm.

For the analysis presented here, it is assumed that the mode tails at a radial position greater than the cell radius (i.e., $r > a$) will be lost, resulting in mode dependent diffraction loss. The loss for each mode is taken to be the integral of the normalized intensity beyond the cell of radius, $r > a$, since light in that region will not be refocused by the lens but will continue to diffract. Thus the fraction of the optical power that is not lost on each roundtrip through the cell can be thought of as the mode specific transmission of an aperture of radius a,

$$T_a = \frac{2\pi\int_0^a E_{pm}^2(r,w_2)r\cdot dr}{2\pi\int_0^\infty E_{pm}^2(r,w_2)r\cdot dr} = \frac{\int_0^{r/a=1} E_{pm}^2\left(\frac{r}{a},\frac{w_2}{a}\right)\frac{r}{a}d\left(\frac{r}{a}\right)}{\int_0^{r/a=\infty} E_{pm}^2\left(\frac{r}{a},\frac{w_2}{a}\right)\frac{r}{a}d\left(\frac{r}{a}\right)} \tag{7.12}$$

Note that this is the roundtrip loss based on the approximation that the lens is effectively in the plane of the bottom mirror and that negligible diffraction occurs during the beam propagation from the cell to the lower mirror and back to the cell.

The calculated aperture or cell transmission, T_a, can be related to the expected OFIS transmission spectrum by noting that diffraction loss out of the mode inside the cavity effectively mismatches the mirrors of nominally identical reflectivity, R, causing a reduction in the maximum transmission for each mode in the F-P cavity to a value less than unity. The maximum transmission of a F-P cavity with internal loss [7] that results from an aperture with transmission of T_a is

$$T_{\max} = \frac{(1-R)^2 T_a}{(1-R\sqrt{T_a})^2} \tag{7.13}$$

Fig. 7.7 and Table IV illustrates and summarizes the maximum transmission of different modes calculated with equations (7.10)-(7.13) with the parameters L_{cav} = 25 μm, f_{cell} = 632 μm, and a = 7.7 μm. These values were extracted from HSA cell experiments in the 25 μm deep channel. According to equation (3), the transverse frequency contribution depends on 2p+m+1, creating some degeneracy in mode frequency. Thus more than one combination of p and m exist for higher order transverse mode frequencies although modes at the same frequency have comparable maximum transmission. The same L_{cav}, f_{cell} and a parameters from the HSA experiments and R=96% was used for the simulation.

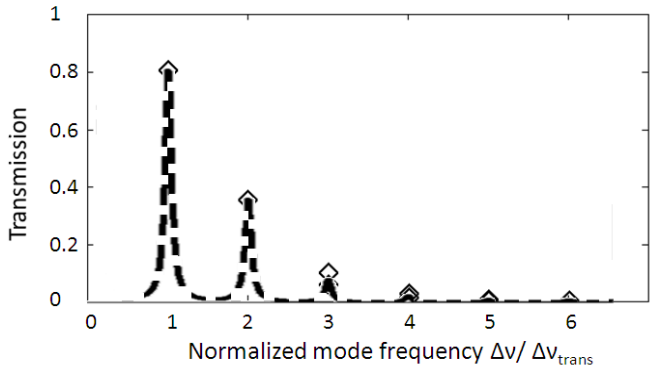

Fig. 7.7 Maximum transmission for different transverse modes an ideal cell-loaded F-P cavity, calculated from parameters described in the text.

Table IV. The simulated maximum transmission for different transverse mode numbers.

p	m	mode number $2p+m+1$	T_{max}
0	0	1	0.804
0	1	2	0.356
0	2	3	0.100
1	0	3	0.058
0	3	4	0.027
1	1	4	0.012
0	4	5	0.008
1	2	5	0.005
2	0	5	0.005
0	5	6	0.003
1	3	6	0.004
2	1	6	0.005

Fig. 7.7 clearly shows that the peak transmission decreases as mode order increases, due to the increasing mode dependent aperture loss when a greater and greater fraction of the intensity profile misses the cell lens. This same trend is observed in the transmission spectrum of HSA cells shown in Fig. 7.3. Within a transverse mode group, the fundamental mode has the lowest loss and thus the highest transmission of all the transverse modes induced by introducing a HSA cell into the cavity. Within each FSR, transverse modes at higher frequencies, i.e. higher order modes, have decreasing peak transmission in agreement with the model. Careful quantitative comparison of the model and experimental results shows that the experimental lower order modes have smaller transmission than predicted while the rate of decrease in the experimental peak transmission is not as rapid as the model indicates. These quantitative differences may be due to approximations made to simplify the model, or scattering from cell RI inhomogeneities. Further characterization of the cell-loaded cavity with a thick lens model and inclusion of aberrations and self-consistent solutions of the resonator modes may reduce this disagreement.

7.5 A thick lens model

A model treating a cell settled or suspended in a cavity as a thick lens was developed. It helped further reveal the relationship between a cell's transverse modes in its OFIS spectra and its morphology including shape and radii of curvature of top and bottom surfaces, and its vertical location in an OFIS cavity.

The ray transfer matrix method was used to calculate the Guoy phase shift of a cell loaded cavity, treating the cell as a thick lens. In the thick lens model, there are independent parameters that can be changed separately to describe the cell's thickness, the radii of curvature of the top and bottom surfaces, and its position in the cavity.

As a general case, a cell with the parameters shown in Fig. 7.8 was put inside a cavity and the Guoy phase shift of a round trip inside the cavity was analyzed. Fig. 7.8 illustrates a cell loaded cavity turned by 90°. The cell has a lateral radius of *r*, a thickness of t_{cell}, and a refractive index of n_{cell}. The radius of curvature of this cell's top and bottom surfaces are *Radius_1* and *Radius_2*, respectively. The cavity with a depth of L_{cav} is filled with medium with refractive index of n_{cav}. The cell is a certain distance away *d* from the channel bottom. The calculation starts at the top mirror of the cavity. The top surface of the cell has a negative radius of curvature (-*Radius_1*) because it is a concave surface.

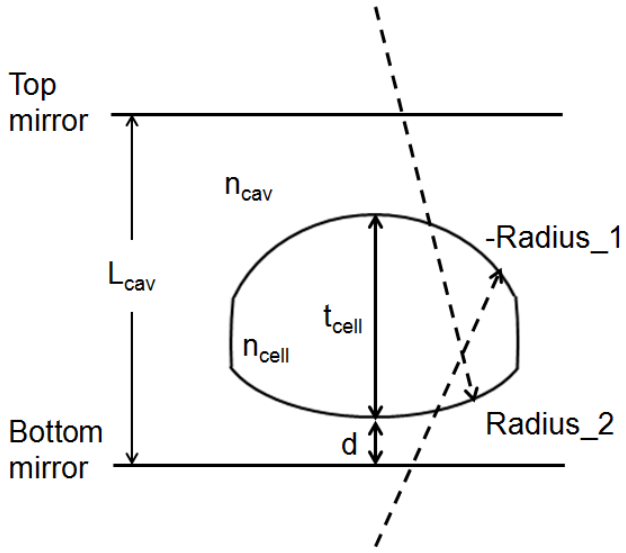

Fig. 7.8 Illustration of parameters in thick lens model

The ABCD matrix describes the thick ball lens is

$$M_{cell}\left(t_{cell}, n_{cell}, n_{cav}, Radius\_1, Radius\_2\right) := \begin{pmatrix} 1 & 0 \\ \frac{n_{cell} - n_{cav}}{-Radius\_1} & 1 \end{pmatrix} \begin{pmatrix} 1 & \frac{t_{cell}}{n_{cell}} \\ 0 & 1 \end{pmatrix} \cdot \begin{pmatrix} 1 & 0 \\ \frac{n_{cav} - n_{cell}}{Radius\_2} & 1 \end{pmatrix} \tag{7.14}$$

In order to make the calculation applicable to more general cases, a normalized sphere position is defined as

$$\rho = \frac{d}{\left(L_{cav} - t_{cell}\right)}. \tag{7.15}$$

The ABCD matrix for free space propagation from the bottom mirror to the bottom of ball lens is

$$M_b\left(\rho, L_{cav}, n_{cav}, t_{cell}\right) := \begin{bmatrix} 1 & \frac{\rho \cdot \left(L_{cav} - t_{cell}\right)}{n_{cav}} \\ 0 & 1 \end{bmatrix}, \tag{7.16}$$

while the one for free space propagation on the other side of the ball lens to the top mirror is

$$M_t\left(\rho, L_{cav}, n_{cav}, t_{cell}\right) := \begin{bmatrix} 1 & \frac{(1-\rho) \cdot \left(L_{cav} - t_{cell}\right)}{n_{cav}} \\ 0 & 1 \end{bmatrix}. \tag{7.17}$$

Reflection on mirrors is described by identity matrix $\begin{pmatrix} 1 & 0 \\ 0 & 1 \end{pmatrix}$. Since the ray transfer matrices may be multiplied to express the combinations of optical components, the round trip matrix is calculated to be

$$M_{RT}=M_t \cdot M_{cell} \cdot M_b \cdot M_b \cdot M_{cell} \cdot M_t = \begin{pmatrix} A & B \\ C & D \end{pmatrix}, \qquad (7.18)$$

where A, B, C and D are elements of the resulting round trip matrix M_{RT}.

The Guoy phase shift of transverse mode from corresponding longitudinal mode can be calculated by modifying equation (26), page 785 from [7]:

$$\exp(j \cdot \psi_G) = \frac{A + \frac{B}{\tilde{q}}}{\left| A + \frac{B}{\tilde{q}} \right|}, \qquad (7.19)$$

where ψ_G is Guoy phase shift and $\tilde{q}$ is the complex radius of curvature of this optical system defined in equation (3) on page 816 from [7]:

$$\frac{1}{\tilde{q}} = \frac{D-A}{2 \cdot B} - \frac{1}{B} \cdot \sqrt{\left(\frac{A+D}{2} \right)^2 - 1}. \qquad (7.20)$$

Since Guoy phase shift is related to the ratio of transverse- to longitudinal mode spacing by

$$\frac{\Delta \nu_{trans}}{\Delta \nu_{long}} = \frac{\psi_G}{\pi} \quad . \tag{7.21}$$

With equation (7.19) – (7.21), one can easily extract the Guoy phase shift value from experimental data.

The Guoy phase shift in a cavity where a flat cell settles on the channel bottom (which corresponds to previous thin lens approximation) is plotted in Fig. 7.9, with the parameters acquired from canine HSA cells' spectra and thin lens model. More specifically, the assumption is that the cell is settled at channel bottom, with a flat cell bottom and a radius of curvature of 35µm. The complete parameters used for this plot was (ρ, L_{cav}, n_{cav}, t_{cell}, n_{cell}, *Radius_1*, *Radius_2*) = (0, 25µm, 1.33, t_{cell}, 1.39, 35µm, 1000µm). The experiment extracted ratio of transverse- to longitudinal mode spacing was 0.12, corresponding to a Gouy phase shift of 3.77. And the cell thickness reading from the plot is 6.46 µm. Even though if the cavity length at the exact location where cell spectrum was taken is know, the cell thickness can be inferred from the longitudinal mode shift in cell spectrum, this information is usually not taken down during experiments. The cavity length could also be calculated if multiple cavity spectra were taken so that the mirror tilt could be taken into consideration. From the simulation it can only be concluded that this thickness value is within the reasonable range. Full simulation sheet can be found in Appendix G.

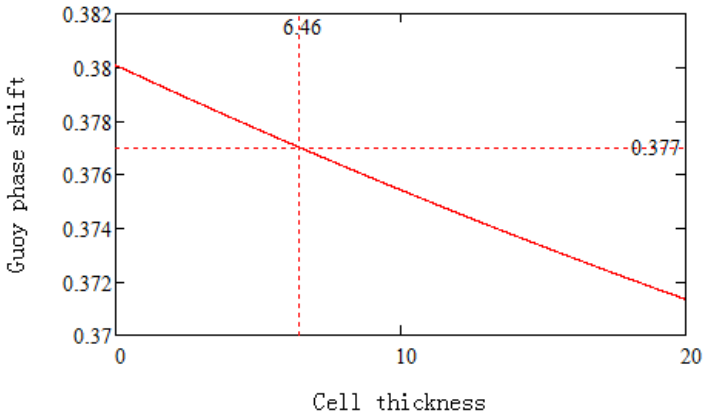

Fig. 7.9 Simulated Guoy phase shift, using parameters extracted from canine HSA cell spectra and thin lens model.

Also, the cell location and the radius of curvature of cell surfaces cannot be experimentally confirmed with our apparatus. However, the Guoy phase shift can be plotted for a few different cases. Firstly, a rigid, symmetric cell settles on the channel bottom, i.e., the radii of curvature for cell top and bottom surfaces are the same. The relation between cell thickness and the radius of curvature (both top and bottom) with the same Guoy phase shift of 3.77 can be plotted, as shown in Fig. 7.10.

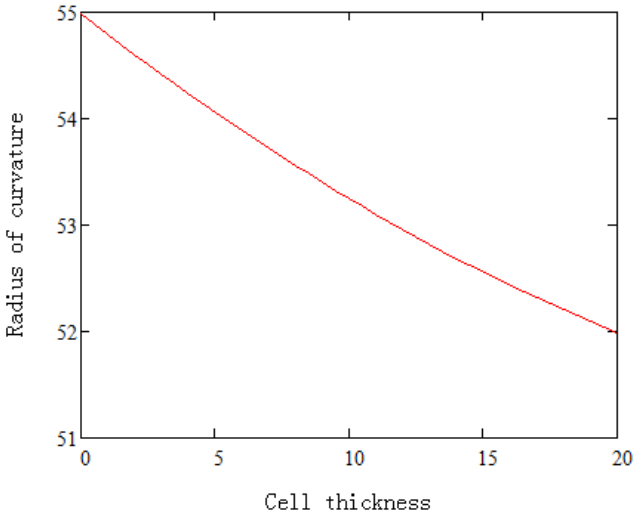

Fig. 7.10 Simulated radii of curvature of cell surfaces, using parameters extracted from canine HSA cell spectra and thick lens model.

If this rigid cell is round (i.e., t_{cell} = 2r) and floating in the channel, the radius can be plotted against cell position in the channel. From Fig. 7. 11, one can find out that since a hidden assumption for this case is that r = *Radius_1* = *Radius_2*, this lateral radius of the cell exceeds the cavity length, which is invalid.

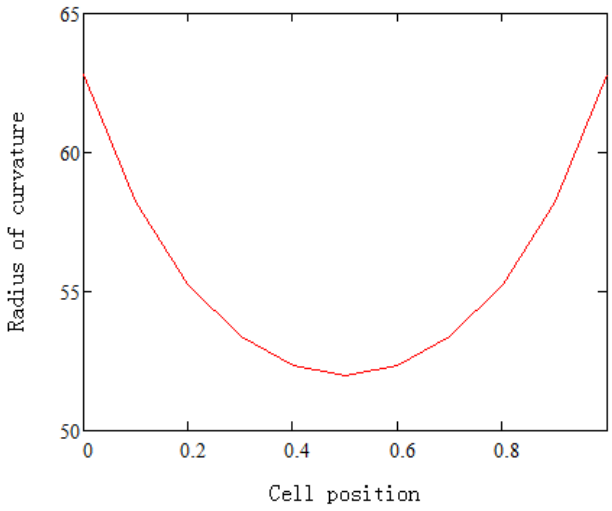

Fig. 7.11 Simulated radii of curvature of cell surfaces when cell is floating, using parameters extracted from canine HSA cell spectra and thick lens model.

This thick lens model will be used to analyze OFIS spectra when increasing voltage is applied on cells.

References

[1] W. Wang, D.W. Kisker D.H. Thamm, H. Shao and K. L. Lear, “Optofluidic Intracavity Spectroscopy of Canine Hemangiosarcoma,” IEEE Transactions on Biomedical Engineering, DOI: 10.1109/TBME.2010.2045893, in press, 2010.

[2] H. Shao, W. Wang, S. E. Lana, and K. L. Lear, "Optofluidic intracavity spectroscopy of canine lymphoma and lymphocytes," *IEEE Photonics Technology Letters*, vol. 20, no. 5-8, pp. 493-495, Mar-Apr, 2008.

[3] G. R. Hadley, "Effective-index model for vertical-cavity surface emitting lasers", *Optics Letters*, vol. 20, no. 13, pp. 1483-1485, Jul 1995.

[4] P. M. A. Sloot, A. G. Hoekstra and C. G. Figdor, "Osmotic response of lymphocytes measured by means of forward light scattering: theoretical considerations," *Cytometry*, vol. 9, no. 6, pp. 636-641, Nov 1988.

[5] C. G. Liu and C. E. Capjack, "Effects of cellular fine structure on scattered light pattern," *IEEE Transactions on Nanobioscience*, vol. 5, no. 2, pp. 76-82, Jun 2006.

[6] K. W. Keohane and W. K. Metcalf, “The cytoplasmic refractive index of lymphocytes, its significance and its changes during active immunization”, Q J Exp Physiol. Cogn. Med. Sci., vol. 44, pp. 343, 1959.

[7] A. E. Siegman, Lasers, Mill Valley, CA: University Science, Chapter 19, 1986.

[8] T. Li, "Mode selection in an aperture-limited concentric maser interferometer," Bell System Technical Journal, vol. 42, no. 6, pp. 2609-2620, 1963.

[9] X. J. Liang, A. Q. Liu, C. S. Lim, T. C. Ayi and P. H. Yap, "Determining refractive index of single living cell using an integrated microchip," *Sensors and Actuators A-Physical*, vol. 133, no.2, pp. 349-354, Feb 2007.

[10] V. A. Loiko, G. I. Ruban, O. A. Gritsai, V. V. Berdnik, and N. V. Goncharova, "Mononuclear cells morphology for cells discrimination by the angular structure of scattered light,” *10th International Conference on Electromagnetic and Light Scattering by Nonspherical Particles*, Bodrum, Turkey, 17-22 June, 2007.

[11] G. E. Andrews, R. Askey and R. Roy, "Laguerre Polynomials," Special Functions, Cambridge, England: Cambridge University Press, pp. 282-293, 1999.

CHAPTER 8 PRELIMINARY RESULTS ON CELL DEFORMATION

This chapter introduces the motivation, approaches and some preliminary results on an application of DEP trap enabled OFIS chips. The idea is to employ the 3-D trap designs described in Chapter 3, and by raising the voltage of the DEP traps, the increasing electric field strength would clamp the trapped cell tighter and tighter. And since the OFIS spectrum is very sensitive to the changes in refractive index profile inside the fluidic resonant cavity, a change in the spectrum is expected if there is indeed a cell shape change. The cell deformation information could be used for the differentiation among cancer cell lines.

Section 8.1 presents a more detailed motivation for this work and experimental approaches taken. Section 8.2 shows OFIS spectra collected from two OSA cell lines with different metastatic potentials, with varying trapping voltage. Section 8.3 analyzes these data collected with chips constructed with borosilicate substrates. And based on COMSOL simulation and experimental observation, additional data was collected with chips built with sapphire substrates. The OFIS spectra of settled and suspended HSA cells collected with sapphire chip are summarized in Section 8.4 and analyzed with thick lens model in Section 8.5.

8.1. Motivations and approaches

Recent studies have shown that the metastatic potential of tumor cells is related to the ability to deform their cytoskeleton, allowing motility and invasion [1-7]. In this study, the mechanical deformability of two murine osteosarcoma (OSA) cell lines, K7M2 and K12 with different metastatic potentials was investigated.

Canine Osteosarcoma (OSA) is a rapidly growing, destructive neoplasm of bone that accounts for 80% of malignant bone tumors in dogs [8]. To provide an investigative tool for the study of OSA biology, a syngeneic (balb/c) murine model using cell lines derived from a spontaneously occurring murine OSA have been developed. The development and use of a more aggressive OSA cell line (K7M2) resulted in spontaneous metastasis to the lungs in over 90% of mice, whereas metastases were seen in only 33% of mice when a less aggressive OSA cell line (K12) was used [9].

In order to investigate the difference in deformability properties between cells from these two cell lines, (DEP) force was applied to individual cells to first trap the cell and facilitate the data collection; and then the trapping voltage which determined the strength of the DEP force was increased to apply higher clamping force upon the trapped cell. Using the 3-D trap design introduced in 3.1.2, also in an attempt to avoid the cell drifting problem mentioned in the same section, a funnel, trap and steer (FTS) electrode pattern was designed. And the electrode layout of the OFIS chip, after flip-chip bonding, is shown in Fig.8.1, with the horizontal lines indicating the edges of the 200μm wide microfluidic channel.

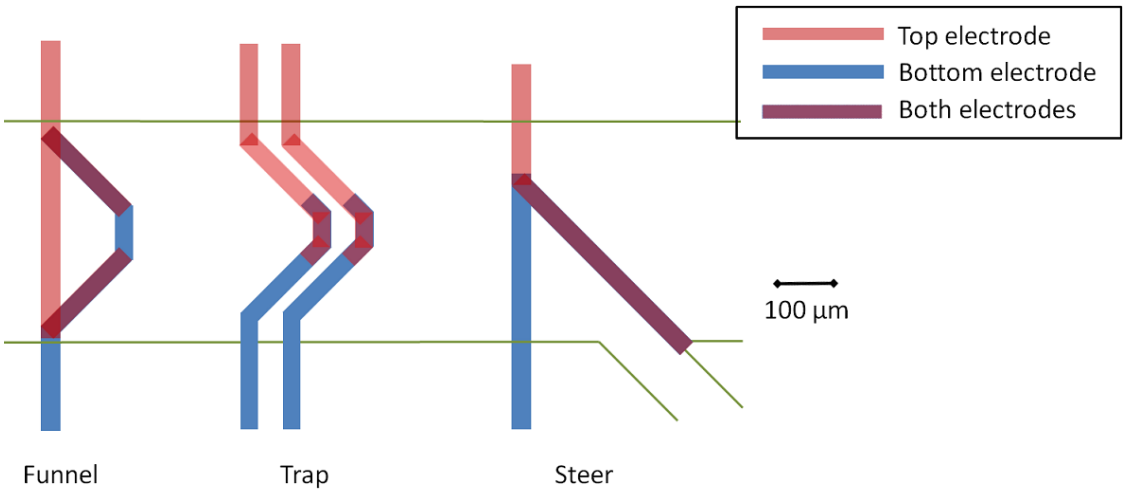

Fig. 8.1 The electrode layout on a flip-chip bonded FTS chip.

The cell shape changes, if any, would be indirectly acquired through the changes in transmission spectra collected with the OFIS technique, while the trapping voltages for DEP traps are increased. It is understood that the cavity depth (i.e. the spacing between the top and bottom electrodes) would affect the electric field distribution and thus the clamping strength, so one OFIS chip with similar cavity depths along the channel was used.

The frequency of the AC signal used was 50MHz, unless otherwise specifically stated. And the AC voltages referred to below were the settings on the function generator. It was reported [10] that the attenuation of the cables and adaptors used for electrical connection was not negligible at high frequencies of over 25MHz, which were the frequencies used for nDEP trapping. As a result, one should be aware of the fact that the

actual voltages applied on the DEP electrodes are likely to be lower than the voltage settings on the function generator.

8.2. Results on two OSA cell lines with different metastatic potentials

With the same FTS chip, OFIS spectra of 24 cells from the metastatic OSA-K7M2 cell line and 24 cells from the nonmetastatic OSA-K12 cell line were acquired, and the change in the transverse-mode patterns when the trapping voltage was increased was analyzed. At first each cell was trapped with relative low voltage (4V, 50MHz) at a flow velocity of approximately 50μm/sec. Multiple transverse modes were found in the OFIS spectra of cells from both cell lines, as shown in the examples in Fig. 8.2, indicating the cells were cancerous.

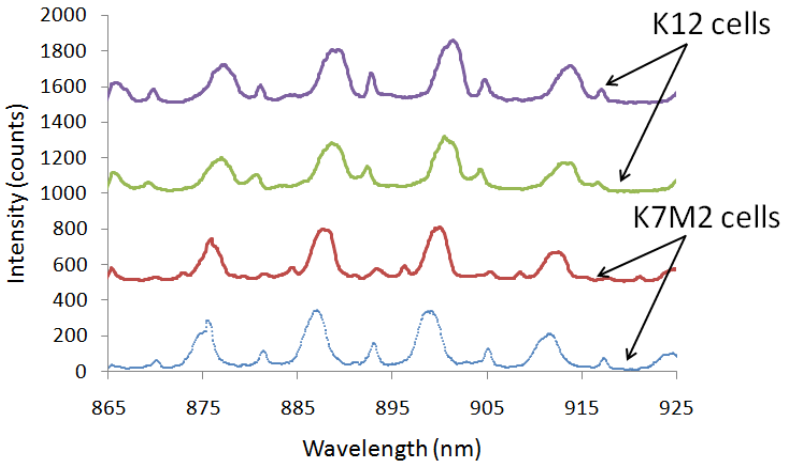

Fig. 8.2 Example of raw transmission spectra of K12 and K7M2 cells.

And then an increasing trapping voltage was applied to each cell. Each spectrum was collected approximately 1 minute after changing the trapping voltage, in case the cell membrane might have a relatively long relaxation time, even though others have measured the relaxation time to be within 1 second [11-13]. Fig. 8.3 shows the voltage dependent transmission spectra of one K7M2 cell, from the bottom to top: at the beginning when it was trapped with low voltage (4V, 50MHz), only one noticeable transverse mode was found in the FSR, and the second transverse mode appeared when the voltage was increased (with 1V increment) to 6V, and the third mode showed up after the trapping voltage was further increased to 9V. The majority of the K7M2 cells and K12 ones had additional transverse modes generated when the trapping voltage was increased, and it might be due to a change in cell size, shape, or biological properties of the intercellular components which in turn affect the refractive index. The bare cavity peak (which was the peak with the highest transmission intensity) blue shifted (to the shorter wavelength) a bit, due to the reduced refractive index of water caused by the Joule heating generated by increased voltage.

The top curve in Fig. 8.3 was acquired after the voltage was decreased back to 4V for 1 minute, to find out whether the cell deformation (if this was what was observed) was reversible. And even though more time (up to 5 minutes) was allowed for relaxation, or less voltage (down to 0V) was been applied, hardly any cells exhibited a spectrum with similar transverse mode patterns (including the number, the location and spacing) as in the initial spectrum. This indicated that some irreversible damage was caused to the cells during the experiments; I believed that it was denaturation due to Joule heating,

and Joel Kindt thought it was asmotic swelling due to the electroporation caused by the electric field. Denaturation is a process in which proteins or nucleic acids lose their tertiary structure and secondary structure by application of some external stress or compound, including heat [14]. It also could be seen in Fig. 8.4 that the cell "shrunk" when higher voltage was applied; however, the cell size stayed small (picture not available) even after the voltage was removed (and the cell was temporarily stuck inside the trap), yet again indicating that some irreversible damage was caused to the cells and might have killed them. A series of systematically designed experiments were carried out to investigate the effect of changing chip substrate and increasing DEP exposure dose on cell viability. These results are presented in Chapter 9.

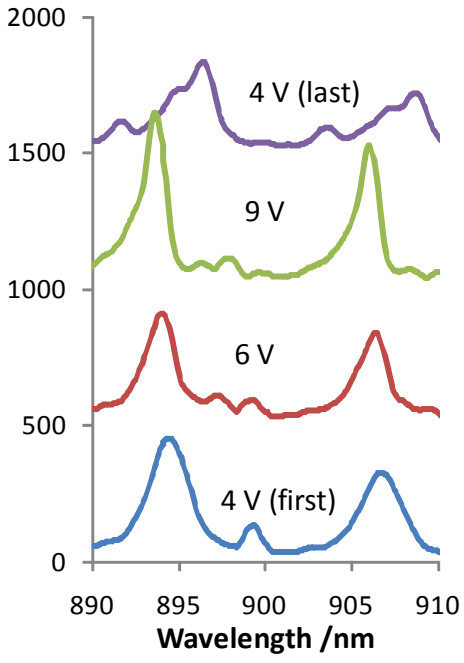

Fig. 8.3 Examples of raw transmission spectra of an OSA-K7M2 cell after varying trapping voltage.

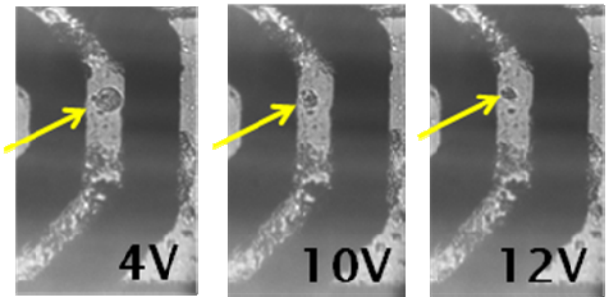

Fig. 8.4 Size change of another OSA -K7M2 cell under 5X microscope.

For the images shown in Fig. 8.4, a blue LED was used to replace the infrared LED as bottom illumination, so that a better resolution could be achieved. And in the same images, the debris inside of the trap was accumulated after a few experiments and cannot be removed by normal channel flush routine.

8.3. Analysis of cell spectra acquired from borosilicate chips

The number, location and frequency spacing of the transverse modes were used as indicators of whether there were changes in the cell size or shape, even though there was a lack of understanding of whether the intercellular structure was changed or damaged permanently when the DEP voltage was applied. Out of 24 OSA-K7M2 cell spectra, 20 of them showed additional transverse modes when the trapping voltage was increased from 4V to typically 10V, or occasionally 12V (based on whether the emerging of the next new mode is visible or not); but the other 4 demonstrated no additional modes except for the change in their intensity. Only 2 OSA-K12 cells behaved in a similar

way, where no additional transverse modes were found, except for intensity change in their original transverse modes; and there were another 2 cells that exhibited a reduced number of modes as the DEP force went up. The spectra presented in Fig. 8.3 may due to the intercellular component changes that affected the index of the cell, or simply the physical size change, or simply due to biochemistry and index change attributed to cell denaturation. The metastatic potential of murine cancerous cells is known to be associated with the deformability of the cells [15], which indicate that the higher metastatic potential K7M2 cells would likely be more deformable than the lower metastatic potential K12 cells. At first the preliminary observation of spectral changes appeared to be consistent with their deformability, further comparison below showed that these changes didn't have enough statistical significance between K7M2 and K12 cell lines.

When the additional modes showed up as the trapping voltage was increased (with 1V increment), that voltage was recorded and summarized in Table I. Under the same clamping voltage of up to 12VAC, while cells from the more metastatic cell line (K7M2) generated up to 4 new transverse modes, the cells from the less metastatic one (K12) only generated up to 2 additional modes. It was also noticed that for the majority (20 out of 24 for each cell line) of the cells from both cell lines, at least 1 additional mode was generated when the clamping voltage was increased, however, more cells in the K12 cell line required higher clamping voltage to generate their first additional modes than in the K7M2 cell line.

Table I: Summary of the transverse mode pattern of 48 OSA cells.

OSA-K7M2						OSA-K12			
cell#	original # of transverse modes @4V	1st addtional modes	2nd addtional modes	3rd addtional modes	4th addtional modes	cell#	original # of transverse modes @4V	1st addtional modes	2nd addtional modes
1	1	8				1	2	10	
2	1					2	1	6	
3	2	5	9			3	1	10	
4	1	6	7			4	1	8	
5	1	6	9			5	2		
6	2	8				6	2		
7	1					7	2	10	
8	1	6	8	10	11	8	2	8	
9	2	7				9	2	9	
10	2	8	9			10	1	6	11
11	2	5	7	8		11	1	8	
12	2	7				12	2		
13	1					13	1	9	
14	2	10				14	1	11	
15	2	5	8			15	2	7	
16	2	6	7			16	2	6	
17	3	5				17	1	8	11
18	3	9	10			18	1	8	
19	1	7				19	3	5	6
20	3	8				20	3	5	6
21	3					21	1	9	10
22	3	6	7			22	1	5	12
23	3	5				23	3	6	
24	3	6				24	4		

On the other hand, when up to 12VAC was applied on individual cells, the cells from OSA-K7M2 cell line were able to generate up to 4 additional transverse modes, while the cells from the less metastatic cell line, K12, were only able to generate up to 2 additional modes. However, these differences observed were not yet sufficient to differentiate cells from the two OSA cell lines, as indicated by the two overlapping populations plotted in Fig. 8.5; nor did it offer a potential algorithm to realize real-time cell sorting based on the spectral change at different clamping voltage.

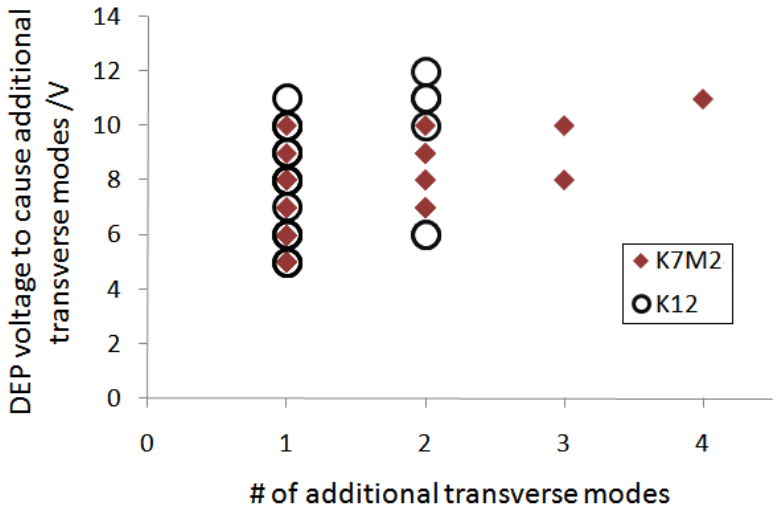

Fig. 8.5 Transverse mode patterns of 40 OSA cells that generated additional modes with increasing clamping voltage.

Flo these preliminary results, it is hard to correlate these results with the deformability of cells, or even to confirm the origin of the spectral changes observed. This may due to one or more of the following:

i. DEP force might not be big enough to deform cancerous cells;

ii. The temperature rise inside DEP structures caused the trapped cells to shrink;

iii. Analyzing the spectra with a thick lens cell model might be able to reveal more cell morphology information.

8.4. Results on settled and suspended HSA cells with sapphire chips

According to COMSOL simulation and experimental observation, using sapphire substrates significantly reduces the temperature rise inside DEP traps. Although no conclusion could be made with the data presented above, it is possible that removing the Joule heating effect by using sapphire substrates to build chips would reduce the possible heat damage to the cells and help get valid OFIS spectra from viable cells. The viability test results using a more reliable test method including DEP trap design that provides uniform DEP exposure is further discussed in Chapter 9.

The data presented here were collected from OFIS chips built with sapphire substrates. The trap design used was FTS (funnel, trap and steer) where there are two electrode bars in the center for the “trap” feature. With this quadrapole design, it was expected that a trapped cell can be suspended with DEP force. And the OFIS spectra of a suspended cell should be different from that of a settled one. Using the thick lens cell model developed in Chapter 7, the spectra of settled and suspended HSA cells are analyzed in Section 8.5.

Based on previously acquired cell data, the cell-to-cell spectrum variation can be large. In order to get results that are more comparable, attempts were made to collect spectra of the same cell, both when it was settled and then when it was suspended. During the experiments, the same flow control introduced before was used to minimize the flow rate until some cells temporarily settled at the channel bottom. Then spectra of all cells

that were in the viewing area of camera and were close to the DEP trap were taken, one at a time. Spectra were only taken from these cells because it was easier to keep track of them and make sure future data of trapped or suspended cells were going to be taken from the same cell(s). And then flow rate was slightly increased by tapping on the syringe or shaking the tubing. Some cells would move with the flow and get into the trap area. DEP electrodes were activated with relatively low trapping voltage such as 8VAC and 50MHz to trap a cell. The trapping voltage was increased in 2V increments and spectrum was taken at each voltage approximately 1 minute after the voltage was changed. In addition, another spectrum was taken 5 minutes after the trap was turned off. At that point the cell might still be in the trap, or slowly moved out of it. In the latter case the chip would be translated so that spectrum could be taken from this same cell when it was settled again, although at a new spot in the channel

OFIS spectra of over 100 cells were collected using the experimental procedure described above. In these data, 28 sets were collected from the same cell that settled and then was trapped. Usually spectra were taken with increasing voltages applied on the trapped cell. And sometimes with decreasing voltages as well, in an attempt to find out whether the spectrum change, possibly due to cell morphology change, was reversible. However, due to bizarre flow movement or asymmetric trapping strength of the DEP trap, cells often moved out of the trap before all the spectra were taken. And if cell moves out of the viewing area and cannot be confirmed if it was the same one after reversing the flow, no more spectra can be collected, or claimed to be in the same set of data.

The parameter being investigated as an indicator of whether there was cell morphology change was the frequency spacing ratio between transverse and longitudinal modes in cell's OFIS spectra. According to the thick lens model developed in Chapter7, Section 7.5, the ratio $\Delta\nu_{trans}/\Delta\nu_{long}$ is directly related to the Guoy phase shift in cell-loaded cavity, which is determined by the cell's vertical location, the top and bottom radii of curvature, as well as its thickness. Since it is a combined effect and none of these factors can be confirmed with or observed in experiments, they are only qualitatively analyzed.

The trend in $\Delta\nu_{trans}/\Delta\nu_{long}$ changes was analyzed. Among the 28 sets of spectra collected from the same 28 cells first settled and then trapped, most of their $\Delta\nu_{trans}/\Delta\nu_{long}$ frequency ratios were higher when they were settled than when they were trapped with 6VAC or 8VAC. Some typical $\Delta\nu_{trans}/\Delta\nu_{long}$ changes are plotted in Fig. 8.6.

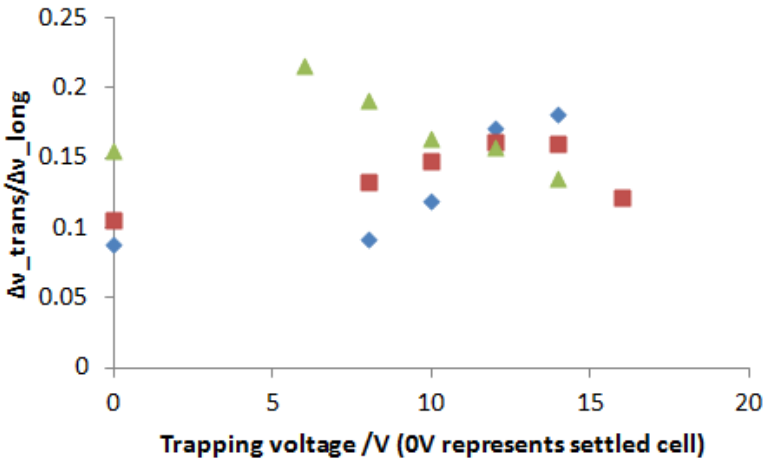

Fig. 8.6 A few common $\Delta\nu_{trans}/\Delta\nu_{long}$ change patterns observed in experimental spectra.

Direct observation of OFIS spectra and of $\Delta v_{trans}/\Delta v_{long}$ values from settled and possibly suspended cells did not reveal any conclusion. There were three major types of $\Delta v_{trans}/\Delta v_{long}$ observed as the trapping voltage increased: increasing $\Delta v_{trans}/\Delta v_{long}$, decreasing $\Delta v_{trans}/\Delta v_{long}$, increasing and then decreasing $\Delta v_{trans}/\Delta v_{long}$. There were also a few cells that have random $\Delta v_{trans}/\Delta v_{long}$ values at different trapping voltages.

8.5. Analysis on settled and suspended HSA cells with thick lens model

There are a few changes in cell morphology and the cell position in the cavity that could cause these observed $\Delta v_{trans}/\Delta v_{long}$ changes as the trapping voltage was increased. Simulation below shows how much each factor, including cell thickness, radii of curvature of top and bottom surface and cell position, affects the $\Delta v_{trans}/\Delta v_{long}$ ratio.

Firstly it was assumed that the changes might due to the lifting of the trapped cell. When cell settles at the channel bottom, the cell position factor is $\rho = 0$. And if DEP force suspends the cell to the center of the cavity, where the position factor is $\rho = 0.5$, the ratio of $\Delta v_{trans}/\Delta v_{long}$ might change a lot. Fig. 8.7 shows the simulation results using parameters of $L_{cav} = 25$ µm, $t = 15$ µm and radii of curvature of cell surfaces of $Radii = 35$ µm. It shows that the ratio changes approximately 0.1% when the cell is suspended. One can conclude that the effect of cell position on $\Delta v_{trans}/\Delta v_{long}$ ratio is negligible.

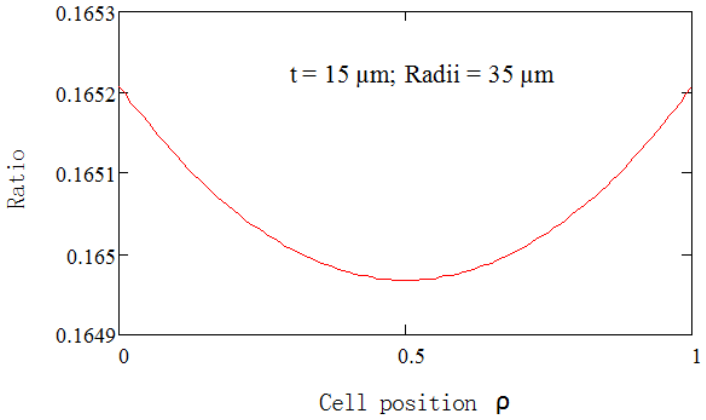

Fig. 8.7 Simulated $\Delta v_{trans}/\Delta v_{long}$ change when the cell position varies from the bottom of cavity (ρ = 0) to top of cavity (ρ = 1).

And then the effect of cell thickness was studied. Similar parameters were used, and ρ was set to be 0.3, although it has been proved that this factor hardly changes the ratio. Fig. 8.8 shows the simulation results. Changing the cell thickness from very flat to almost elliptical in the vertical direction, which is not practical based on the COMSOL simulation of DEP forces, decreases the $\Delta v_{trans}/\Delta v_{long}$ ratio by a few percent. Since DEP force increases as the trapping voltage increases, the reduction in cell thickness would result in increasing $\Delta v_{trans}/\Delta v_{long}$ ratio. However, this still might not be the dominant factor.

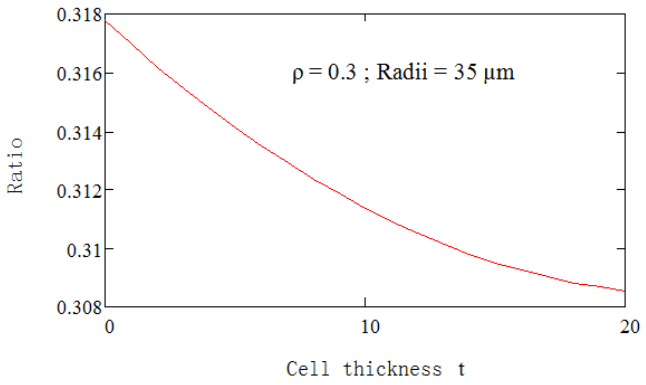

Fig. 8.8 Simulated $\Delta v_{trans}/\Delta v_{long}$ change when the cell thickness varies from extremely flat (t = 0) to spherical or even elliptical in the vertical direction (t = 20).

Lastly the changes in radii of cell surfaces were simulated and the result is shown in Fig. 8.9. The inset shows that over 30% changes could occur when the radii of curvature of top and bottom surfaces decrease from 50 to 20. This indicated that instead of cell position change during cell suspension due to DEP force, the changes in cell surface affects the $\Delta v_{trans}/\Delta v_{long}$ ratio more dramatically.

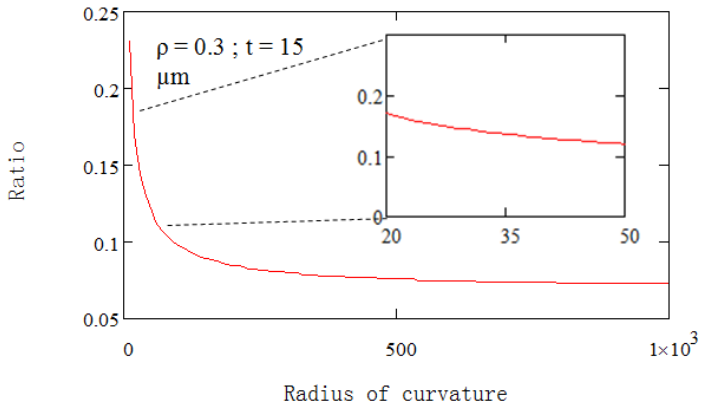

Fig. 8.9 Simulated $\Delta v_{trans}/\Delta v_{long}$ change when the radii of cell surfaces (top and bottom) vary from extremely small (Radii = 10 µm) to very flat surface (Radii =1000 µm), with inset showing the ratio change when Radii = 20-50 µm.

The simulation results help explain some of the $\Delta v_{trans}/\Delta v_{long}$ changes observed in experiments. The difference in the trend of $\Delta v_{trans}/\Delta v_{long}$ changes can be attributed to the deformability difference in cells, even though the cells under investigation were from the same cell line. Since none of the simulated factors could be experimentally observed or recorded, the analysis below is only a hypothesis and can not be confirmed. The monotonic increase in $\Delta v_{trans}/\Delta v_{long}$ may be due to the shape change on cell top and bottom surfaces induced by DEP lifting force. The increasing then decreasing pattern might because at certain trapping voltage, the cell was completely suspended and the shape change caused by clamping force from the trap made the surface become flatter. Similarly if a cell can be easily suspended and then deformed along the direction of

electrodes, in which the confining force is minimal, the $\Delta v_{trans}/\Delta v_{long}$ ratio would decrease due to the face that the radius of curvature in that direction increased.

References:

[1] K. F. Tullberg and M. M Burger, “Selection of B16 melanoma cells with increased metastatic potential and low intercellular cohesion using Nuclepore filters,” *Invasion Metastasis*, vol. 5, pp. 1–15, 1985.

[2] T. Ochalek, F. J. Nordt, K. Tullberg and M. M. Burger, “Correlation between cell deformability and metastatic potential in B16-F1 melanoma cell variants,” *Cancer Res.,* vol. 48, pp. 5124–5128, 1988.

[3] O. Thoumine and A. Ott, “Comparison of the mechanical properties of normal and transformed fibroblasts,” *Biorheology,* vol. 34, pp. 309–326, 1997.

[4] J. Sleep J, D. Wilson D, R. Simmons R and W. Gratzer, “Elasticity of red cell membrane and its relation to hemolytic disorders: an optical tweezers study.” *Biophys J*, 77:3085–95, 1999.

[5] M. Lekka, P. Laidler, D. Gil, J. Lekki, Z. Stachura and A. Z. Hrynkiewicz, “Elasticity of normal and cancerous human bladder cells studied by scanning force,” *Eur. Biophys. J.,* vol. 28, pp. 312–316, 1999.

[6] J.P. Mills, L. Qie, M. Da, C. T. Lim and S. Suresh, “Nonlinear Elastic and Viscoelastic Deformation of the Human Red Blood Cell with Optical Tweezers.” *MCB*, vol.1, no.3, pp. 169-180, 2004.

[7] M. Manimaran, Francis EH Tay, K. C. Chaw, “Cell deformation in cancer metastasis: a BioMEMS based approach.” *Journal of Physics: conference series*, vol. 34, pp. 1143–1147, 2006.

[8] Donald J. Meuten (ed), Tumors of bone and cartilage in Tumors in Domestic Animals, Berkley, University of California Press, pp. 157-230, 1990.

[9] J. Schmidt et al, Establishment and characterization of osteogenic cell-lines froma spontaneous murine osteosarcoma, *Differentiation*, vol. 38, no. 3, pp. 151-160, 1988.

[10] J. Kindt, L. Netherton and H, Cutler, senior design report, spring 2009.

[11] R. Waugh and E. A. Evans, “Viscoelastic properties of erythrocyte membranes of different vertebrate animals,” *Microvascular Research*, vol. 12, no. 3, pp. 291-304, 1976.

[12] M. Dao, C.T. Lim and S. Suresh, “Mechanics of the human red blood cell deformed by optical tweezers,” *J. of the Mechanics and Physics of Solids*, vol. 51, pp. 2259 – 2280, 2003.

[13] F. Thom, “Mechanical properties of the human red blood cell membrane at −15 °C,” *Cryobiology,* vol. 59, no. 1, pp. 24-27, 2009.

[14] http://en.wikipedia.org/wiki/Denaturation_%28biochemistry%29

[15] C. Khanna C, J. Khan, P. Nguyen P, et al., “Metastasis-associated differences in gene expression in a murine model of osteosarcoma”, CANCER RESEARCH, vol. 61, pp. 3750-3759, 2001.

CHAPTER 9 CELL VIABILITY TEST

This chapter discusses experimental work specifically designed to answer people's concern about the viability of cells after they run through the OFIS apparatus. Viability in regards to a cell refers to its ability to grow, develop, and function normally. Although no direct evidence was found, a cell's viability might change its refractive index profile and thus affect its OFIS spectrum. This becomes a major concern when cell shrinking caused by heating effects from DEP traps was observed in experiments. Another concern is the time dependence of cancerous cell viability, for usually cells were used up to 36 hours after they were taken out of culture media and re-suspended in PBS. Section 9.1 briefly discusses the motivation of this work. Section 9.2 presents the experimental method of time dependent viability test and experimental apparatus for getting the cell samples through the microfluidic channel and DEP traps. Section 9.3 compares the viability results of cells run through microfluidic channel and DEP traps constructed on two substrates with different thermal conductivities.

9.1 Motivation

The time dependency of the viability of cancerous cells was of interest since biological cells, instead of micro particles, were used in OFIS experiments. The cell lines, including canine lymphoma, canine HSA and murine OSA, are kept at CSU Department of Clinical Sciences. All cell samples including the ones mentioned above, as well as canine PBMCs and endothelial cells were kept and prepared over there. Every cell sample, after it was delivered to our lab, remained refrigerated until it was used for cell experiments. Each

cell experiments would last a few hours during which the cells stayed at room temperature. It was widely believed that cells would only stay viable for a few hours after they were extracted from culture media and re-suspended in PBS. However, valid OFIS spectra were acquired from cells that were 30hrs old and have been stayed at room temperature for at least 1 hr. Test the time dependency of cancerous cells' viability will answer the question of whether acquiring OFIS spectra from the same batch of cells over 24-hour time scale is a valid presentation of cell line.

Another concern arose after DEP electrodes were implemented on OFIS chips. It was observed that after being trapped at a relative high voltage (e.g., 14VAC), the cells shrunk, as shown in Fig. 8.4. It was later found out that a consequence of high electric fields required for DEP forces and the salinity needed for the buffer solution is RF Joule heating. Some work has been done to measure the temperature rise caused by AC joule heating with DEP electrodes in a microfluidic channel [1,2]. It was revealed that the viability of the cells depended on the peak temperature rise and time of exposure. Joel Kindt's COMSOL simulation confirmed the local temperature rise of over 60 °C in the middle of DEP traps, with borosilicate substrate and 14V applied voltage.

As a result, an idea of using an alternative substrate with much higher thermal conductivity was proposed. The material chosen was sapphire, which has a thermal conductivity of 35 W/(m·K), over 30 times bigger than that of borosilicate glass. COMSOL simulation predicted approximated 10 °C temperature rise in the middle of DEP traps, with the same experimental conditions as the previous simulation with

borosilicate glass substrates. This temperature rise with sapphire substrates is within the safe range of cell death caused by heat shock [3]. DEP electrodes and a series of experiments were designed to find out whether using different substrate would affect the viability of the cells coming out of DEP traps.

9.2 Experimental method

This section introduces the testing method for cell viability, before describing how the cell sample for the viability test was acquired.

9.2.1 Viability test

As briefly discussed in Section 2.3, the fastest and most commonly used method for cell viability test, is the Trypan blue exclusion test. And this is the cell viability test most easily available for our lab. Trypan blue is a dye exclusion viability test, meaning that it works via a mechanism in which viable cells occlude the dye whereas nonviable ones do not. This mechanism works by exploiting the fact that as a cell loses viability, the cell membrane degrades and becomes more porous. The increased porosity allows the large dye molecules to enter into the cell, whereas it would normally be occluded. Thus the viable cells appear clear whereas those no longer viable are stained blue/purple, while the nonviable one will often appear bloated and transparent. Fig. 9.1 shows a viable and a nonviable cell, stained by Trypan blue.

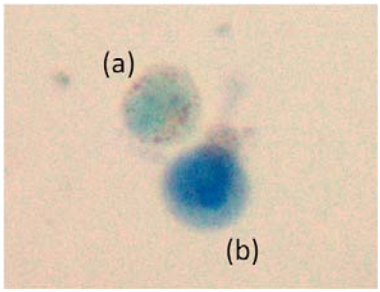

Fig. 9.1 Trypan blue stained (a) viable and (b) nonviable cells under 20X microscope.

Within each cell solution sample, the number of viable and nonviable cells could be counted. And the viability is calculated as

$$Viability = \frac{number\ of\ viable\ cells}{number\ of\ viable\ cells + number\ of\ non-viable\ cells} \times 100\%$$

.

A detailed cell counting and viability test procedure is given in Appendix H. The Trypan blue dye was mixed 1:1 with cell solution. A hemacytometer was used for counting the viable and non-viable cells. The cells in all nine grids inside each counting chamber on the hemacytometer were added up until total number of grid of 30 were counted. Depending on the actual flow velocity and channel dimensions, the cell solution takes 2.5-3.5 hours to collect.

9.2.2 Electrode and experiment design

On the DEP electrode integrated test chips, quadrapole electrodes were designed to apply DEP forces on cells, with the rest of the chip stayed the same as in previously used

OFIS chip configuration. As shown in Fig. 9.2 (a), a funnel structure first focuses the cell flow to the center of the microfluidic channel, and then bar electrodes apply continuous DEP forces. Each section of the bar electrodes is 400 μm in length and the spacing is designed to be 40 μm, the same spacing as the DEP trapping structure reported in [5]. In addition, each set of adjacent bar electrodes is separated by 100 μm so they can be activated separately to provide different DEP to cell interaction time, or more accurately, interaction electrode length. Since the cell flow is still laminar flow in the microfluidic channel, the cells wouldn't escape the traps through these 100 μm separations. Since the actual interaction time between the cells and DEP traps is affected by flow velocity, reporting both parameters reflects the amount of DEP exposure more accurately.

Two chips with identical electrode designs were fabricated, one of which was built on borosilicate glass substrates and the other on sapphire substrates. Since channel depth affects heat dissipation in the channel, the fabrication process is carefully controlled so that the final channel depth was as close as possible. The chip built with borosilicate glass substrates (also called borosilicate chip for short) had a channel depth of 18 μm, while the one built with sapphire substrates (sapphire chip) had a channel depth of 19 μm.

During the experiments, AC signal was applied on the electrodes with the configuration shown in Fig. 9.2 (b). The electrodes were activated as soon as steady flow velocity was realized (usually takes 30 minutes) by setting the ON/OFF duty cycle of the custom syringe pump to 10-15% and were kept on until the end of that experiment.

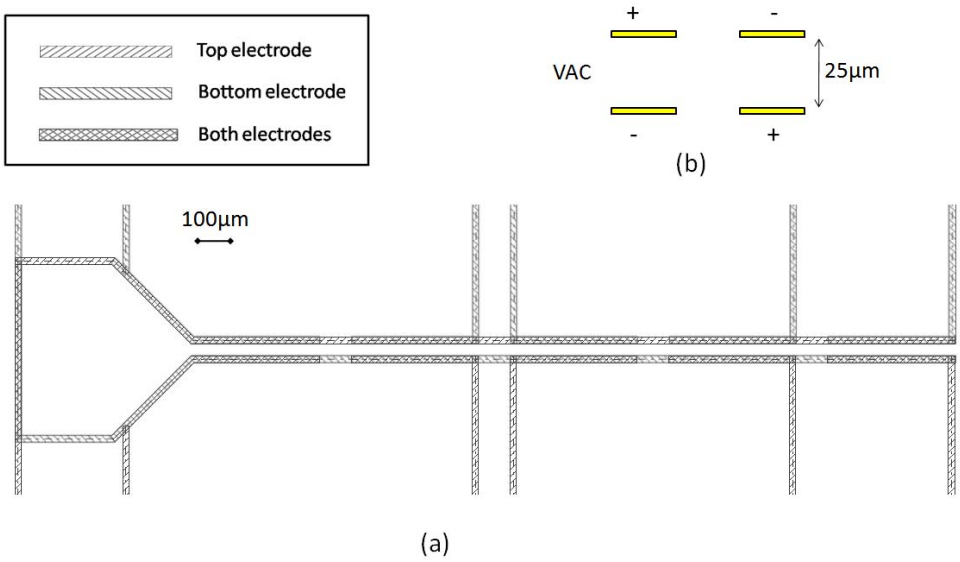

Fig. 9. 1 (a) Top view of trap area on DEP chip; (b) Side view illustration of AC signal applied on top and bottom electrodes.

There were four sets of experiments carried out to investigate the how the cell viability is affected by the exposure dose of DEP, and whether changing the chip substrates to sapphire would reduce joule heating and thus increase the cell viability. In each set of experiments, the viability values tested were: cells going through the DEP electrodes, those going through the microfluidic channel with no DEP electrode activated, and those sitting in a separate vial at room temperature over similar length of time. Experiments were conducted in triplicates for better statistics.

9.2.3 Flow control

During cell experiments, the test chip was clamped in two card edge connectors, same set-up as all DEP trapping experiments. And both inlet and outlet holes of fluidic channel

had nanoport and nanotube connections. Cell flow was regulated by a syringe controlled by the custom syringe pump. Solution coming out of the channel was collected by a small vial with a small access hole on the top for the tubing, so minimal evaporation would occur.

A cell retrieval rate was calculated by comparing the cell concentration of collected cell solution from the channel outlet, and that of the room temperature control by

$$Concentration = \frac{2 \times (number\ of\ viable\ cells + number\ of\ non-viable\ cells)}{number\ of\ grid \times 0.1 \mu L}$$

.

The retrieval rate observed was usually 30-40%, possibly due to the dead zone formed between the nanotube and channel inlet or outlet.

For all experiments, there was a desired flow velocity of 200-250 μm/sec. This velocity was slow enough to make sure 90-95% of the cells could be trapped and that there was at least a few seconds of cell-trap interaction time. Fig. 9.2 shows how cells were being funneled, and then they would stay in the trap area, but only affected by the DEP electrodes that were activated. And it was fast enough so that there was enough volume (at least 15 μL) of cell solution came out the outlet of the chip after a few hours (typically 3-4 hrs). Each hemacytometer sample requires 5μL of cell solution. I started with 3 samples to get a better statistical result.

Fig. 9.2 A snapshot from video showing majority of the cells were being funneled.

The final estimated average flow velocity (around 250 μm) was usually slower than the fastest flow velocity observed (around 350 μm) with microscope. The average flow velocity was estimated after enough volume of cell solution was collected. The total volume was estimated with 10μL pipette, with 5μL setting. Since there were mirrors coated on the chip, the channel depth can be calculated from a cavity spectrum. The velocity was estimated by

$$Average\ velocity = \frac{total\ volume}{(channel\ width \times channel\ depth) \times \exp eriment\ time}$$

.

The time during which flow rate was being stabilized was not counted as experiment time here.

The fluids and cells coming out of the test chip were collected in a cleaned vial. However, at the beginning of the experiments, the vial was detached and the cell collection did not start until 10 minutes after the desired, steady flow velocity was reached. The flow velocity was estimated by the speed of the fastest cell going across the computer screen. The width of the viewing area on the computer screen corresponded to 1000 μm in length, and to get the desired average flow velocity, the fastest cell travelling in the center of the channel would take around 3 seconds to go across this length.

9.3 Viability test results

Firstly time experiments were conducted to evaluate whether it was appropriate to use cells that were 24 hours old (kept in fridge), and whether their viability changed dramatically during a few hours of experiments at room temperature. And then more recently, the effect of DEP exposure dose and chip substrate type on cell viability was assessed with a new electrode design, allowing more accurate and uniform control of DEP exposure dose.

9.3.1 Time experiment

Originally we were told that cells would only survive a few hours after they were taken out of culture media. However, valid OFIS spectra were acquired from cells that were kept in the fridge for at least 30 hours and have been stayed at room temperature during experiments for at least 1 hour. So it was predicted that refrigerated cells would

be viable at higher percentages of the population than the room temperature cells, particularly as time progressed.

This time experiment work was done by a senior design student [6].The results showed that the difference in viability between the cells refrigerated and kept at room temperature is minimal when accounting for the deviation of the data, as shown in Fig. 9.3. It might appear that there was a large amount of error in the data, but here the deviation was calculated with the variation in each hemacytometer grid and it didn't truly reflect the repeatability of the test.

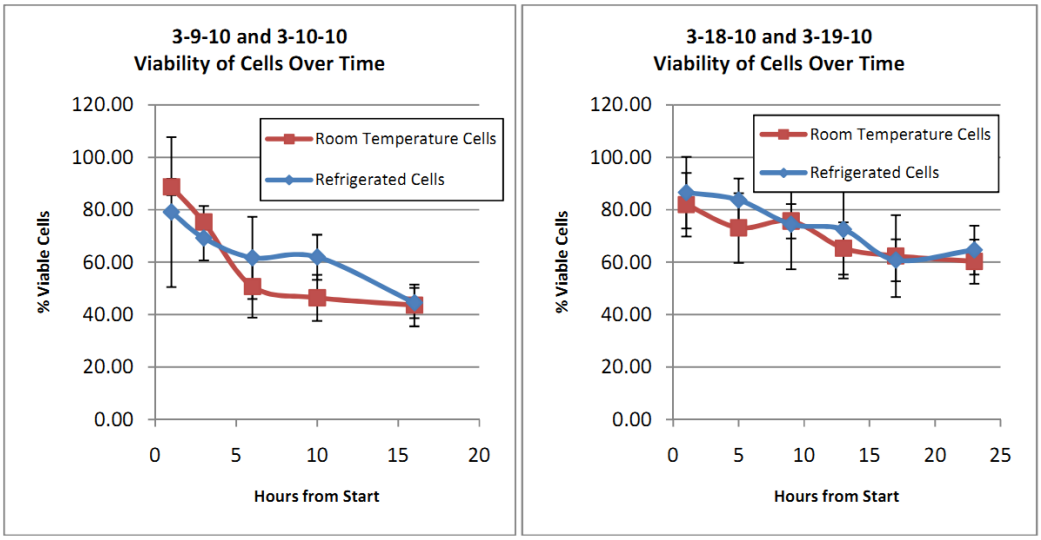

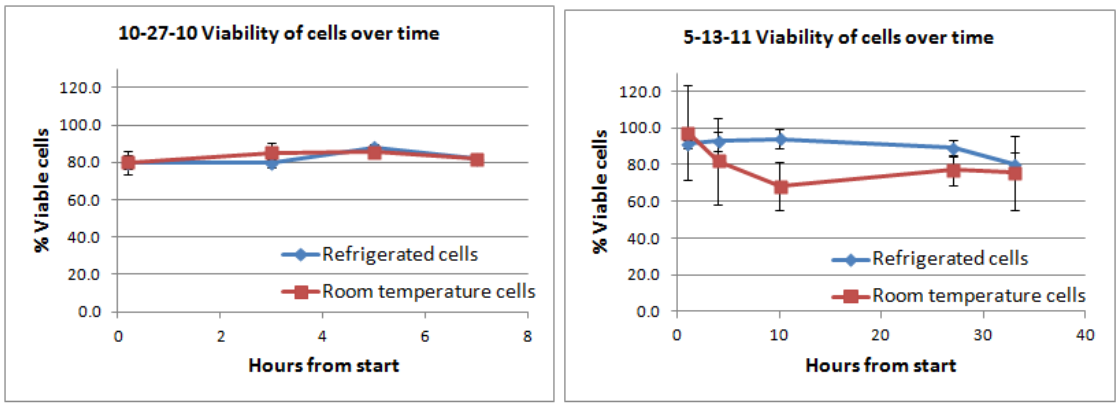

Fig. 9.3: Plots of the percent viability as a function of time for both refrigerated and room temperature cells (with first two plots reproduced from [6]).

This result showed that even after taken out of culture media, a great portion of cells survived after 24 hours. From these four separate tests, one can see that the viability difference in refrigerated cell and cells kept at room temperature was supersizing small. And the cell survival rate had a very large batch-to-batch variation. This variation may

due to the culture conditions such as when the cell line was split, or how many times it was split.

In conclusion, a good portion of cancerous cells stays viable even after 24 hours after taken out of culture media and re-suspended in PBS, both in the fridge and at room temperature. Therefore, using them on the second day or after a few hours of room temperature experiments is acceptable. However, due to the batch-to-batch variation, it is important to take a room temperature control, so that viability result on different day could be directly comparable.

9.3.2 Compare of DEP exposure on two substrates

The viability test results are summarized in Table I below. The first set of experiments, where the activated DEP electrode length was 1200μm, was done for a fourth time, only because a rather interesting viability value from the cells went through the channel, even higher than that of the room temperature control, was recorded. The viability of cells does have batch variation due to their life cycle, the culturing and splitting conditions, as well as the difference in timing for each experiment. In order to get a more accurate representation of DEP influence on cells between different exposure dose or chip substrate, the ratio between the viability of cells affected by DEP electrodes and those went through the fluidic channel was used for the key parameter for these comparison.

Table I Summary of cell viability test results.

Substrate material	**Experimental condition**	**L=1200µm, VAC=8V**				**L=2000µm, VAC=12V**		
		1	2	3	4	1	2	3
Borosilicate	DEP	68.7	62.4	63.8	72.1	24.0	25.3	27.5
	Microfluidic channel	91.0	77.5	77.3	77.2	82.9	77.6	73.5
	Room temperature control	83.5	90.3	86.2	81.8	91.1	82.7	77.5
	Ratio of DEP/Channel	**0.75**	**0.80**	**0.83**	**0.93**	**0.29**	**0.33**	**0.37**
Sapphire	DEP	77.6	77.1	83.3		79.0	73.6	78.9
	Microfluidic channel	82.7	76.0	86.7		76.5	75.4	83.3
	Room temperature control	88.1	82.1	87.7		85.5	82.8	85.6
	Ratio of DEP/Channel	**0.94**	**1.01**	**0.96**		**1.03**	**0.98**	**0.95**

*L: the activated DEP electrode length.

The same statistical null hypothesis test used before, two sample Student's t-test [7] was applied to evaluate the significance of differences between the cell viability values from two chip substrates and two DEP exposure dose listed above. The resulting p-value of this test depends not only on the separation between the viability mean values, but also on the number of replicas. The outcome of this statistical analysis is listed in Table II.

Table II Calculated *p*-values of two sample Student's t-test.

	Borosilicate substrate L=1200μm, VAC=8V	**Borosilicate substrate L=2000μm, VAC=12V**	**Sapphire substrate L=1200μm, VAC=8V**	**Sapphire substrate L=2000μm, VAC=12V**
Borosilicate substrate L=1200μm, VAC=8V	1	**0.00037**	**0.03241**	0.02653
Borosilicate substrate L=2000μm, VAC=12V		1	0.00031	**0.00034**
Sapphire substrate L=1200μm, VAC=8V			1	**0.70146**
Sapphire substrate L=2000μm, VAC=12V				1

Usually, the significance level where the null hypothesis is rejected is chosen to be 0.05. The four bolded p-values in Table II were calculated from experiment results where only one parameter, either the chips substrate or the DEP exposure dose, was changed. From these values it can be concluded that (a) with borosilicate glass substrates, increasing DEP exposure dose affected the cell viability dramatically; (b) with sapphire substrates, increasing DEP exposure dose didn't significantly affect cell viability; (c) with the same DEP exposure dose, replacing substrate material with sapphire significantly increased cell viability.

Even though our understanding of what happens after cell death and exactly how this process influences cell's OFIS spectra is still being developed, this work confirmed our hypothesis, and COMSOL simulation, that using a high thermal conductive material as

chip substrate reduces the ambient temperature inside DEP traps. And as a result, it increases the cell survival rate. This discovery could be generalized and applied on other applications that utilize DEP structure for cell manipulation.

References:

[1] U. Seger-Sauli, M. Panayiotou, S. Schnydrig, M. Jordan, and P. Renaud, “Temperature measurements in microfluidic systems: Heat dissipation of negative dielectrophoresis barriers,” *Electrophoresis*, vol. 26, no. 11, pp. 2239-2246, Apr. 2005.

[2] M. S. Jaeger, T. Mueller, and T. Schnelle, “Thermometry in dielectrophoresis chips for contact-free cell handling,” *Journal of Physics D: Applied Physics*, vol. 40, no. 1, pp. 95-105, Jan. 2007.

[3] X. M. He and J. C. Bischof, "The kinetics of thermal injury in human renal carcinoma cells," Annals of Biomedical Engineering, vol. 33, pp. 502-510, Apr 2005.

[4] U. Seger, M. Panayiotou, S. Schnydrig, M. Jordan, and P. Renaud, "Temperature measurements in microfluidic systems: Heat dissipation of negative dielectrophoresis barriers," Electrophoresis, vol. 26, pp. 2239-2246, Jun 2005.

[5] J.Kindt, M.Naqbi, T. Kiljan, W. Fuller, W. Wang, D. W. Kisker and K. L. Lear, “Automated optical cell detection, sorting, and temperature measurements,” Imaging, Manipulation, and Analysis of Biomolecules, Cells, and Tissues IX in SPIE Photonics West, vol. 7902, pp. 790222, DOI: 10.1117/12.875608, 2011.

[6] W. Fuller, T. Kiljan, A. Miller, L. Mundhenke and M. Eldeiry, senior design report spring 2010.

[7] J. L. Devore, Probability and Statistics for Engineering and the Sciences, Thomson Brookes/Cole, 6th edition, pp. 360-373.

CHAPTER 10 CONCLUSION

This chapter summarizes contributions of this dissertation to developing optofluidic intracavity spectroscopic biosensing systems for single cancer cell detection. The contributions include achievements related to the fabrication and the testing of optofluidic Fabry-Pérot (FP) cavities, as well as the data analysis and optical modeling of cavity transmission spectra.

10.1 Fabrication

The OFIS chip fabrication is an integral part of the project: the fabrication flow needed to be polished to ensure performance of the chip, and in turn, the experiments motivated the modification and optimization in the fabrication.

The major improvements in the fabrication include:

i. PDMS permanent bonding to non-mirror coated glass;

ii. Experimented with In soldering for chip bonding, proved that it was not a permanent and complete seal;

iii. Optimized the UV epoxy bonding according to the OFIS chip structure, and applied it as the only bonding method that potentially has a 100% yield (bonding is reversible until satisfactory results are achieved) and complete sealing over time;

iv. OFIS chips bonded with UV epoxy had an optical finesse of the cavity of at least 13 when the SU-8 fabrication was carefully controlled;

v. With the help of senior design students, designed and fabricated planar trapping, funneling and steering DEP electrodes, as well as the contact pads whose dimension fit the card edge connector ;

vi. Fabricated microfluidic channel of various channel depth with SU-8 3025 and SU-8 2035, making fabricating chips with 3-D traps possible;

vii. With the help of senior design students, designed and fabricated quadrapole 3-D traps for FTS and ACSU chips;

viii. Designed and fabricated SU-8 microfluidic channel with side channels for cell sorting chip;

ix. With the help of senior design students, optimized the fabrication flow for SU-8 channel patterning with chip lifting device for an optical finesse of the cavity of at least 10;

x. Optimized the Nanoport attachment method with Crystalbond.

10.2 Experiments

The major accomplishments in the OFIS experiments include:

i. With traditional Voldman DEP trap in a PDMS channel, demonstrated trapping of 7μm and 15μm (in diameter) polystyrene spheres at 40 μm/sec flowrate;

ii. With the help of senior design students, implemented custom syringe pump with LabVIEW controls to set the pump speed and the On/Off time;

iii. Designed a procedure for setting up experiments, which would exclude air bubbles from the fluidic system;

iv. With manual control of the custom syringe pump, stabilized the fluidic flow and collect OFIS spectra of 32 settled HSA cells and 32 PBMC cells in 2 OFIS chips;

v. With manual control of the custom syringe pump, stabilized the fluidic flow and collect OFIS spectra of settled human ovarian cancer cells from 5 cell lines, both cancerous and non-cancerous;

vi. With the help of senior design students, implemented the card edge connectors to make electrical connections with the DEP electrodes on OFIS chips;

vii. With the first generation quadrapole traps, demonstrated trapping of 7μm and 15μm (in diameter) polystyrene spheres, as well as various cells (such as lymphoma, HSA and OSA cells) at over 100 μm/sec flowrate;

viii. Trapped and collect transmission spectra of OSA cells from 2 cell lines with different metastatic potentials;

ix. With the help of senior design students, set up apparatus for automated detection of cell presence, switch of the RF signal to DEP electrodes, release of the trapped cell, as well as real-time analysis of the transmission parameters of the cell;

x. With the help of senior design students, trapped and analyzed 200 cells continuously with the automated system;

xi. Differentiated settled human ovarian cancer cells and PBMCs based on the characteristic transverse mode pattern in their OFIS spectra, although the differentiation between ovarian cancer cells and non-cancerous ovarian cells was not successful;

xii. Similarly, by analyzing the OFIS spectra on settled cells, the differentiation between canine HSA cells and non-cancerous endothelial cells was not successful;

xiii. Compared the OFIS spectra of OSA cells when increasing AC voltage was applied to cells from 2 cell lines with different metastatic potentials and summarized the number of transverse mode peaks and the voltage that make additional peaks appear, however, it was not concluded that DEP can deform the OSA cells without causing denaturation, or other kinds of cell death that may affect the OFIS spectrum;

xiv. Designed DEP electrodes to apply adjustable, uniform DEP forces on majority of cells passing through microfluidic channel without immobilizing them, and used this design to systematically investigate the effect of chip substrate and DEP exposure dose on the survival rate of cells coming out of OFIS system.

10.3 Statistical analysis

i. Analyzed frequency dependence of the DEP force needed to immobilize 15μm polystyrene spheres at 40 μm/sec flowrate;

ii. Qualitatively compared the OFIS spectra of settled canine HSA cells and PBMCs, and differentiated them by their distinctive transverse mode pattern;

iii. Normalized raw OFIS transmission spectra based on the illumination LED envelop and the transmission of other optical components, so that the ones collected from different location of the channel or different days could be directly compared;

iv. Generalized the transverse mode pattern into 2 transmission parameters, average transmission and standard deviation, to quantitatively compare the OFIS spectra of settled canine HSA cells and PBMCs;

v. Applied statistics methods such as two sample Student's T-test on cells' transmission parameters to analyze the cell differentiation results of canine HSA cells and PBMCs;

vi. Produced ROC curve that demonstrate the sensitivity and specificity of the binary cell classification result of canine HSA cells and PBMCs.

10.4 Optical modeling

i. Constructed an optical model that treat a cell settled at the channel bottom as a thin lens and applied it to reproduce the experimental transmission spectrum of an apertured optical resonator;

ii. Used the cell lens model to extract focal length value from OFIS spectrum of each individual cell, and differentiated among canine HSA cells, lymphoma cells and PBMCs based on their focal lengths;

iii. Constructed an optical model that treat a cell in the cavity as a thick lens, which is a more accurate model compared with thin lens model;

iv. Investigated how different factors such as cell position, cell thickness and the radii of curvature of its top and bottom surfaces affect the transverse mode spacing in a cell spectrum.

APPENDIX A OPTICAL ADJUSTMENTS

This appendix summarizes the step to bring the optical system into alignment. A good optical alignment not only provides visual confirmation of the cell movement and trap status in the microfluidic channel, but also facilitates the spectral measurement of certain object (cavity location or cells).

1. Use the blue LED as bottom illumination (or other light sources with visible light beam). Note that the forward current of the blue LED (20mA) is much smaller than that of the high-power infrared LED (80 or 100mA).
2. Roughly align the microscope and light source by moving the translation stage attached to the optical plate where the chip sits, while leaving room for further adjustment.
3. Turn on the top illumination light on the microscope; make sure the microscope illumination light falls on the opening of optical plate and on the bottom illumination LED.
4. Add a lens to the optical path (between the LED and the optical plate).
5. Put a piece of paper on the optical plate, adjust the height of the LED, until the size of the blue spot is minimal.
6. Switch to infrared LED light source (make sure it's on/close the original location of the blue LED); turn off microscope light; turn on the CCD camera and the camera software.

7. Put a sample (with electrodes or other features, and with a reflective surface such as mirror or large area of gold) on the optical plate; adjust the height of the microscope until features are imaged on the camera.
8. Use the reflective surface part of the sample, shoot light (either blue or infrared) back through the fiber; this could be done by taking the fiber off the spectrometer side and align it with the bottom illumination LED, or by using a 3dB coupler and a separate LED or laser diode.
9. If the alignment is good, you should be able to see a bright spot on the computer screen. If not, it might be due to the misalignment between the CCD array and illuminated area; or the mismatch in optical length between the microscope and the fiber.
10. To fix the misalignment between the CCD array and illuminated area, take the camera off from the top of the microscope and move it around slightly (with very small displacement at a time), both in the horizontal direction and vertical direction, until the bright spot shows up on the screen. And then adjust the camera position so that the bright spot can be visualized on the camera.

    (If the spot is off the center too much, one can also take apart the top portion of the microscope and adjust the splitter inside.)
11. To fix the mismatch in optical lengths, locate the threaded tube (with: two side screws for lateral adjustments; black tube for rough “vertical” adjustment; silver tube for fine “vertical” adjustment) on the left hand side of the microscope; gently push the optical plate up and down a little to find out: in order to make

the spot size smaller, the fiber tip need to move closer to the object, or further away from it.

12. Turn the tubes in or out to make vertical adjustment:
    a. make sure the fiber is not twisted too much; whenever necessary, take the fiber off, release the tension and put it back on;
    b. make sure that there's no relative movements among all the adjustable elements when the tubes are turned in or out;
    c. if the threads are exhausted, take the tubes off and move the fiber connector to a better position.

    The minimum spot size is 10-15 μm with the 5x lens (this could also be estimated by comparing the spot size with on-chip electrodes of known size, or with micro-spheres).

13. When optical adjustment is done, the exact spot location might drift; so it would be a good idea to check the spot size and location from time to time, or before critical spectral measurements. After adding the 3dB fiber coupler, this could be as easy as turning on the laser diode driver and adjust the acquisition time on the camera software.

APPENDIX B STEP-BY-STEP EXPERIMENTAL SETUP

This appendix describes the process to set-up a cell experiments, which was established over the years and part of it has been documented in senior design reports [1-2].

1. Choose an OFIS chip and make records

Choose the type of chip you would like to use based on the purpose of the experiments.

Each chip has a unique chip # that is marked on the case and it contains the following information:

- The date when the chip was made (i.e. 090324 which corresponds to 03/24/09).
- A single digit # when more than 1 chip were made in the same day.
- The type of the electrode design (i.e. FTS which means funnel, trap and steer).
- The type of substrate used (i.e. a letter d indicates that the chip has mirror coating).

In the lab notebook, put down the purpose of the experiments, the chip#, sample used and electric connection configuration (especially when not all the electrodes were used).

2. Prep the chip (Wear gloves)

A. *Use isopropanol to start the experiment bubble-free.*

- Take the isopropanol syringe and pull off the plastic tip so the needle is showing. Make sure there is a drop of isopropanol on the tip of the needle by slightly pushing on the syringe.

- Place the needle into the nanoport attached to the chip inlet. Look at the bottom of the chip, look into the inlet hole to make sure that the needle is touching the glass.

- Begin filling this port with isopropanol until a little over half full. Turn chip over to check for any bubbles in the inlet. If there are any bubbles they need to be removed. The bubble can be sucked up with the same syringe of isopropanol or using the air pressure the bubble can be blown out.

- Once the bubble is gone, add more isopropanol so it reaches the top of the nanoport.

B. *Attach the nanoport adaptor and nanotube.*

- The syringe containing either DI or PBS (phosphate buffered saline) can be used to attach to the nanotube. The PBS is usually used as a prep for cells. On the syringe unscrew the plastic portion that contains the needle.

- Take the nanotube (long red tube) and screw this into the syringe. This can be placed to the side for now.

- The nanoport is a small funnel looking device that screws into the inlet port attached to the chip. These are usually kept in a clear plastic box found next to the computer. Place this into the inlet and begin screwing it into place. Before it is too tight the end of the nanotube can be place into the nanoport. The nanotube should almost touch the glass in the inlet. Once this is in place, the nanoport should be screwed in tightly so leaking does not occur. Make sure there are no bubbles in the inlet reservoir. If there are bubbles, return to step A.

C. *Clean the channel.*

- Using either the DI or PBS solution attached to the chip, begin pushing on the syringe lightly. The solution should begin to come through the outlet.

- The chip can be turned over so that the outlet is lying against the napkin on the desk to collect the solution. Run the solution through the channel for a couple minutes to remove residual isopropanol.

D. *Deliver the cell solution or spheres.*

- Unscrew the syringe with DI or PBS. Make sure the adaptor that connects to the syringe is still filled with solution by adding more from the syringe (this keeps bubbles out of the line).

- Reverse the syringe to induce some air (air volume: cell solution volume = 1:5 or 1:10), this will make flow control easier; and if custom syringe pump with a duty cycle is used, this will ensure steady flow.

- After unscrewing the needle of the syringe containing cells, gently push on the syringe so that you can see a bead of solution.

- Screw this syringe into the adaptor. This syringe can be placed in the syringe holder that is used to pump the solution.

E. *Place chip on the stage under microscope.*

- Make sure chip is secured under the metal latch or clips (if card edge connectors are used).

- Using the black knobs attached to the base holding the chip, you can adjust what the microscope is focused on by moving the stage left or right, or up and down to focus in on the channel.

3. View the channel on the computer

- Turn on the Hewlett Packard power supply switch (the top box on the left corner of the desk) to turn on the illumination LED.

- Meter selection should be on mA and the reading should be around 80mA.

- This can be changed using the dials. This can also be adjusted for lighting purposes when viewing the channel.

- On the lab computer, click start, all programs, Basler vision technologies and Pylon Viewer.exe.

- Click to choose the camera “Basler scA640-74gm”, and then choose continuous shot. If microscope lights are turned on you will be able to see what is under the microscope. If the picture is black see step 4 to turn on equipment.

- You can adjust the lighting with acquisition controls under the feature of the camera, both exposure timebase and exposure time (raw) can be changed.

- After finding the channel, gently push or pull the syringe until cells are found in the channel; push or pull the syringe to achieve a proper flow (not too fast to clog the channel and not too slow so that some cells can be spotted). Leave the syringe upright on the syringe holder.

- In the camera program, click save image to take a picture.

- To confirm the light collecting spot, turn on the Melles Griot laser diode driver and enable the 2nd infrared LED located on a separate prototype board. Increase the exposure time on the camera software and find the small bright round spot on the screen.

- If the spot cannot be found, adjust the stage up and down, or the fiber position (by turning the tube or the 2 screws), or even the position of the camera.

4. Control the flowrate

- Use manual control of the syringe to get the flow rate to an acceptable range.

- Turn on the Oriel Encoder Mike Controller (custom syringe pump) on the desk in front of the computer; the switch is on the back.

- Make sure the vel and m1 motor tabs are lit up with red lights.

- Set the speed of the pump from 0.5-200. Once you push in value you would like, press the enter button which looks like an arrow at the bottom right corner of the number pad.

- Put the syringe on the syringe holder and adjust the controller position so that it is barely pressed against the syringe. To make the pump go up press the run

button on the bottom right hand corner of the machine, and to make the pump go down press the run button on the left hand corner machine.

- Turn on the remote mode (by switching on the “rem/loc”) on the controller so that the LabView program can be applied to pump the syringe with certain duty cycle.

- In the LabView program “Evan’s control”, toggle the two right toggles (stop and manual cmd) in the down position or off position.

- Then set the pump ON/OFF time based on the duty cycle the user wants (usually 10%-50%, based on experimental observations of the stabilized flowrate). The delay before write and delay before read are usually left at 500 ms.

- To check that the pump is working the bottom left run button will turn red for X second and turn off for Y seconds if the Labview is programmed to turn on the pump for X seconds then off for Y seconds.

- To deactivate the pump just push “rem/loc” again; to change the pump speed on the controller, it needs to be out of the remote mode, too.

- If the flowrate needs to be changed immediately, manual control of the syringe is the fastest way to adjust it; otherwise the custom syringe pump can provide steady flow **over a few hours**, although partial clogging of the microfluidic

channel might occur and **a higher flow speed or even a thorough rinse of the channel is required to avoid permanent damage to the fluidic system on the chip.**

5. Trap cells or sphere

- Make electrical connections from the function generator to electrodes on the chip.

- Turn on the function generator, check the waveform, offset, frequency and voltage setting. One critical parameter is that the frequency range should be kept above 300 kHz.

- The voltage setting can be adjusted with the left two buttons under auto vernier and the maximum voltage is 16V.

- If the “disable” button on the bottom right of the front panel is red, that means the AC signal is disabled. Just press the button to enable the trap if manual trapping is used.

- If automated trapping is applied, press the “disable” button so that the AC signal is controlled by the relay.

- The LabView program that controls the relay is now collecting spectrum intensity data from the spectrometer.

- In the LabView program “DAQContV1.47-t”, the spectrum was monitored with a 100ms live integration time.

- The user can set a trapping threshold for the changes in the maximum intensity of the monitored spectrum.

- As long as cells are moving slow enough (<200μm/s) through the light collecting spot, its presence can be detected and this triggers the trap.

6. Take spectral data

- If manual data collection is used, open the OOIBase32 program, set the “Integ. Time” and right click in the spectrum window then “store dark”.

- Right click again and change the view mode to “scope mode minus dark”.

- The processed spectrum can be saved at any time. You can store the dark again if fluorescent peaks show up or when the integration time is changed.

- The same LabView program (“DAQContV1.47-t”) also has the ability to collect transmission spectrum of the trapped cell automatically.

- User can set an integration period for the saved spectrum of the trapped cell. The time is usually selected to be 3-6 seconds for better signal to noise ratio.

- As soon as the cells are trapped, the data acquisition will start and after the integration is done the saved spectrum will be displayed.

- The automatic release of the cell can be turned off, in case the cell is not well centered with the light collecting spot and more data need to be recorded. Otherwise the program will turn off the trap and release the cell after the user defined “time until release” is elapsed.

- Currently the transmission parameter method is integrated to the program to analyze the transverse mode strength of the spectral data; the result is plotted in the “deviation and mean” window. Other real-time analysis can be applied with future changes in the LabView program.

References

[1] J. Kindt, L. Netherton and H, Cutler, senior design report, spring 2009.

[2] W. Fuller, T. Kiljan, A. Miller, L. Mundhenke and M. Eldeiry, senior design report spring 2010.

APPENDIX C TRANSMISSION PARAMETER CALCULATION

- LORENTZIAN FIT

Detailed instructions and calculation algorithm are summarized in file “Appendix D P-value calculation.xls”

APPENDIX D P-VALUE CALCULATION

Detailed instructions and calculation algorithm are summarized in file “Appendix D P-value calculation.xls”

APPENDIX E ROC CURVE

Detailed algorithms on ROC curve construction and AUC calculation are summarized in file “Appendix E ROC curve.xls”

APPENDIX F LOSS FOR APERTURED LAGUERRE GAUSSIAN

Detailed analysis and calculation steps are summarized in MathCAD file “Appendix F Loss for apertured Laguerre Gaussian.xmcd”.

APPENDIX G THICK LENS WITH GUOY PHASE SHIFT

Detailed analysis and calculation steps are summarized in file “Appendix G Thick lens with Guoy phase shift.xmcd”.

APPENDIX H CELL COUNTING AND VIABILITY TEST PROCEDURE

1. Use a 10μL pipette (with a clean tip) to put certain volume of cell solution in a cleaned vial.

2. Change the pipette tip and put same volume of Trypan blue solution in the same vial; be careful not to let the pipette tip touch the cell solution.

3. Mix thoroughly by taking the solution and pumping it out (with the same tip).

4. Allow mixture to stand for 5min at 15-30 °C (room temperature).

5. To prepare the hemacytometer, clean the mirror-like polished surface carefully with a Kimwipe (or clean room wipe) and alcohol (such as methanol). The coverslip, which is thicker than those for conventional microscopy, should also be cleaned. Place the coverslip over the counting surface prior to adding the cell suspension.

6. Pipette 10μL of the cell/dye mixture (one sample for each duplicate well) under the cover glass on a hemacytometer at the sample introduction point. The area will fill be capillary action. Enough liquid should be introduced so that the mirrored surface is just covered.

7. Put the hemacytometer under the microscope in C7, use 10x lens to find the chamber and then switch to 40x lens for the counting.

8. Count all the live cells (round to oval and colorless/birefringent) and dead cells (stained by the dye, deep blue color). One can start with the center 1mm x 1mm square; then move on to the 4 squares forming the cross shape, or count all 9 squares if necessary (e.g., not enough cells are found in the center square). Cells dyed blue are dead.

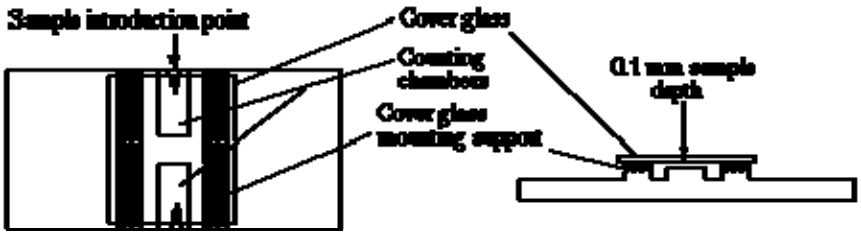

Fig. 1 Top and side view of a hemacytometer.

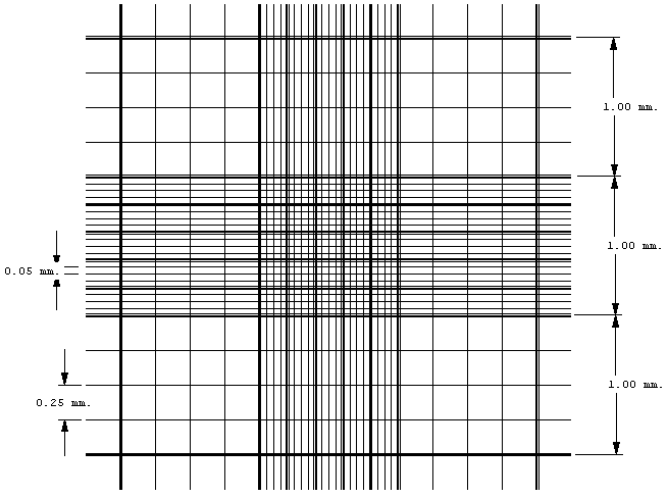

Fig. 2 Configuration of one of the two counting chambers.

9. Use the following equation to calculate the concentration (number of cells/ml) of the cell solution:

   Total # of cells counted divided by number of squares counted (usually 1, 4 or 9). Multiply X 2 (dilution factor) X 1 x 104 (one square has a volume of 1 x 10-4 ml) – OR total # of cells counted divided by number of squares counted times 100000. Cell counts between duplicate dilutions should agree within +/- 20%.

10. Use the following equation to calculate the viability (percentage of viable cells) of the cell solution:

    Viability = # of viable cells / (# of viable cells + # of non-viable cells) x100%.

11. Clean the hemacytometer and cover glass with wipe and alcohol. Rinse the pipette tips with alcohol and DI water.

Application notes and other precautions:

1. Be extremely careful with higher power objectives, since the counting chamber is much thicker than a conventional slide. The chamber or an objective lens may be damaged if the user is not careful. One entire grid on standard hemacytometers can be seen at 40x (4x objective).

2. Suspensions should be dilute enough so that the cells or other particles do not overlap each other on the grid, and should be uniformly distributed.

3. To perform the count, determine the magnification needed to recognize the desired cell type. Having the scope slightly off focus makes the viable cells more visible.

4. For cells that overlap a ruling, count a cell as "in" if it overlaps the top or right ruling, and "out" if it overlaps the bottom or left ruling. One can use a different algorithm to prevent double counting the cells overlapping a ruling, but be consistent!

Reference:

[1] R. Freshney, Culture of Animal Cells: A Manual of Basic technique, pp. 117, Alan R. Liss, Inc., New York, 1987.